Computational Modeling of a Biomass Micro-gasifier Cookstove

ANOOP ASRANNA I.P.

Master of Science Thesis

P&E Report Number: 2697

TU Delft Delft University of Technology

Computational Modeling of a Biomass Micro-gasifier Cookstove

MASTER OF SCIENCE THESIS

For the degree of Master of Science in Mechanical Engineering

Track - Sustainable Process and Energy Technology at Delft University of Technology

Anoop Asranna I.P

September 30, 2015

Faculty of Mechanical, Maritime and Materials Engineering (3mE) · Delft University of Technology

DELFT UNIVERSITY OF TECHNOLOGY

DEPARTMENT OF PROCESS AND ENERGY TECHNOLOGY

The undersigned hereby certify that they have read and recommend to the Faculty of Mechanical, Maritime and Materials Engineering (3mE) for acceptance of a thesis entitled

COMPUTATIONAL MODELING OF BIOMASS MICRO-GASIFIER COOKSTOVE

by

ANOOP ASRANNA I.P

in partial fulfilment of the requirements for the Degree of

MASTER OF SCIENCE MECHANICAL ENGINEERING

Dated: September 30, 2015

Supervisor(s):

_____

Prof. Dr. Bendiks Boersma

_____

Dr. Paul van der Sluis

Reader(s):

_____

Dr.Ir. M.J.B.M. Pourquie

_____

Dr.Ir. W.de.Jong

The work in this thesis was supported by the Philips Microsystems and Devices group. Their support is gratefully acknowledged.

ABSTRACT

The World Health Organization (WHO) states that indoor air pollution resulting from inefficient burning of biomass in traditional cookstoves is a major health hazard affecting around 2.7 billion people globally. With the use of biomass for cooking energy expected to grow in the coming decades, efficient energy conversion technologies are an urgent need.

The Philips woodstove based on the principle of micro-gasification of biomass is one such technology having the lowest reported emissions among wood burning cookstoves. The stove is based on experimental design and gaps exist in understanding the physics involved. Integration of simulations into the design process is expected fill these gaps and enable the characterization of key design parameters. A computational fluid dynamics based simulation model is developed for this purpose to investigate the fluid flows and heat transfer in the secondary combustion zone of the micro-gasifier stove.

A three dimensional model of the stove is built using COMSOL Multiphysics. Combustion is modelled as a volumetric heat source with uniform heat generation. With appropriate boundary conditions a close approximation of the stove operating conditions is obtained and convergence achieved.

The results demonstrate that the model is partially successful in simulating the flaming mode operation of the stove. The flow pattern is in agreement with visual observations. The temperature field inside the combustion chamber suffers because of the uniform heat generation assumption. The highest temperatures occur around regions of flow stagnation which is not representative of the actual operating conditions. The temperature values outside the combustion chamber are more reasonable, however still inaccurate. Including all the design details is expected to return more agreeable results.

It has been realized that the discrepancy in the temperature field is because the secondary air flow rate specified in the model is only 43% of the experimental value. By specifying a secondary air flow rate closer to the experimental value, a closer approximation of the operating conditions is expected.

A mixing analysis is carried out for two different heights of the fuel bed using passive scalars. The recirculation zone is found to have a significant impact on the mixing of the two streams. The simulations predict that at higher fuel bed heights the recirculation zone is restricted in space leading to poor mixing of the air and fuel stream.

A validation study of the mesh used is conducted to ascertain its accuracy. A high Reynolds number jet is simulated and the results are compared with experimental values. The centerline velocity decay obtained using the mesh in regions close to nozzle exit is within 10% of the experimental values. The lateral velocity predictions are 20% lower than the experimental values. Since the distances in the computational domain do not extend beyond x=15D, the mesh used is expected to return accurate results.

In its current state, the model is a good tool for flow visualization and understanding the broad qualitative trends. For comprehensively characterizing the design parameters of the stove, a better definition of the heat source term and reactive flow modelling is necessary.

TABLE OF CONTENTS

Table of figures

List of tables

Acknowledgements

I would like to express my sincere gratitude to Dr. Paul van der Sluis for have given me the opportunity to work on the woodstove. It is an inspiration watching him work in the lab and come up with ideas that always seem to work. I have thoroughly relished interacting with him. I have enjoyed working on this project through the course of its ups and downs which has largely been possible because of Paul's co-operation.

My intention of taking up this Master's program was to work on sustainable technological solutions that would create a social impact. I am glad I could pursue my passion in the form of my thesis.

I would also like to thank Dr Sergei Shulepov from Philips Research for his valuable inputs all through my thesis. Discussions with him have helped me develop a better understanding of simulation models. Also I would like to express my special gratitude towards Dr Peter Bouma, who patiently went through the report and helped me shape the report to its current form. His analysis has helped me interpret and present the results of my simulations better.

I express my gratitude to Dr Bendiks Boersma who agreed to take up the responsibility of guiding me midway and made sure I got through to the end. It is a privilege to have worked under your guidance and I thank you for your patience and support. I also thank Dr Aravind for the initial support and guidance.

This thesis would not have been possible without the constant support of my parents and family. A big thank you to all my friends here in Netherlands who have made life enjoyable here.

I write these lines with a sense of gratitude and accomplishment. The past two years in TU Delft has been fulfilling on all grounds and has lived up to what it promised to be. I thank everyone who has made this possible.

1. Introduction

In this section, a brief introduction to the use of biomass as a cooking fuel and its consequences is provided. This is followed by the motivation for the current research. A short literature study follows which leads us to the problem definition. The scope of the assignment is laid out in the problem definition.

1.1. BIOMASS AS A COOKING FUEL

Biomass constitutes a significant share of the energy mix in rural households across the world. Globally, about 2.7 billion people depend on direct burning of biomass such as wood, cow dung and agricultural waste to meet their cooking energy need accounting for almost 90% of the total household energy consumption. (IEA, 2015)

While biomass in itself is a sustainable form of energy and carbon neutral, unsustainable land use practices and inefficient energy conversion technologies have far reaching consequences on global climate and human health. (Bhattacharya and Leon, 2005)
Emissions from biomass can be due to two factors:

1. Emissions resulting from unsustainable harvesting of the fuel
2. Emissions from combustion/incomplete combustion of the fuel

Use of wood, the predominant cooking fuel, seriously impacts the ecology and land usage patterns (Arnold et al, 2003).It is the leading cause of deforestation in developing countries (Rudel, 2013). Sustainable harvesting will need to ensure that the carbon dioxide released during combustion is reabsorbed by the biomass grown to replace it (MacCarty et al, 2007).

Figure 1.1 shows the traditional 3 stone fire which is used extensively for domestic cooking and heating applications. Also shown is a type of clean cookstove which will be discussed later on in this section.

Figure 1.1: Left) A traditional 3 stone fire Right) A 'clean' cookstove (Image source: UN Foundation)

Along with CO_2, incomplete combustion of biomass/wood in traditional fires such as the one shown in figure 1.1 release large amounts of CO, CH_4, black carbon and volatile organic components into the atmosphere. All of these are potent greenhouse gases with their greenhouse warming potential several times that of carbon dioxide. The amount of pollutants released for combustion of wood in the traditional three stone fire and their global warming potential is provided in table 1.1.

Product	**Amount released(g) /kg of wood** (Bailis et al,2014)	**Global warming potential, 100 years CO_2equivalent** (MacCarty et al,2007)
CO_2	1584	1
CO	57.4	3
CH_4	2	21
Black carbon	0.9	680
OC	1.4.	50
Other hydrocarbons	7.8	12

Table 1.1: Combustion products and their global warming potential

Using this data it is calculated that the traditional three stone fire releases about 500g of equivalent of CO_2 per liter of water boiled for 30 minutes (MacCarty et al, 2007). Emissions from such open fires accounts for about 2% of the total global emissions (Bailis et al, 2014)

The black carbon released as an aerosol is the second most significant contributor to global warming after carbon dioxide (Ramanathan and Carmichael, 2008). Black carbon resulting from biomass burning is the leading cause for glacial melting in the Himalayan region (Menon et al, 2010). Cookstove smoke contributes 21% to the overall black carbon emissions. (Global Alliance for Clean Cookstoves, 2015)

Apart from the serious climate consequences, direct burning of biomass also has a detrimental effect on human health. The soot, carbon monoxide and the hydrocarbons released from combustion in ill ventilated spaces cause respiratory infections, pneumonia, chronic obstructive and pulmonary diseases

resulting in 4.3 million premature deaths worldwide annually. (Bruce et al, 2006) (WHO, 2012)
A comparison with some other major factors of premature deaths is given in figure 1.2. The data for deaths due to smoke from biomass is from 2012 while the rest the data is for the year 2013.

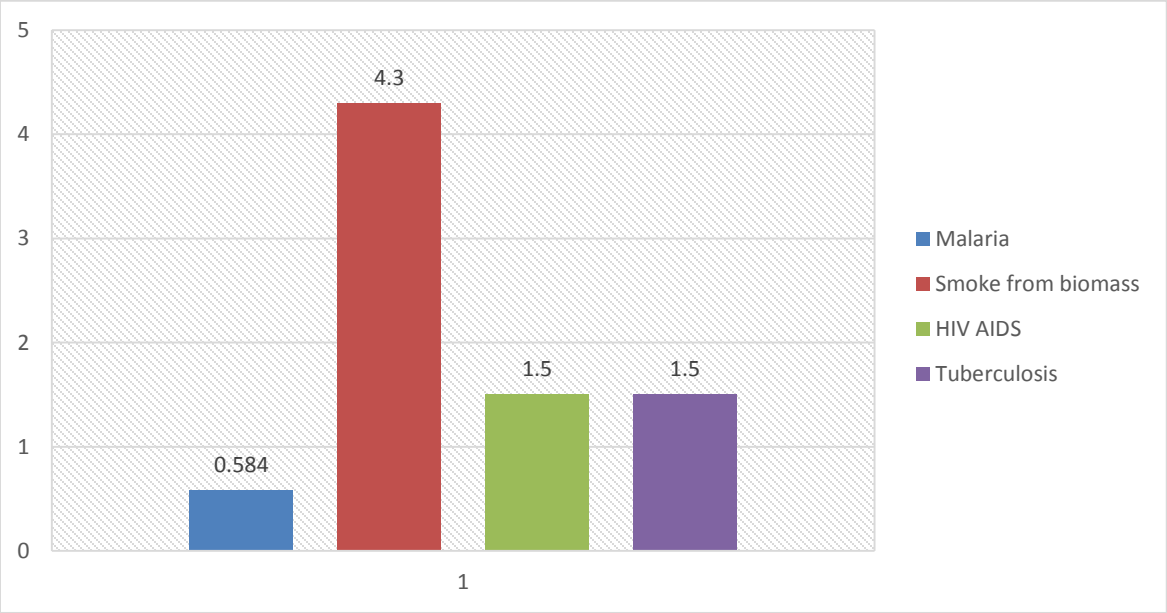

Figure 1.2: Annual deaths worldwide and cause (WHO, 2012) (WHO, 2013)

Figure 1.2 reveals the real extent of the hazard posed by the inefficient burning of biomass. It accounts for more deaths than Tuberculosis, HIV AIDS and Malaria combined.

In view of these serious threats posed by traditional cookstoves, several alternatives have been proposed. The prominent ones being:

- Switching to modern cooking fuels and technologies
- Promoting efficient and sustainable biomass energy conversion technologies and setting up sustainable supply chains

The switch to modern cooking fuels such as liquid petroleum gas and electricity is a feasible long term solution. Complete elimination of indoor air pollution will need a transition to these modern fuels (Goldemberg et al, 2004). However this transition is expected to take a few more decades given the size and distribution of rural communities worldwide. Consequently, the number of people relying on biomass for their cooking needs is expected to increase to over the coming decades (IEA, 2006).

The IEA (International Energy Agency) in its 2006 outlook had estimated a total of 2.7 billion people to be reliant on biomass for cooking energy by 2030. The latest numbers for 2015 indicate that this number has already been reached (IEA, 2015). Therefore efficient biomass conversion technologies are an urgent need.

Clean cookstove technologies were developed in response to this need. They are more fuel efficient and have lower emissions compared to the traditional cooking stoves. The Global Alliance for Clean Cook

stoves is a global stove program that aims to disseminate 100 million improved stoves worldwide by 2020. This can bring down the overall emissions caused by wood by around 11-17% (Bailis et al, 2014).

The Philips woodstove is one such clean cookstove working on the principle of micro-gasification. In a micro- gasifier the combustible gases in the biomass are driven off from the solid fuel to a combustion zone where they are burnt separately. This enables better control over the process of combustion in comparison to direct burning. (Roth, 2011).

The current work attempts to develop a computational model of the woodstove to comprehend the physics involved in the stove operation better. A brief motivation for the current research is provided in the following section.

1.2. MOTIVATION

The Philips woodstove is one of the best performing stoves both in terms of efficiency and emissions available in the market today (Jetter et al, 2012). The stove has been developed based mostly on experimental design. While this approach has yielded a high performing stove, the following limitations exist:

- The underlying physics involved in the wood stove operation is not completely understood. This knowledge gap has led to an inadequate characterization of the design parameters of the stove.
- It is not possible to obtain all data experimentally. Key parameters like the flow rates are difficult to measure at all locations or will need sophisticated measurement techniques.
- Traditional workflows based on building physical prototypes involves a lot of manual effort and are also expensive. They are not always feasible, especially during the design optimization phase.

The integration of simulation in the design phase is expected to overcome these limitations. A simulation based design will mean avoiding the costly physical prototypes and enables optimization at the early stages of the design lifecycle.

In view of these benefits, it is decided to develop a simulation model for the Philips woodstove. The simulation model is expected to aid and inform experimental design and not replace it.

To decide on the modelling approach a literature survey of the past stove modelling efforts was done. Some important approaches are discussed below.

1.3. LITERATURE STUDY

Past stove modelling efforts have relied both on analytical and computational methods to model the determine flow properties and behavior. A short summary of both these efforts is provided in the following section.

1.3.1. ANALYTICAL MODELS

Early analytical models focused on specific aspects of the cookstove like combustion chamber size, nozzle spacing etc. The first detailed model is reported in Bussman, 1982 who modelled the gas phase combustion region above the fuel bed. The rising plume of volatiles from the fuel bed was also modelled. Properties such as the gas velocity and temperature were expressed as a function of the height of the

plume. All the gases i.e. the air, volatiles and the combustion products was modelled as a single incompressible fluid with constant molecular weight and specific heat. The analytical model was in good agreement with experimental values.

Based on this work, the first zonal model for cookstoves was published by Bussmann and Prasad, 1983. The zonal model identified 3 different zones in an open cooking fire:

1) Reacting fuel bed zone
2) Gas phase combustion zone
3) Heat transfer zone

The fuel bed model did not consider the pyrolysis rate of air or char combustion. The fuel consumption rate was determined from the heat release rate of the stove. The mass flow rate and the temperature of the exiting gases was found by the conservation of mass and energy respectively to the top of the fuel The fuel bed was assumed to be at a temperature of 1100 K.

In the gas phase combustion zone, the temperature, width and the velocity of the plume was determined based on the mass flow rate of the gases from the top of the fuel bed using co-relations developed by Bussman, 1982. Convective heat transfer coefficient for the bottom and the sides of the pot were obtained from analytical co-relations and was validated experimentally. Radiative heat transfer modelling assumed blackbody radiation between the fuel bed and the pot bottom. The heat transfer model under-predicted the heat transfer efficiency. The biggest success of this model was its success in coupling the different zones of a cooking fire. This formed the basis for much of the later works that followed.

Date, 1988 developed an analytical model for a stove with a nozzle on the lines of the model developed by Bussman and Prasad, 1983. This model was more detailed incorporating heat loss through the walls, radiation absorption in participating media etc. A detailed combustion model proposed by Shah, 2011 was included later on and the influence of various geometric design variables and operational parameters was investigated. In the heat transfer zone, experimental co-relations were used to determine heat transfer coefficient. The heat transfer efficiency predicted was 1.2% higher than experimental predictions.

Despite their accuracy the analytical models relied extensive for experimental data for heat transfer and other correlations. With the emergence of computational tools the analytical models find limited usage today. (MacCarty, 2013)

1.3.2. COMPUTATIONAL MODELS

The computational methods have largely relied on the analytical framework discussed previously. Therefore a detailed description of t efforts is not provided. Only some important efforts have been listed. Weerasinghe and Kumara, 2003 developed a CFD based coupled model for the gas phase combustion and heat transfer in a semi-enclosed cooking stove. The energy release was approximated by the eddy dissipation model in which the reaction rate of fuel combustion is taken as the slowest of the dissipation rates of fuel, oxygen and the products.

Gupta and Mittal, 2010 developed a 2D model incorporating the packed bed and the fuel zones in a single pan wood stove. Flow through the fuel bed is modelled as flow though a porous media. A uniform source term was introduced to account for the heat generation. 60% of the total energy release is assumed to be

from the flame while the remaining 40% of the energy release is from the fuel bed. The model was validated with two cases from literature.

Varunkumar, 2012 conducted a computational investigation into the gasification and combustion in a forced draft gasifier stove. Assumption of premixed combustion and mixed control chemical reactions was made. The flaming efficiency is in good agreement with the experimental values accurate upto 1%.

Therefore computational techniques have been successful in predicting the flow behavior and heat transfer characteristics in all types of stoves. With this brief overview, we now proceed to establish the approach that will be used in this analysis.

CURRENT APPROACH

As mentioned earlier, past cookstove modelling approaches have relied on zonal model to simplify analysis. In the zonal model, the cookstove is divided into different zones. The zonal model of a gasifier stove is shown in figure 1.3.

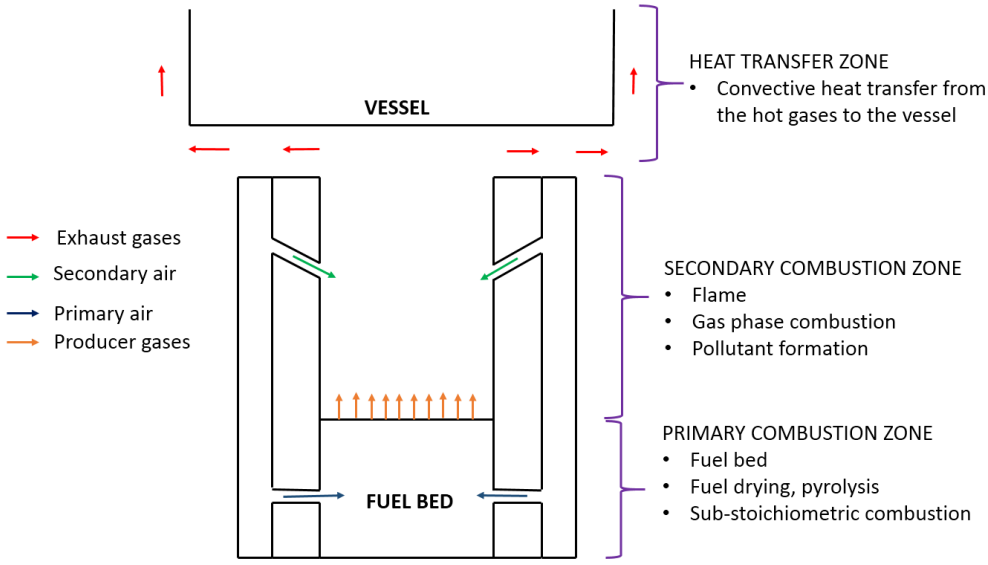

Figure 1.3: Zonal model of a gasifier stove

Figure 1.3 elucidates the different processes occurring in the stove. Modelling all these phenomena is computationally expensive and challenging in view of the time frame available. The objectives of the current assignment are restricted to understanding the fluid flow and heat transfer processes occurring in the secondary combustion zone. The contribution of the primary combustion zone to the fluid flow can be accounted for by specifying the mass flow and temperature of the producer gas at the top of the fuel bed. The fuel bed is therefore not part of the model.

And because the simulation model is expected to only inform and aid experimental design, a detailed modelling of the flame and pollutant formation is deemed to be beyond the scope of the current investigation. The current work thus focuses on modelling only the gas phase combustion and the heat transfer to the vessel.

Computational Fluid Dynamics (CFD) is the preferred tool in industrial simulations for fluid flows coupled with heat transfer (Versteeg and Malasekera, 1995). COMSOL Multiphysics, the preferred CFD tool in the Philips Research is used for this analysis.

Now that the scope of the analysis has been defined, we define the problem statement.

1.4. PROBLEM STATEMENT

The aim of the current assignment is to develop a CFD model that enables an investigation into the steady state flow and temperature fields in the secondary combustion zone of a forced draft micro-gasifier biomass cookstove. The analysis is done for a case when the stove is operating in the flaming mode with a flat bottomed cooking vessel placed on its top. The study also aims to study the mixing of the secondary air and producer gases rising from the fuel bed in the secondary combustion zone.

STRUCTURE OF THE REPORT

Now that the problem statement is defined, we proceed to the actual analysis. The first chapter is on the basic principles involved in the operation of a biomass micro-gasifier stove. The different aspects of a gasifier stove, ranging from its construction to the performance characteristics is analyzed. The later chapter focuses on the different aspects of the simulation model developed. A brief introduction to CFD and COMSOL Multiphysics is followed by an explanation of the equations used for the analysis. Then details about the actual implementation in COMSOL including the model geometry, boundary conditions, mesh used, order of discretization etc. are provided. A chapter analyzing the results obtained from the simulation follows. The discussion of the results leads us to the conclusion and recommendations for future work. The appendix among other things contains details about the validation study of the mesh used for the simulation.

2. Theory of Gasifier Stoves

In this chapter, the fundamental principles involved in the operation of the Philips woodstove is explained. The process of biomass combustion in a micro gasifier is described. This is followed by a section on the construction and operation of the Philips woodstove. There is a short description of the performance characteristics of different types of stoves. The chapter concludes with the comparison of the performance of different cookstoves available in the market today.

2.1. BIOMASS: COMPOSITION AND TYPES

Biomass is a term that refers to organic material originating from plants. Biomass is produced when plants convert the incident solar energy into chemical energy through photosynthesis and store it in form of chemical bonds (cellulose, hemicellulose and lignin).This stored energy can be converted into useful forms of energy in different ways. Biomass is an important source of energy contributing a significant 10-14% of the global energy supply. (McKendry, 2002).
There are different ways in which biomass can be classified. One method is based on the feedstock they are derived from. The prominent ones are:
1) Forestry products or residues
2) Agriculture waste and residues
3) Industrial and municipal organic wastes
4) Energy crops (McKendry, 2002)

The composition of biomass and therefore its properties as a fuel is strongly dependent on the feedstock. This can be seen in table 2.1 which provides the composition of different types of biomass along with that of coal.

	Wooden pellets **(Khan, De Jong et al,2009)**	Sewage sludge **(Nilsson, Gómez-Barea et al. 2012)**	Bituminous coal **(Kurkela and Ståhlberg 1992)**
Proximate analysis (weight%, as received basis)			
Volatile matter(VM)	80.4	47.2	7.6
Fixed carbon(FC)	14.5	4.7	87.7
Ash	0.2	39.4	2.8
Moisture	4.9	8.7	1.9
Ultimate analysis (weight %, dry ash free basis)			
C	45.6	54.3	91.6
H	6.6	7.7	3.5
O	47.8	27.4	2.4
N	-	8.4	1.6

Table 2.1: Composition of different biomass fuels and coal

The VM and the FC content is indicative of the ease of ignition and the subsequent gasification. Biomass fuels have significantly higher VM and lesser FC compared to coal. The higher oxygen content in biomass means that the carbon to oxygen ratio in biomass is lower than that of coal, leading to lower

calorific value. There is also significant ash content which has consequences for the overall handling and processing of biomass. Biomass fuels also have higher moisture content which influences the storage and also lowers the heating value of the fuel. (McKendry, 2002)

Biomass fuels can also be classified based on their physical characteristics such as shape, the state of existence etc.

Conversion of biomass to energy can be achieved through the following routes:

1) Thermochemical conversion – Combustion, pyrolysis, gasification and liquefaction
2) Biochemical/ biological conversion – digestion, fermentation (McKendry, 2002)

Only thermochemical conversion of biomass is discussed here. We start with an analysis of biomass combustion.

2.2. BIOMASS COMBUSTION

Combustion of biomass is a thermochemical process by which the energy stored in the chemical bonds of the biomass fuel is released as heat by means of oxidation. It is the most direct process to convert biomass into energy. It is a complex phenomenon involving many homogenous and heterogeneous reactions. It occurs in the following steps:

1) Drying
2) Pyrolysis
3) Combustion of volatile matter
4) Combustion of char (Roth, 2011)

Figure 2.1 gives a schematic explanation of the process of combustion.

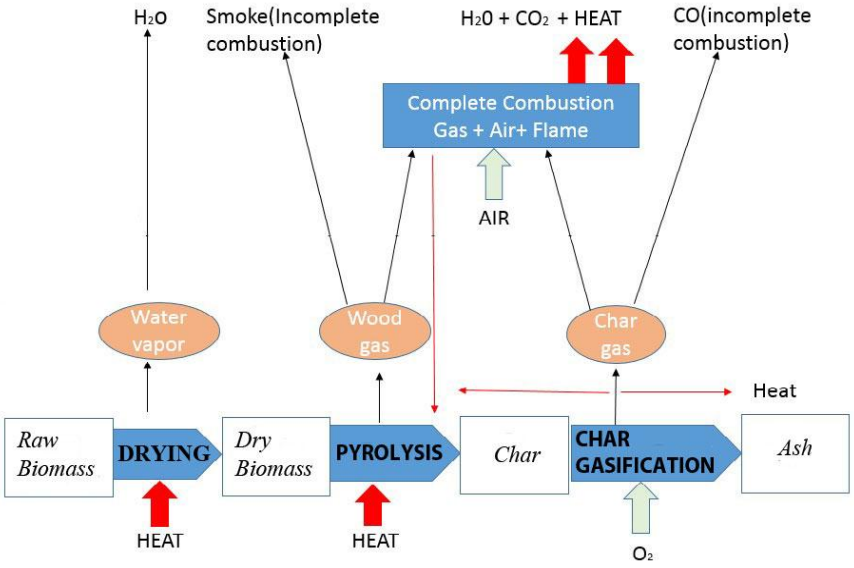

Figure 2.1: Biomass combustion (Roth, 2011)

To describe briefly, drying occurs when the moisture present in the biomass evaporates because of the heat generated by the combustion process. The dried biomass undergoes thermal decomposition at high

temperatures. This is termed pyrolysis. The volatiles vaporize, the heavier hydrocarbon molecules are converted into gases. This is an endothermic reaction requiring heat input. The released volatile matter then undergoes combustion at sufficiently high temperatures releasing heat in the process (a part of this heat is supplied for evaporation and pyrolysis) (Mando, 2013).

Once the volatile matter escapes a porous residue called char remains. Char undergoes oxidation at very high temperatures. Unlike pyrolysis, there is abundant supply of oxidizing agent during char oxidation. All these processes overlaps for most practical applications and a distinction is made only for better conceptual understanding. (Roth, 2011)

2.3. COMBUSTION IN A GASIFIER

Gasification is a thermochemical phenomenon in which a liquid or a solid fuel is converted into a combustible gas with the aid of an oxidizing agent at very high temperatures. Combustion in a gasifier differs from direct burning of biomass in that in a gasifier, the gas generation can be separated from the process of gas combustion. This is achieved by regulating the air supply to the different regions of the combustion zone. A better control over the combustion process is possible and consequently the combustion is cleaner with drastically reduced emissions compared to direct burning of biomass. (Roth, 2011)

The combustion of wood can be represented by the following expression

$$CH_{1.4}O_{0.6} + 1.05O_2 \rightarrow CO_2 + 0.7\ H_2O$$

(Lacrosse, 1990)

In a gasifier, the wood undergoes thermal decomposition to form gases which are then combusted to release energy. When air is supplied to oxidize biomass, the product gas from the devolatisation contains H_2, CO, CO_2, CH_4, H_2O and traces of longer chain hydrocarbons. The product gas is also referred to as producer gas (Mathieu and Dubuisson, 2002). The approximate composition is shown in Table 2.2.

Temperature	H_2 (% vol)	CO(% vol)	CH_4 (%vol)	CO_2(%vol)	C_{2+}(%vol)
988	16	54.3	12.8	12.8	4.1
1088	21.2	50.5	13.2	11.4	3.7
1188	26.4	46.8	12	11.5	3.3

Table 2.2: Wood gas composition (Mathieu and Dubuisson, 2002)

The gases generated undergo further oxidation forming water and carbon-di oxide. In case of incomplete combustion, carbon monoxide will be formed.

A schematic of the combustion process happening in a gasifier device is shown in figure 2.2.

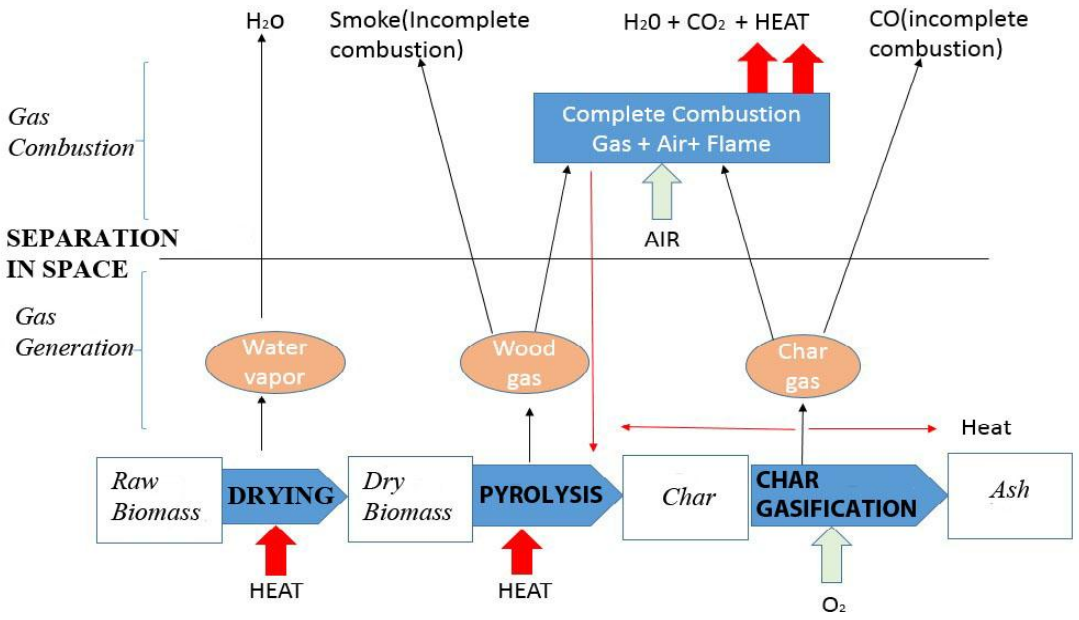

Figure 2.2: Combustion in a gasifier (Roth, 2011)

2.4. MICRO GASIFIERS

Gasifiers can be classified based on their application, the type of fuel used etc. When gasifiers are used for cooking applications they are referred to as micro-gasifiers. They are called so not only because they need to have significantly reduced dimensions to fit a cooking vessel on top of them, also because the power output required for cooking is in the range of 4-5kW. The challenge in designing these micro-gasifiers is to achieve sufficient control in a limited space (Roth, 2011).
A schematic of a micro gasifier is shown in figure 2.3.

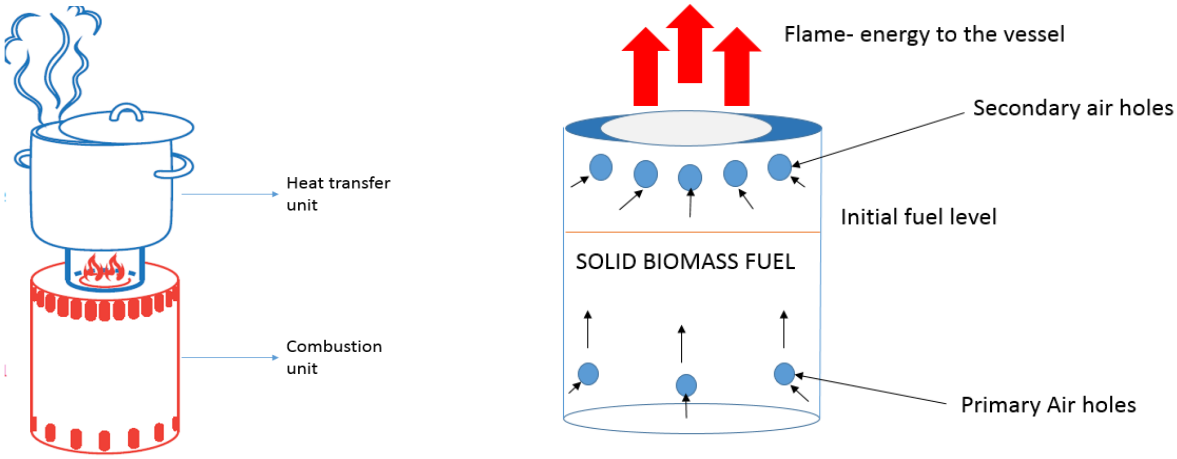

Figure 2.3: A micro-gasifier stove: Left) with a cooking vessel Right) Operation of the combustion unit

Gasifier stoves can either be natural draft or forced draft depending on the mode of air supply. If there is a fan forcing up the air through the combustion chamber it is a forced draft gasifier stove. If it relies only on natural draft, it is a natural draft gasifier stove (Roth, 2011).

The combustion unit consists of an insulated reactor containing the fuel and air supply ports. To separate the gas generation zone from the gas combustion zone, air is supplied at two different regions of the combustion chamber. The primary air holes are located at the bottom in the region of the fuel bed. The primary passes through the fuel bed to the flame front. The volatiles released undergoes oxidation with the primary air releasing heat. The primary air also supplies the air required for the gasification of char. Once all the volatiles have been released, char gasification is initiated.

Secondary air is introduced at the top of the combustion chamber to oxidize these gases. This is an exothermic process releasing energy which will be transferred to the heat transfer unit. The secondary air also contributes to the gasification of biomass. (Roth, 2011)

2.5. PHILIPS WOODSTOVE

The Philips woodstove was developed by Dr Paul van der Sluis of Philips research in 2004. It is a fan driven gasifier stove that can burn any kind of solid biomass without smoke. (Clean cooking catalog, 2012).

CONSTRUCTIONAL FEATURES

The Philips woodstove is composed of the following parts:

1) Combustion chamber
2) Fan assembly
3) Stainless steel body

The constructional features are shown in figure 2.4.

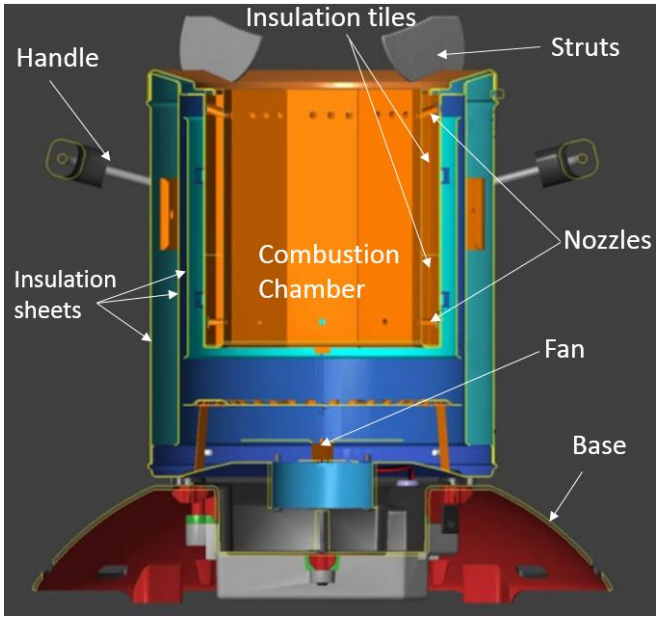

Figure 2.4: Philips woodstove-Constructional features

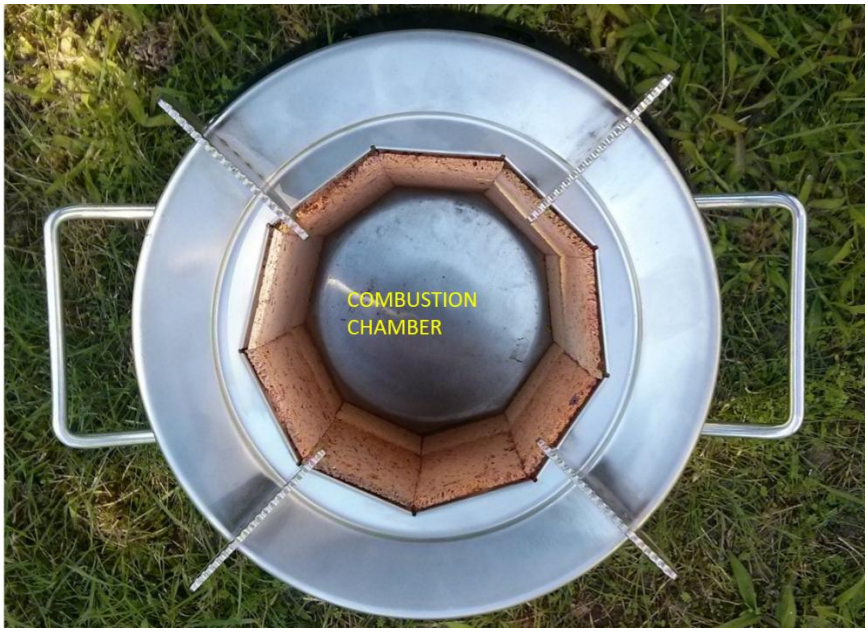

Figure 2.5: Philips woodstove-top view

Figure 2.5 shows the top view of the woodstove with no fuel loading. The arrangement of the insulation tiles can clearly been seen.

1) COMBUSTION CHAMBER

This is the region where the biomass is burnt. The metal walls of the chamber are lined with ceramic tiles to protect against the highly corrosive environment. These tiles are excellent insulators and minimize heat loss from the combustion chamber to the outer walls. (Van der Sluis, 2015)
There are two sets of tiles placed on top of each other. There are nine such set of tiles which form the combustion chamber (nine upper and nine lower tiles). These tiles are arranged in the shape of a regular nonagon (refer to figure 2.5). Holes drilled in these tiles serve as air nozzles.
There are two sets of nozzles

a) Primary air nozzles – formed by the holes in lower tiles in the combustion chamber. There is one hole per tile and thus there are nine primary nozzles in the stove located at the center of each tile.

b) Secondary nozzles – formed by holes in the upper tiles in the combustion chamber. There are three holes in each tile and 27 total nozzles in the stove. The secondary nozzles are inclined downwards into the combustion chamber. This sets up region of recirculation in the combustion chamber which contributes to better mixing of the fuel and air stream. This also ensures that the flame does not contact the cooking vessel directly avoiding soot deposition on the vessels. Periodic arrangement of tiles means that the air flow from the nozzles collide in the center of the combustion chamber (Van der Sluis, 2015).

2) FAN ASSEMBLY

The fan is placed at the bottom of the stove and is provided with an insulating casing to protect it from the high temperatures. The fan is powered by a 6V battery.

3) STAINLESS STEEL BODY

Cylindrical steel sheets separated by air gaps form the body of the stove. The air gaps are provided to insulate the exterior wall of the stove from the heat radiating from the combustion chamber. The combustion chamber is provided with struts to support the cooking vessel. (Van der Sluis, 2015)

WORKING PRINCIPLE

The air from the fan is guided into the nozzles through an annular chamber. The annular chamber is formed by the space between the combustion chamber and the insulation walls. The air is preheated as it rises up the annular chamber. The preheating of air in the annular chamber ensures that air enters the combustion chamber at high temperatures.

The primary air supplies the bulk of the air necessary for pyrolysis, while the secondary air provides the bulk of the air needed for secondary combustion and gasification. About 80% of the air flows in through the secondary nozzles and the rest 20% flows in through the primary nozzles. (Van der Sluis, 2015)

Now that the construction and operation of the stove has been described, we proceed to the performance comparison of gasifier stoves in general and the Philips woodstove in particular.

2.6. PERFORMANCE CHARACTERSTICS OF GASIFER STOVES

Gasifier stoves permit the use of proper air fuel ratios ensuring clean combustion. Consequently, forced draft stoves offer significant reduction in emissions and fuel consumption compared to open fire (Reed et al, 2004). A comparison of the emissions for different stoves when one liter of water is boiled for 30 minutes is shown in table 2.3.

Type	CO_2(g/L)	GWP of total PIC's(g/L)	Total GWP	PIC/total GWP
Three stone	536	193	729	26%
Charcoal	300	310	610	51%
Forced draft gasifier	277	8	284	3%

Table 2.3: Emissions comparison of stoves (MacCarty et al, 2007)
*** GWP-Global warming potential**
PIC-products of incomplete combustion.

The lower CO_2 emissions of the gasifier stove means a higher fuel efficiency. The PIC (products of incomplete combustion) count is substantially lower reaffirming the higher emission performance of the gasifer stove. On an average forced draft stoves reduce fuel consumption by 40% and emissions by around 90%. The high performing forced draft stoves move biomass up the energy ladder closer to the class of liquid fuels (MacCarty et al, 2010)

Realizing the need for a standard protocol an International Standards Organization (ISO), International Workshop agreement (IWA) was finalized. The IWA tiers of performance are interim international guidelines for stove performance, including efficiency, total emissions, indoor emissions, and safety. The IWA rating system was introduced to set aspirational goals for cook stove performance The IWA rating is based on four key performance indicators:

1) Fuel use/efficiency
2) Total emissions
3) Indoor emissions

4) Safety (Jetter, 2012)

Table 2.4 lists the key parameters that are used in the rating.

Tier 0	Tier 1	Tier 2	Tier 3	Tier 4

Performance indicator	Open fire	Target
Fuel use		
Specific energy consumption	0.050MJ/(min*L)	0.017 MJ/min*L)
Thermal efficiency	15%	45%
Emissions		
CO emissions(High power)	16 g/MJ delivered	8g/MJ delivered
PM 2.5 emissions(high power)	979 mg/MJ delivered	41 mg/MJ delivered
Indoor emissions		
CO emissions	0.97 g/min	0.42 g/min
PM 2.5 emissions	40 mg/min	2 mg/min

Table 2.4: IWA tiers for cook stoves (Jetter, 2012)

The open fire or direct burning of biomass forms the first tier. The Tier 4 category is the aspirational goal. Complete details of the IWA rating system is available in Jetter, 2012.

Figure 2.6 shows the emission comparison of different category of stoves.

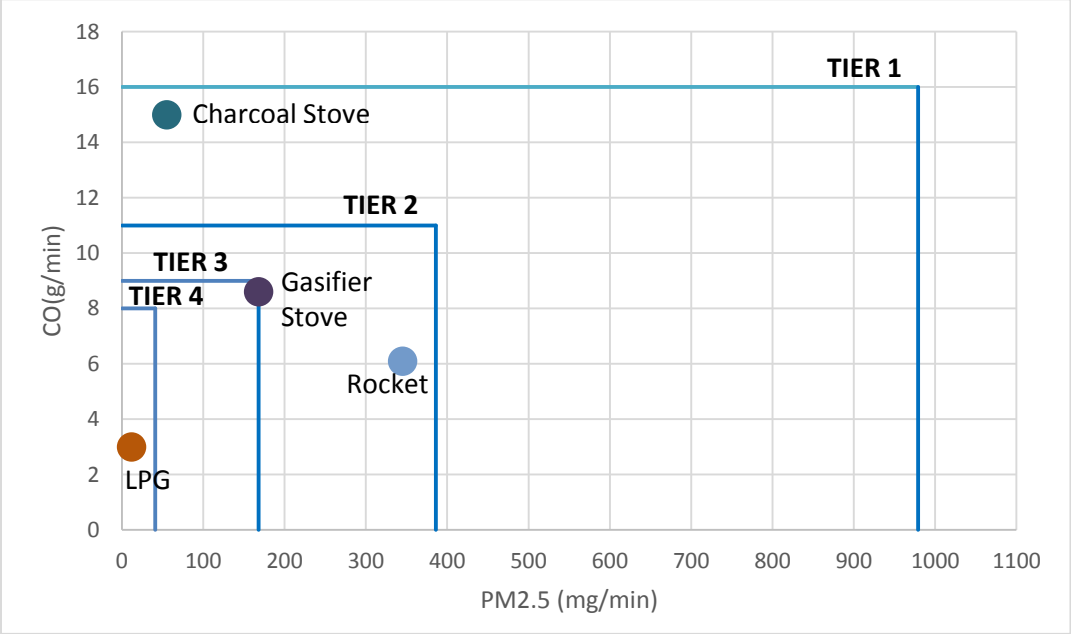

Figure 2.6: Stove emission (high power) comparison (Jetter, 2012)

Liquid Petroleum Gas (LPG) stoves lie in the tier 4 category. Gasifier stoves fall in the tier 3 category, charcoal stoves in the tier 1 category and rocket stoves in the tier 2 category. Amongst the biomass

burning stoves, gasifier stoves are closest to the aspirational tier 4 category highlighting the superior performance.

Gasifier stoves offer other advantages such as ease of operation, a steady hot flame and an ability to work well on all kind of biomass fuels. The limitations are that it requires changes in user behavior and practices. There are also significant cost and technology barriers involved preventing wider implementation of these stoves (Bhattacharya and Leone, 2005)

2.7. PERFORMANCE CHARACTERSITICS OF THE PHILIPS WOODSTOVE

Table 2.5 provides some of the key performance characteristics of the Philips woodstove.

Performance indicator	Value
Fuel use	
Thermal efficiency (high power)	38.4%-39.4%
Emissions	
CO emissions (g/MJ delivered)	0.98-2.71
PM 2.5 emissions **(**mg/MJ delivered)	62.3-147.3
Indoor emissions	
CO emissions	0.08-0.21 g/min
PM 2.5 emissions	4.70 -9.09 mg/min
Output	
Cold start firepower	4 -4.5 kW
Hot start fire power	4.9 -5.1 kW
Mean time to boil	17.2 -18.1 minutes

Table 2.5: Performance parameters of the Philips woodstove (Clean cooking catalog, 2012)

Figure 2.6 shows the Carbon Monoxide and the PM 2.5 emissions of different stoves. The Philips woodstove has significantly lower emissions amongst all category of stoves.

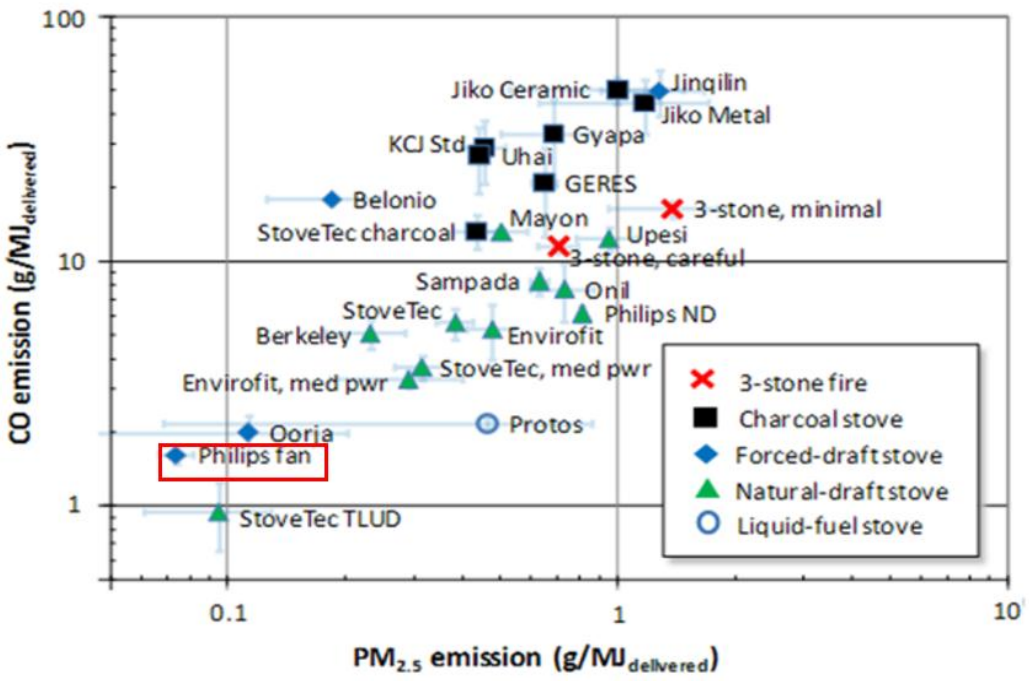

Figure 2.7: CO emissions for different stoves (Jetter et al, 2012)

Figure 2.7 shows the efficiency comparison of different stoves. Even in terms of efficiency the Philips woodstove has higher efficiencies than most other stoves.

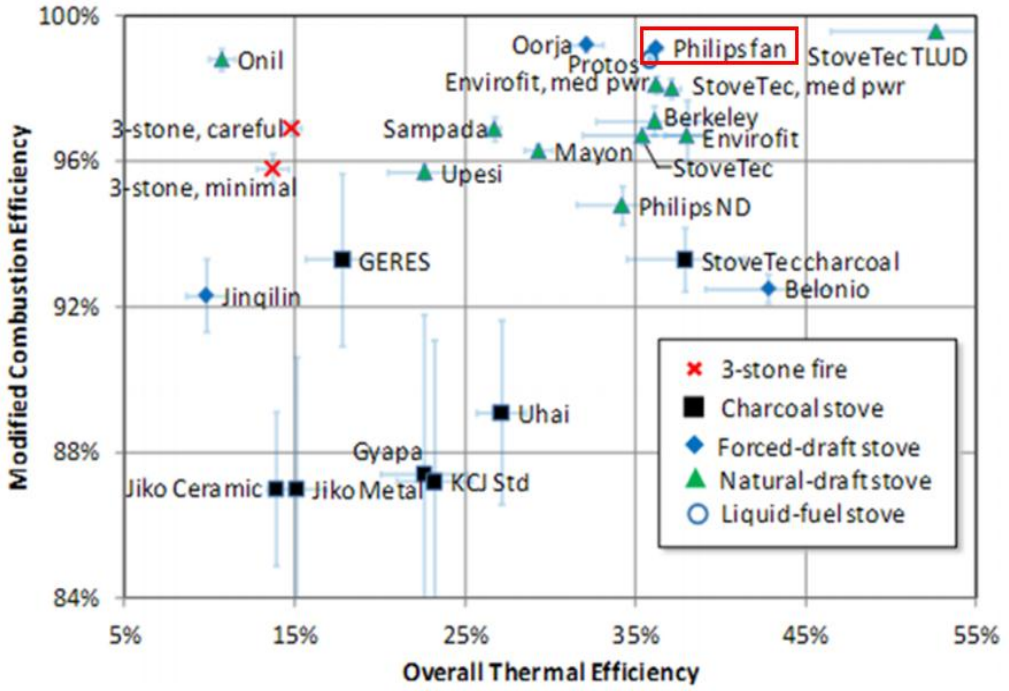

Figure 2.8: Efficiency comparison (Jetter et al, 2012)

Chapter 3. Simulations

This chapter focuses on the different aspects of the simulation model developed. A brief introduction to COMSOL Multiphysics, the software being used is followed by an explanation of the physics and the equations used. This is followed by a section on the implementation in COMSOL where the geometry, the mesh used and other relevant details are discussed.

3.1. INTRODUCTION

The Computational Fluid Dynamics (CFD) module in COMSOL is a commercially available package that can be used to simulate a variety of flows. It provides an opportunity to couple the fluid flow to a wide range of physical processes. The solvers and the built in meshes are well suited for most fluid applications and are numerically robust. (COMSOL CFD user guide, 2013)

COMSOL is a finite element (FEM) solver. FEM is a numerical technique used to solve for a boundary value problem described by a differential equation. FEM makes use of interpolation functions to obtain the solution. The interpolation function based on the governing differential equations, approximates the behavior of the variable within individual elements. Part of the interpolation function is solved at each node individually and the solutions are then added to find the value of the variable in the interpolation function for that mesh element. (Cook, 2007)

Since the solutions are based on individual meshes elements, the distance between the nodes has a direct impact on the quality of the solution. A better refined mesh will return a better solution. However, this comes with the cost of increased computational effort and time.

FEM has emerged as a powerful numerical method with applications in different fields. Ability to deal with complex geometries and consistent treatment of the boundary conditions are the biggest advantages offered by FEM. (Zienkiewicz and Taylor, 2000) (Cook, 2007)

Classical finite element formulations are based on the principle of minimum potential energy which cannot be extended to heat transfer and fluid flow problems. For fluid flow problems, the Galerkin-Ritz method is employed. (Zienkiewicz et al, 2005) (Donea and Huerta, 2003)

3.2. PHYSICS

The flow in the secondary combustion zone of the stove is non –isothermal characterized by the presence of large temperature gradients. The non-isothermal flow module in COMSOL Multiphysics is designed for such situations where the fluid flow is strongly coupled to heat transfer. The module solves the Navier-Stokes equation and an additional energy balance equation. (COMSOL CFD User's guide, 2013).The non-isothermal flow module is used for simulations and the equations used are described in the following section.

3.2.1. FLUID FLOW EQUATIONS

There are three fundamental conservation laws governing the fluid flow behavior. They are

1) Mass
2) Momentum
3) Energy.

These equations are central to understanding the dynamic behavior of a fluid. Each of them is briefly described below.

3.2.1.1. MASS CONSERVATION

The mass conservation law states that the rate of increase of mass flow through a control volume is equal to the rate of inflow through the boundaries. (Kundu and Cohen, 2008)

In differential form it is expressed as:

$$\frac{\partial \rho}{\partial t} + \nabla \cdot (\rho u) = 0$$

Where
ρ - density of the fluid, $Kg.m^{-3}$
u – velocity vector, ms^{-1}
(Zienkiewicz et al, 2005).

For a stationary analysis, the equation reduces to

$$\nabla \cdot (\rho u) = 0$$

3.2.1.2. MOMENTUM CONSERVATION

The momentum conservation equation is a generalized form of the Newton's second law defining the motion of a fluid. It is obtained by balancing the forces acting on the fluid element. The Newton's second law can be expressed as:

$$F_i = \sum F = \rho \iiint_V \frac{D(u_i)}{Dt} dV$$

Where F_i represents the resultant of all the forces acting on the volume V. The forces acting on a fluid element can be categorized into body forces and surface forces. The total force acting on the fluid element can also be expressed as the sum of the two:

$$F_i = F_{vol} + F_{surface} \quad \text{..... E3.1}$$

1) Volume forces: Body or volume forces act over the entire volume and are proportional to the volume of the element. Only the gravitational force is considered for this analysis. It is expressed as:

$$F_{vol} = \iiint_V \rho g dV$$

2) Surface forces: Surface forces act at the surface level and are proportional to the area of the surface on which they are acting. The surface forces consist of the shear stresses and the normal stresses that act on a fluid element. If τ_{ij} represents the deviatoric stress tensor of the fluid element, the surface forces can be expressed as

$$F_{surface} = \iint_S \tau_{ij} n_j dS$$

Substituting the surface and volume force expressions in equation E3.1, we obtain

$$\rho \iiint_V \frac{Du_i}{Dt} dV = \iiint_V \rho g dV + \iint_S \tau_{ij} n_j dS$$

(Kundu and Cohen, 2008).

Expressing the stress tensor in terms of the deformation or the strain rates of the element and by using divergence formula the equation reduces to the form:

$$\rho \frac{\partial u}{\partial t} + \rho u \cdot \nabla u = \rho g - \nabla p + \nabla \cdot (\mu(\nabla u + (\nabla u)^T) - \left(\frac{2}{3}\right)\mu(\nabla \cdot u)I$$

This is the Navier-Stokes equation for a compressible Newtonian fluid.
(COMSOL CFD User's guide, 2013) (Zienkiewicz et al, 2005)

For a stationary case,

$$\rho u \cdot \nabla u = \rho g - \nabla p + \nabla \cdot (\mu(\nabla u + (\nabla u)^T) - \left(\frac{2}{3}\right)\mu(\nabla \cdot u)I$$

When the flow makes a transition to turbulence, the fluid properties become invariant in space and time. Turbulent flow is chaotic, characterized by the presence of diverse range of length and time scales (Pope, 2000). The Navier-Stokes equation is applicable for this case too, but the diverse scales of flow make the solution difficult.

Several numerical methods have been proposed to model turbulent flows. CFD methods like Direct Numerical Schemes (DNS) attempt to completely resolve all the flow scales. In another technique called the Large Eddy Simulation (LES), only the larger scales are resolved while smaller scales are only modelled. For practical engineering applications the computational requirements for both these techniques are formidable. (Pope, 2000)(Cengel and Cimbala, 2006)

An alternative is to use the Reynolds Averaged Navier-Stokes equation which incorporates additional equations to account for the mixing and transport by the turbulent eddies. In this method, the fluid properties are divided into an averaged value and a fluctuating part. Any scalar quantity of flow, $\emptyset$ is decomposed and expressed as:

$$\emptyset = \overline{\emptyset} + \emptyset"$$

where $\overline{\emptyset}$ represents the averaged component and $\emptyset"$ represents the fluctuating component. Expressing the terms in the Navier-Stokes equations in this form leads to the Reynolds averaged Navier-Stokes equation.

$$\rho u \cdot \nabla u = \rho g - \nabla p + \nabla \cdot (\mu(\nabla u + (\nabla u)^T) - \left(\frac{2}{3}\right)\mu(\nabla \cdot u)I - (\overline{\rho u_j" u_i"})$$

(COMSOL CFD User's guide, 2013)

The equation is similar to the Navier-Stokes equation for laminar flow case except for an addition $\overline{\rho u_j" u_i"}$ term. This term represents the Reynolds stresses acting on the fluid element.

The *k-ω* model is chosen for this simulation. In this model the Reynolds stress tensor is expressed as:

$$\overline{\rho u_j" u_i"} = \nabla.(\mu_t(\nabla u + (\nabla u)^T) - \left(\frac{2}{3}\right)(\mu_t(\nabla \cdot u)I + \rho k I) \text{ (Wilcox, 1993)}$$

The motivation for the choice of the turbulence model is provided in section 3.4.

Substituting this in the Navier-Stokes equation and on rearranging, we obtain:

$$\rho u \cdot \nabla u = \rho g - \nabla p + \nabla \cdot \left((\mu + \mu_t)(\nabla u + (\nabla u)^T) - \left(\frac{2}{3}\right)(\mu + \mu_t)(\nabla \cdot u)I\right) - \left(\frac{2}{3}\right)\rho k I$$

Where,
μ_t – turbulence viscosity, Pa-s
k- turbulent kinetic energy, m^2s^{-2}
ω – turbulent dissipation rate, s^{-1}

(COMSOL CFD User's guide, 2013)

The additional equations to be solved for are:

$$\mu_t = \rho(\frac{k}{\omega})$$

The additional transport equation for the turbulent kinetic energy is:

$$\rho(u \cdot \nabla)\mathrm{k} = (\nabla \cdot [(\mu + \mu_t \sigma_k^*)\nabla \mathrm{k}] + \mathrm{P_k} - \rho\beta_0^* k\omega)$$

The additional transport equation for the turbulent dissipation rate is:

$$\rho(u \cdot \nabla)\omega = (\nabla \cdot [\left(\mu + \mu_t \sigma_\omega^*\right)\nabla\omega] + \alpha(\frac{\omega}{\mathrm{k}})\mathrm{P_k} - \rho\beta_0^*\omega^2\Big)$$

Where the production term, P_k is expressed as

$$P_k = \mu_t[\nabla \mathrm{u}:\left(\nabla \mathrm{u} + (\nabla \mathrm{u})^{\mathrm{T}}\right) - \left(\frac{2}{3}\right)(\nabla \cdot \mathrm{u})^2] - (\tfrac{2}{3})\rho \mathrm{k}\nabla \cdot \mathrm{u}$$

Where α, β, σ, σ* and β* are numerical constants. (Wilcox, 1993)

The momentum equation for both laminar and turbulent flow have been described in this section. Apart from this, an additional energy equation term is also to be solved for. Since the energy equation has heat transfer terms, a brief overview of the different modes of heat transfer is provided in the following section.

3.2.2. HEAT TRANSFER

Heat transfer is a mode of energy transfer that is driven by temperature gradients. There are three modes of heat transfer.
1) Conduction
2) Convection
3) Radiation

In the gasifier stove, there is heat transfer by all the three modes mentioned. We describe each of them briefly below.

3.2.2.1. CONDUCTION

Conduction is the energy transfer from the higher energy particles to the neighboring lower energy particles caused by the interaction between them. In liquids and gases conduction of heat is due to the collision because of the random motion of particles, while in solids it is by the transport of free electrons through the crystal lattice.
Conductive heat transfer is governed by the Fourier law which can be expressed as

$$Q = -k_t A \nabla T = -k_t A \frac{\partial T}{\partial n} n$$

Where,
Q – Heat flux, W
k_t –thermal conductivity, W/m K
T – temperature, K
A- area, m^2
n- unit vector in the direction of heat transfer

The negative sign indicates that the heat transfer is in the direction of decreasing temperature magnitude. Also the heat flux is in a direction perpendicular to the isotherm. The Fourier law illustrates that heat transfer by conduction is an isotropic phenomena. It is also the expression that defines the thermal conductivity of the material. The law is applicable to solids, liquids and gases. Heat transfer by conduction is the dominant mode of heat transfer in solids. (Bergman et al, 2011)

3.2.2.2. CONVECTION

Convective heat transfer is a mode of energy transfer between a fluid and a solid surface due to the combination of conduction and bulk fluid motion. It can be viewed as a special case of conduction with additional fluid motion.

The formation of boundary layers is a characteristic of convective heat transfer. The interaction between the fluid and the solid surface sets up a velocity boundary layer. If the temperatures of fluid and the surface are different a thermal boundary layer is also set up. The properties of these boundary layers significantly influence the rate of heat transfer.

The rate of convective heat transfer can be represented by Newton's law of cooling. It is expressed as

$$Q_{conv} = hA(T_{sur} - T_{\infty})$$

Where,
Q_{conv}– Convective heat flux, W
h -average convection heat transfer coefficient, W/m^2 K
A - area of heat transfer, m^2
T_{sur} - temperature of the surface, K
T_{∞}- temperature of fluid at a distance from the surface, K

The heat transfer coefficient depends on the velocity and the thermal boundary layers, which in turn are dependent on the surface geometry, fluid properties and the nature of the flow.

An expression for the heat transfer coefficient may be obtained by considering the heat transfer at the solid surface where only conduction occurs. Equating the Fourier law with the Newton's law of cooling the following expression is obtained

$$h = \frac{-k_t \left(\left(\frac{\partial T}{\partial y} \right)_{y=0} \right)}{T_{sur} - T_{\infty}}$$

Determining the heat transfer coefficient is central to solving convection heat transfer problems and for most cases it can only be determined experimentally (Bergman et al, 2011).

3.2.2.3. RADIATION

Thermal radiation is the energy emitted by bodies because of their temperature. This is caused by the changes in the electronic configuration of the materials. The emitted energy travels in the form of electromagnetic waves. Unlike conduction and convection, radiation does not need any medium for propagation. The radiation emitted from a surface is governed by the Stefan Boltzmann's law which can be expressed as

$$E = \varepsilon \sigma T_{sur}^4$$

Where,
E_r = Surface emissive power, W/m^2
σ = Stefan Boltzmann's constant, $Wm^{-2}K^{-4}$
T_{sur} = Absolute temperature of the surface, K.
ε =emissivity, whose values lie in between 0 and 1. (1 for a perfect blackbody)

When the surface is enclosed by another surface at a temperature T_{amb}, the heat transfer between the two surfaces is given by:

$$E_r = \varepsilon \sigma (T_{sur}^4 - T_{amb}^4)$$

The total radiation incident on a surface is called the irradiation. This irradiation can either be transmitted, reflected or absorbed. That is

$$G_{incident} = \alpha G_{incident} + \rho_r G_{incident} + \tau_r G_{incident}$$

Where,
G = irradiation, W/m^2
α = Absorptivity of the surface
ρ_r= reflectivity of surface
τ_r= Transmissivity of the surface

The last three are radiative properties of the surface having values between 0 and 1. It follows that

$$\alpha + \rho_r + \tau_r = 1$$

The net radiation leaving a surface is called the radiosity 'J'. It is expressed as

$$J = E_r + \rho_r G_{incident}$$

Where 'J' = Radiosity, W/m^2
The net radiation flux from a surface will be the difference between emitted and the absorbed radiation. Ignoring transmissivity this can be expressed as

$$q" = J - G = E_r - \alpha G$$

The net radiation flux has the units of W/m^2 (Bergman et al, 2011).

3.2.2.4. VIEW FACTORS

Radiation between surfaces is an important phenomena seen in a lot of practical applications. The directional nature of radiation needs to be accounted for in analyzing this. This is done by the use of a 'view factor', also referred to as 'shape factor' or 'configuration factor'.

The view factor is a geometric entity independent of the material properties or the temperature. If 'i' and 'j' are the two surfaces between whom there is radiation exchange, the view factor F_{ij} is the fraction of radiated emitted by surface 'i' that is incident on the surface 'j'.

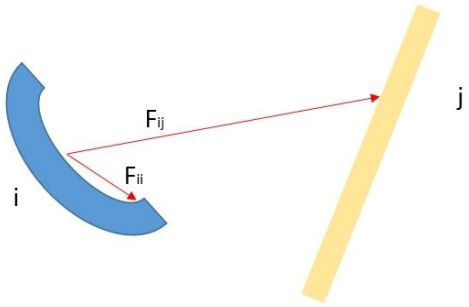

Figure 3.1: View factor between surfaces

Mathematically this is expressed as

$$F_{ij} = \frac{q_{ij}}{AJ}$$

Where,
q_{ij} - radiative flux, W/m^2
J - Radiosity, W/m^2
A - Area of the surface, m^2

The view factor is calculated using the following expression

$$F_{ij} = (\frac{1}{A_i}) \int_{A_i} \int_{A_j} \frac{cos\theta_i * cos\theta_j}{\pi R^2} dA_i dA_j$$

Where, dA_i and dA_j are the elemental areas on each surface

θ_i and θ_j are the polar angles formed by the areas with the line connecting them

R- distance between the two areas.

On the same lines

$$F_{ji} = \left(\frac{1}{A_j}\right) \int_{A_i} \int_{A_j} \frac{cos\theta_i * cos\theta_j}{\pi R^2} dA_i dA_j$$

The net radiation flux and the radiosity between surfaces can be calculated using the principles explained earlier. There will be only be additional view factor relationship in each of these relations.
For example the net radiation flux can be expressed as

$$q" = F_{ij}(E - \alpha G)$$ (Bergman et al, 2011)

With the basic heat transfer equations now explained, we now proceed to the thermal energy equation for a fluid also referred to as the heat equation.

3.2.3. THERMAL ENERGY EQUATION

The thermal energy equation is obtained from the first law of conservation of energy. The equation is of the form:

$$\rho C_p \frac{DT}{Dt} = -(\nabla . \mathrm{q}) + Q + Q_{vh} \quad + W_{pressue}$$

Where,
C_p- specific heat capacity at constant pressure, J/Kg. K
T- absolute temperature, K
q - heat flux due to conduction, W/m^2
Q- heat source other than viscous heating, W/m^3
Q_{vh}- viscous heating term
$W_{pressure}$ - pressure work
(COMSOL CFD User's guide, 2013)

The heat flux due to heat conduction can be expressed as,

$$q = -k_t \nabla T$$

Viscous heating refers to the transformation of mechanical energy of the fluid into internal energy due to viscous effects (action of shear forces) (Morini, 2014). It represents the rate of viscous dissipation of kinetic energy. The viscous heating can be expressed using tensors as,

$$Q_{vh} = 2\mu \left[e_{ij} - \left(\frac{1}{3}\right) \mu (\nabla . u) \delta_{ij} \right]^2$$

(Kundu and Cohen, 2008)

The pressure work term refers to the reversible conversion of work into heat by the pressure in the fluid (COMSOL CFD User's guide, 2013). It represents the contribution of pressure to the deformation work (Kundu and Cohen, 2008).

It is expressed as:

$$W_{pressure} = (\frac{T}{\rho})\frac{\partial \rho}{\partial T}\Big|_p (\frac{\partial p}{\partial t} + (u.\nabla)\mathrm{p})$$

(COMSOL CFD User's guide, 2013)

3.2.4. EQUATION OF STATE

Along with the energy equation, an additional equation of state also needs to be solved for. The equation of state relates the pressure, density and the temperature of a gas. For an ideal gas it takes the form:

$$\rho = \frac{P}{R_u T}$$

Where,
P - Pressure of the fluid, Pa
ρ - Density of the fluid, Kg. m^{-3}
R_u- Universal gas constant, $Pa.m^3\,Kg^{-1}K^{-1}$
T - Temperature, K(Zienkiewicz et al, 2005)

With all the necessary equations now established, we now focus on developing the geometry of the simulation model.

3.3. COMPUTATIONAL DOMAIN

The top view of the combustion chamber with the tiles numbered is provided in Figure 3.2

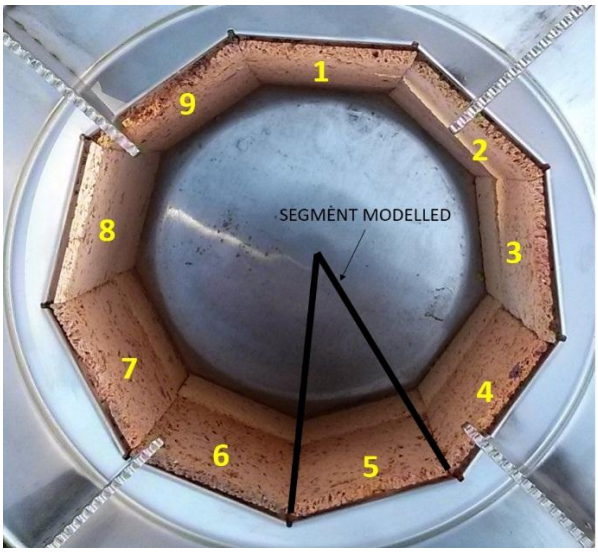

Figure 3.2: Computational domain

Also seen in figure 3.2 is the segment modelled. The computational domain is restricted to one tile. This is for the sake of computational efficiency. The effects of the neighboring domains are accounted for by using a periodic boundary condition

The domain can be any of the nine tiles. Tile 5 is highlighted in figure 3.2 is for the sake of clarity.

Some of the major assumptions made in defining the geometry are:

- Since only the secondary combustion zone is considered, the fuel bed is not modelled. It is assumed that the stove is half loaded with fuel.
- The model is developed for a case when there is a flat bottomed vessel placed on the top of the stove. The walls of the vessel are assumed to be at a temperature of 373 K.
- Detailed design of the insulation sheets has not been included to reduce the computational effort. Also details like the struts provided to support the vessel has not been included.
- The width of the ambient air segment is chosen so as to avoid any recirculation of hot gases exiting the stove

The computational domain with the different components and some important dimensions are shown in figure 3.3.

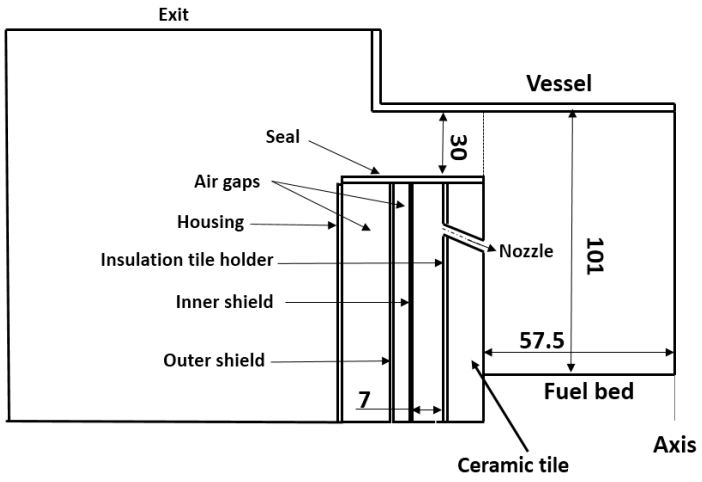

Figure 3.3: Computational domain-components (dimensions in mm)

The dimensions of the ceramic tile is provided in figure 3.4.

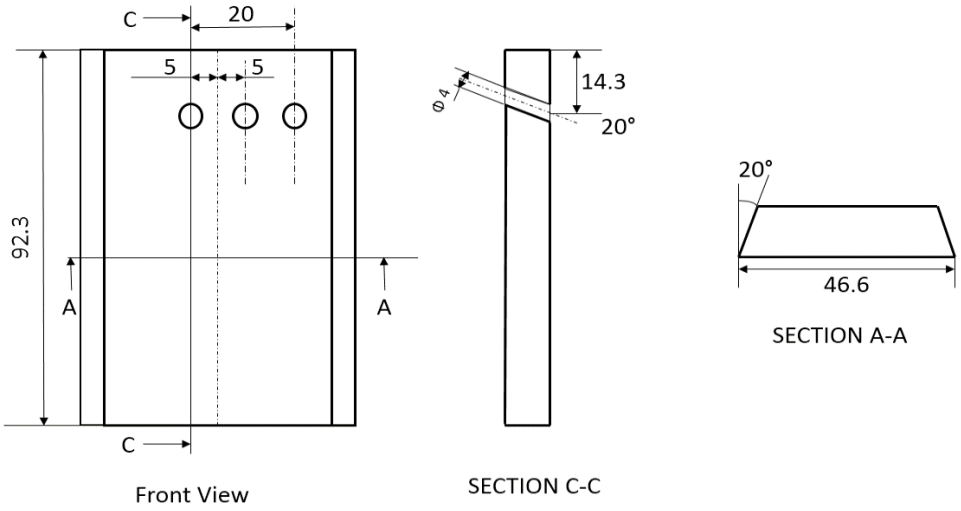

Figure 3.4: Insulation tiles –dimensions (in mm)

The 3 dimensional geometry developed with the details mentioned above is shown in figure 3.5.

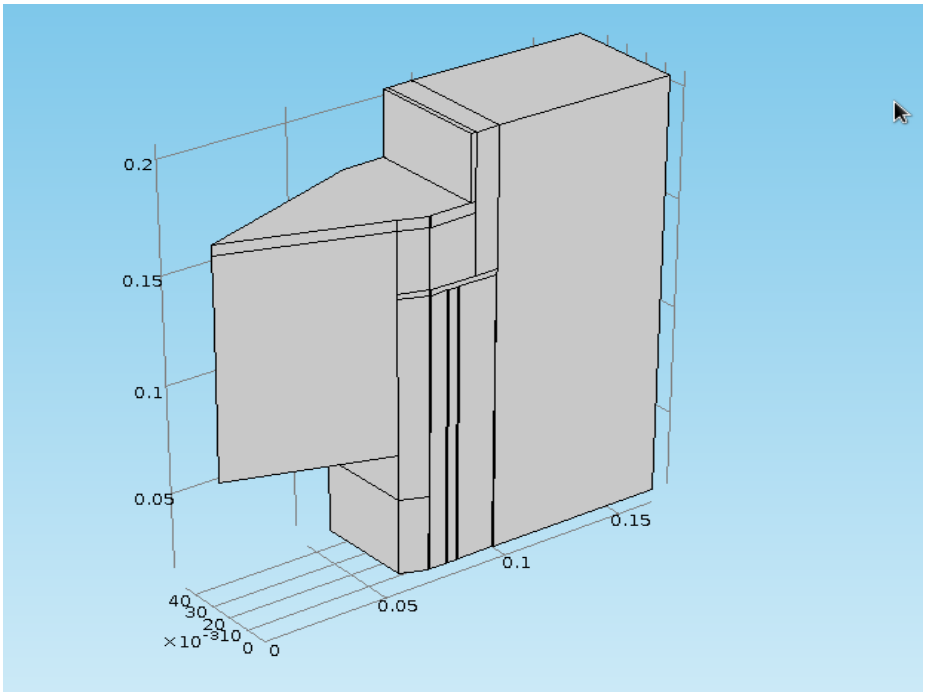

Figure 3.5: Model geometry

The top view of the geometry is shown in figure 3.6. Noticeable is that the geometry represents a circular segment only till the ceramic tiles.

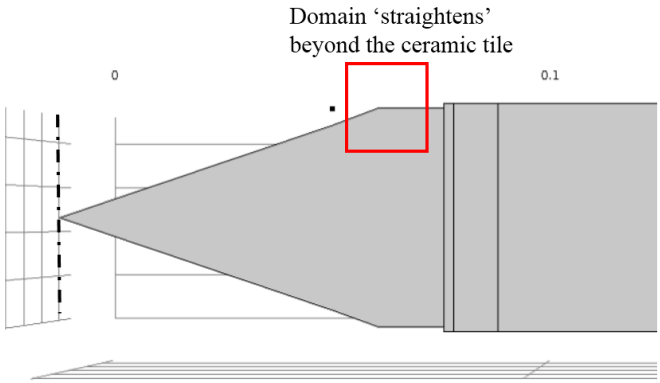

Figure 3.6: Computational domain -top view

The geometry of the regions lying beyond the ceramic tiles, i.e. the annular chamber, the insulation sheets, air gaps and the ambient air, is constructed using rectangular blocks. This brings down the computational effort substantially. This is not expected to impact the fluid flow pattern or the temperature profiles significantly.

3.4. TURBULENCE MODEL

It will be shown in the later sections that the flow in the nozzles can make a transition to turbulence or transitional flow. Therefore use of turbulence models is necessary. The *k- ω* model is chosen as it provides a better treatment of flows near the wall and is suited for flows close to the transition Reynolds number. It can also reliably predict the spreading rate of jets making it very relevant to the current modelling effort. (Wilcox, 1993)

3.5. MATERIALS

In this section, the materials specified for the different stove components and some of their important properties are stated.

3.5.1. INSULATION CHAMBER

The ceramic tiles are made of low lime, highly insulating concrete which can withstand high temperatures and corrosion. Some important properties of the tile are given in table 3.1.

Property	Value
Bulk Density	1340 Kg/m^3
Maximum temperature	1320°C
Thermal conductivity(mean)	0.34 $Wm^{-1} K^{-1}$

Table 3.1: Material Properties of the ceramic tile (Morgan Thermal Ceramics, Firelite LWHS datasheet)

The thermal conductivity value stated in table 3.1 is the mean of 5 values measured from 200°C to 1000°C.

3.5.2. STEEL

Steel is the material specified for the insulation sheets, the vessel and the seal. Some important properties of the material used are stated in table 3.2.

Property	Value
Density	7850 Kg/m^3
Heat capacity at constant pressure	475 J/Kg.K
Thermal conductivity(mean)	44 W/mK

Table 3.2: Material properties of steel used (COMSOL material library)

3.5.3. AIR

Air is the material specified for the fluid phase occurring in the domain. Even the producer gas rising from the fuel bed is specified as air. The properties of air available from the COMSOL materials library is used.

3.6. BOUNDARY CONDITIONS

Figure 3.7 shows the different boundary conditions used in the domain.

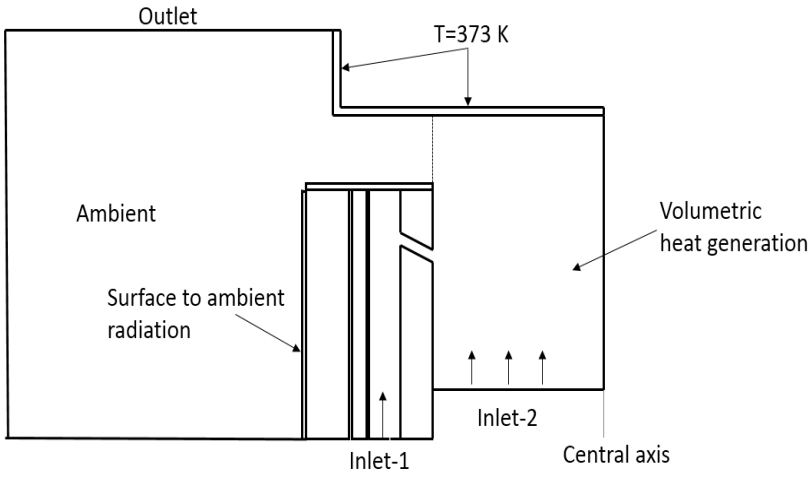

Figure 3.7: Boundary conditions

Below we describe each of the boundary condition listed in figure 3.7.

3.6.1. INLET 1

This is the air inlet into the annular chamber. The flow properties of the entering air, specifically air flow rate needs to be established.
The following experimental results on the airflow rates in the stove are available :

a) The air flow rate for the entire stove= 2.5 *10^{-3} m^3/s
Therefore the flow rate through each domain is 1/9th of the total value, i.e. $V = 0.2778 * 10^{-3} m^3/s$

The density of air at 298K(entering air temperature), ρ=1.185 kg/m^3. Therefore the mass flow rate of air through the stove is

$$W_{air} = V * \rho = 0.329 * 10^{-3}\ kg/s$$

Since the primary nozzles are not modelled, only the secondary air flow needs to be considered. No physical measurements on the proportion of the primary and secondary air is available. To avail these values, a simulation mimicking the test conditions, i.e. with no fuel loading is carried out. The results of the simulation established that around 81% of the air enters the secondary nozzles and the remaining 19% enters the primary nozzles.

The secondary air flow rate is $V_s = 0.81 * 0.2778 * 10^{-3} = 0.225 * 10^{-3}\ m^3/s$

On the same lines, the mass flow rate, $W_s = 0.81 * 0.329 * 10^{-3} = 0.26649 * 10^{-3}\ kg/s$

Similar calculation is repeated for primary air flow:

The primary air flow rate is $V_s = 0.19 * 0.2778 * 10^{-3} = 0.05272 * 10^{-3}\ m^3/s$

On the same lines, the mass flow rate, $W_s = 0.19 * 0.329 * 10^{-3} = 0.06251 * 10^{-3}\ kg/s$

Only the flow of secondary air is considered at the annular chamber. The mass flow boundary condition presents itself as the most convenient boundary condition at the inlet. However, convergence with a pressure boundary condition is easier compared to a mass flow or a velocity boundary condition. It is therefore decided to implement a pressure boundary condition for inlet 1.

The pressure of the flow is obtained from the fan curve. With the calculated secondary air flow rate, the corresponding pressure is calculated from the fan curve. From the fan curve, the corresponding pressure for the calculated secondary air flow rate is around 30 Pa. A copy of the fan curve is provided in appendix A.

NOTE: *It has now been realized that this boundary condition is not accurate. With a pressure of 30 Pa, the mass flow rate at the secondary nozzles is only 43% of the actual value (refer table 4.1). With limited time at disposal to make the necessary changes, the results obtained using inlet pressure of 30Pa have been retained. However, some initial results of the simulation with a higher inlet pressure, and consequently a higher mass flow (60%of the actual value) have been included. Only a skeletal analysis is provided for this case in 4.1.7.*

Here we deviate slightly from the inlet boundary condition to establish the regime of flow. In section 3.4, it was stated that turbulence models become necessary as flow can be in the transitional/ turbulent regime. With the flow rates now available a rough estimation of the Reynolds number can be obtained. Since there are three nozzles, that the flow from the annular chamber is divided almost equally among the three nozzles. The flow rate through each of the nozzle will be

$$V_{noz} = 0.33 * V_s = 0.07425 * 10^{-3} m^3/s$$

The cross sectional area of each nozzle

$$A_{noz} = \frac{\pi}{4} * (d_{noz})^2 = 12.57 * 10^{-6} m^2$$

Now since the flow rate is the product of the cross sectional area and the flow velocity, the flow velocity

$$U_{noz} = \left(\frac{V_{noz}}{A_{noz}}\right) = 5.9\ m/s$$

The Reynolds number for this velocity can be calculated as:

$$Re = \frac{\rho U_{noz} d}{\mu}$$

Where,
ρ – Density of the fluid, Kg/m^3
U_{noz}- Velocity of fluid through nozzles, m/s
d- Diameter of the jet, m
μ - Dynamic viscosity, Pa.s

The air gets heated as it rises up the annular chamber. The exact temperature rise can be obtained only from simulations. We assume that the air at the nozzle inlet is around 350K. For 350 K, the values of

density and dynamic viscosity are ρ=1.009 Kg/ m^3 and μ=2.075*10^{-5} Pa.s. Therefore the Reynolds number of the air flow at the inlet of the nozzle is around 1150.

The Reynolds number will further increase as it accelerates inside the nozzle. An air jet exiting the nozzles at a Reynolds number of close to 1000 can be in the turbulent or the transitional regime.

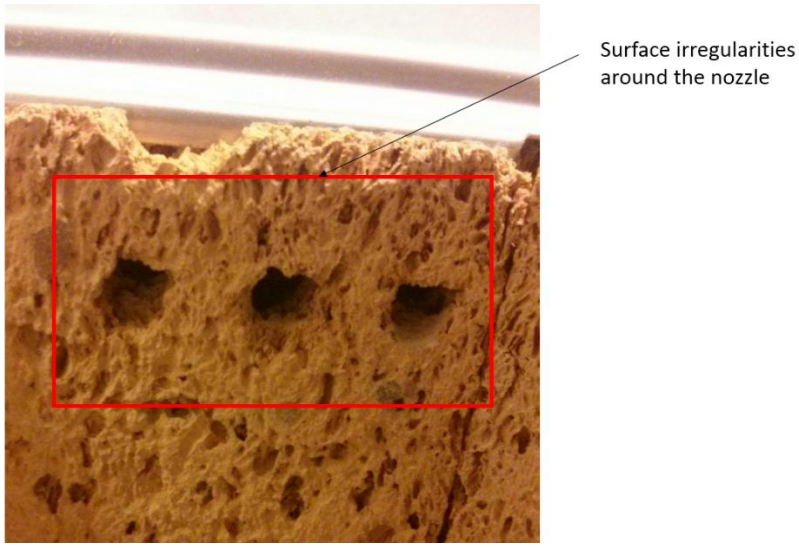

Figure 3.8: Irregular surface of the ceramic tile

Another aspect to be considered is irregular surface around the nozzle exit. This is highlighted in figure 3.8. Roughness and irregularities in the surface can trigger a transition to turbulence. This makes the use of turbulence models necessary.

Returning to the inlet boundary condition specification, along with the flow conditions specifying the turbulence variables is necessary. For a channel flow, the turbulence length scale is calculated as 0.07L where 'L' is the width of the channel or the pipe radius. The turbulence length scale is a measure of the size of the unresolved eddies.

In this case, the air gap of 7 mm is the characteristic length and therefore, the calculated length scale is 4.9*10^{-4}m. A turbulence intensity of 5% is assumed. (COMSOL CFD user's guide, 2013)

The inlet conditions are tabulated in table 3.3.

Property	Value
Pressure (P)	30 Pa
Turbulence intensity	5%
Characteristic length (L)	7 mm
Turbulence length scale	4.9 *10^{-4} m

Table 3.3: Inlet1 Boundary conditions

3.6.2. INLET 2

The mass flow of producer gases rising from the fuel bed is specified at this inlet. The producer gas is the product of the sub-stoichiometric combustion of the products of volatisation at the top of the fuel bed.

Table 3.4 shows the typical products of pyrolysis formed per kg of wood for different temperatures.

Temperature(K)	Char(kg)	Dry gas(kg)	Tar(kg)	Water(kg)
988	0.092	0.662	0.06	0.186
1088	0.057	0.758	0.06	0.125
1188	0.051	0.765	0.06	0.124

Table 3.4: Pyrolysis products (Mathieu and Dubuisson, 2012)

Considering only the dry gases and water, the mass flow of volatiles per Kg of wood

$$w_{volatiles} = w_{drygases} + w_{water}$$

The temperature of the char at the top of the fuel bed of the gasifier stove in the flaming mode of operation is close to 1200 K. (Varunkumar, 2012). For 1188 K, from table 3.4 substituting the values, we obtain

$$w_{volatiles} = 0.889\ kg\ /\ kg\ of\ wood$$

To calculate the total volatiles released from the top of the fuel bed, the wood burning rate in the stove needs to be established. This is done in the following paragraphs.

The firepower of the stove ranges from 4-5 kW. The calorific value of biomass is around 16 MJ/Kg. (Varunkumar, 2012). Considering an average fire power of 4.5 kW, the wood consumption rate can then be calculated as:

$$w_{wood} = \left(\frac{Firepower}{Calorific\ value\ of\ wood}\right) = \left(\frac{4500}{16 * 10^6}\right) = 16.87\ \text{g/min}$$

Therefore, the total mass of volatiles released

$$W_{volatiles} = w_{volatiles} * w_{wood}$$

$$W_{volatiles} = 2.5 * 10^{-4}\ kg/s$$

This is for the entire stove. For the segment modelled, the mass of volatiles released will be one ninth of this value. That is

$$W_{volatiles} = \left(\frac{1}{9}\right) * 2.5 * 10^{-4} = 2.77 * 10^{-5} kg/s$$

The volatiles released undergo sub stoichiometric combustion with the primary air forming the producer gas. The contribution of the primary air to the mass flow at the top of the fuel bed also needs to be considered. The primary air flow rate is calculated in section 3.6.1 as $6.251*10^{-5}$ kg/s.

Therefore the total flow rate of gases at the top of the fuel bed,

$$W_f = 9.028 * 10^{-5}\ kg/s$$

Along with the mass flow, the temperature of the gas also needs to be specified. The temperature of the gases has been obtained in different ways in the past. Bussman and Prasad, 1983 used an analytical expression to express the gas temperature as a function of distance from the fuel bed. Bussman, Visser

and Prasad, 1983 used an energy balance on the top of the fuel bed to obtain the gas temperature. Both these approaches were based on extensive experimental data relevant to only natural draft stoves.

Experimental data for the producer gases generated at the top of the fuel bed is available for a forced draft gasifier stove in Varunkumar, 2012. Oorja, the stove used in the cited literature operates in similar superficial velocity range as the Philips woodstove. Therefore the properties of the producer gas formed for both the stoves are comparable. For a wood consumption rate of 16 g/min, Varunkumar, 2012 reported the hot gas temperature exiting the fuel bed to be around 1200 K. This value is used for the simulation.

3.6.3. HEAT SOURCE

Combustion is modelled using a source term with uniform heat generation. The source term is defined for the entire combustion chamber as seen figure 3.7. The magnitude of the power to be specified is obtained from the specified fire power of the Philips stove, which is 4.5 kW.
About 70% of this energy is released in the flaming mode (Varunkumar, 2012). Therefore power output during the flaming mode is

$$P_{flaming} = 0.70 * 4.5 = 3.15\ kW$$

Considering the contribution of the enthalpy of the producer gas rising from the fuel bed, the total power output for the domain is expressed as

$$P_{flaming} = P_{source} + P_{enthalpy}$$

Where,
P_{source} - for energy released due to combustion
$P_{enthalpy}$ - energy content in the hot producer gases.

The energy content in the producer gases is calculated as the product of the mass flow rate and the enthalpy. Therefore

$$P_{enthalpy} = W_f * H_f$$

W_f is the producer gas mass flow which has already been established in section 3.6.2. H_f is the enthalpy of the producer gas. Its value determined from COMSOL is found to be around H_f = 1000 kJ/Kg.
Therefore the energy contribution of the hot producer gases is:

$$P_{enthalpy} = 7.82 * 10^{-4} * 1000 * 10^3$$
$$P_{enthalpy} = 782\ W$$

Therefore,

$$P_{source} = P_{flaming} - P_{enthalpy}$$

On substitution and calculation:

$$P_{source} = 3.15 - 0.782 = 2.37\ kW$$

This is the magnitude of the power source to be specified in the combustion chamber. Using this value resulted in extremely high temperatures in the combustion chamber. Temperature values are found to be in an acceptable range when the power magnitude is less than 900W. Therefore, as a limiting case a power source of 900W is used. (900W for the entire stove, 100W for the domain)

This is roughly 38% of the actual energy release (2.37kW) in the stove. One of the reasons for this is the discrepancy in secondary airflow entering the combustion chamber. With a pressure of 30Pa specified at inlet 1, the secondary air flow in the model is only 43% of the actual value. Therefore there is lesser energy being carried away by the exiting gases leading to higher temperatures in the domain. Establishing the right airflow is expected to allow for a source term with higher power output.

3.6.4. PERIODIC BOUNDARY CONDITION

Since only a segment of the stove is modelled a periodic boundary condition is necessary to account for the influence of neighboring domains. Periodic boundary conditions are used when the flow pattern and the thermal solution are repeating in nature. A periodic boundary condition for flow is specified at the edge of the domain.

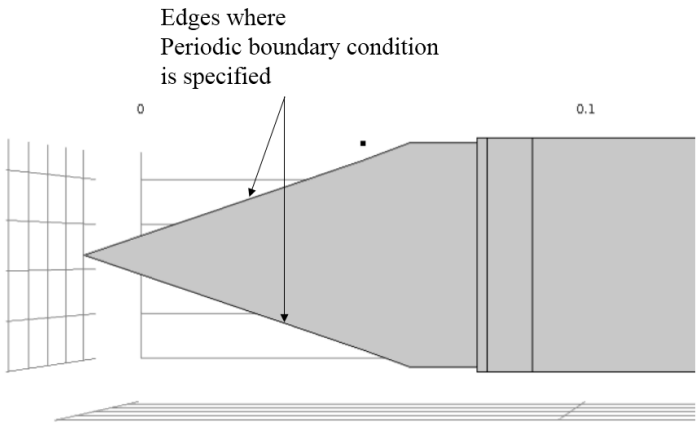

Figure 3.9: Periodic boundary condition

Only the edges inside the combustion chamber are specified. This is done to reduce the computational effort.

3.6.5. ISOTHERMAL VESSEL SURFACE

This is the temperature of the cooking vessel placed on the top of the stove. Previous experimental studies on wood stoves like Buissman and Prasad, 1983 and Zube, 2010 report the temperature of the pan to be around 373K. This value is used for the simulation.

3.6.6. SURFACE TO SURFACE RADIATION

This boundary condition is applied to all solid surfaces to account for the radiation between the surfaces. The surfaces included are the ceramic tile surfaces, the vessel surface, the insulating sheets and the seal. The equations used have been described in the earlier sections.

3.6.7. SURFACE TO AMBIENT RADIATION

The outer surface of the insulating chamber is exposed to the ambient. A surface to ambient radiation boundary condition is used to account for the radiation from the outer metal walls into the ambient. The outer surface of the insulating chamber is made of stainless steel. The emissivity values for stainless steel ranges from 0.6 to 0.85 (Engineering Tool Box). An emissivity of 0.8 is specified.

The radiation is modelled according to the following equations:

$$-n.\,(k\nabla T) = \epsilon_r \sigma\,(T_{amb}{}^4 - T^4)$$

Where ϵ_r is the emissivity of the material and σ is the Stefan Boltzmann's constant. Ambient temperature of 293 K is specified.
Radiation losses to the ambient environment assume negligible irradiation from the surroundings.

3.7. MESH

An unstructured mesh composed mostly of tetrahedral elements is used for in the simulations. A grid independence test is carried out to ascertain the level of refinement required. The results of the grid independence test is given in table 3.5.

Mesh	Degrees of freedom	Solution time(minutes)
Coarse	596217	101
Normal	970275	233
Fine	1616824	996

Table 3.5: Mesh details

The variation of jet velocity and temperature along the jet trajectory is studied for the three different mesh sizes. Figures 3.10 and 3.11 show the results obtained. The values are measured along the centerline of the second nozzle from the nozzle inlet to the center of the combustion chamber.

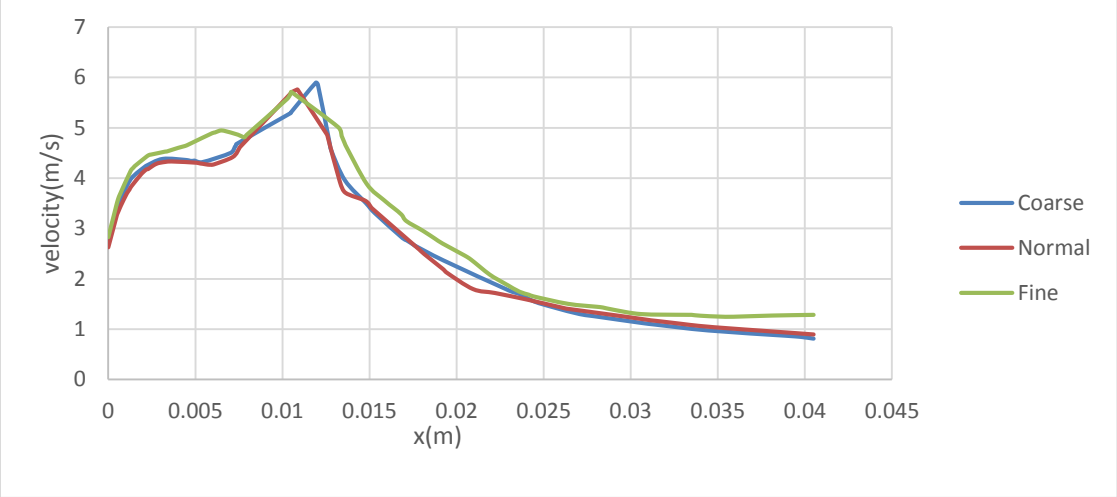

Figure 3.10: Mesh refinement study- velocity variation

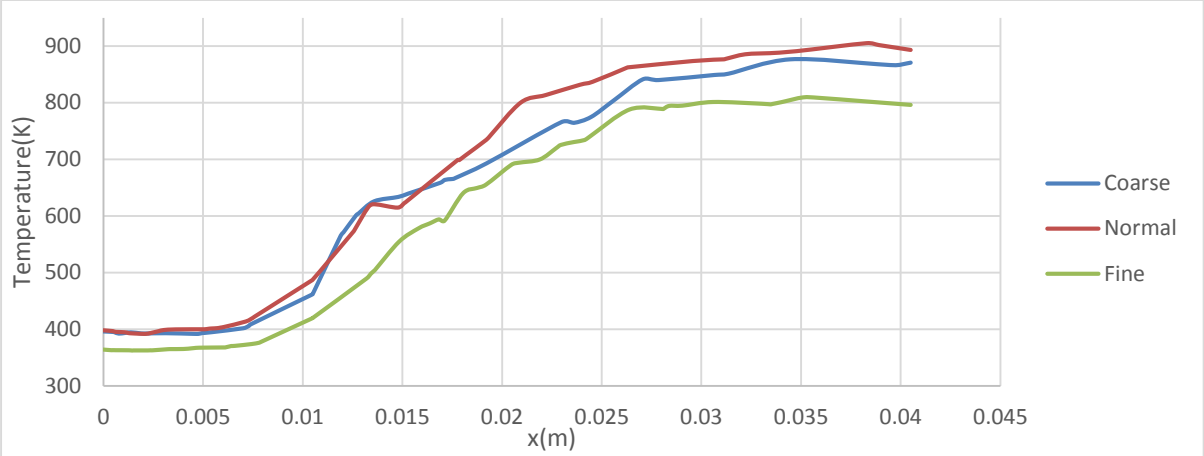

Figure 3.11: Grid independence study- temperature variation

Reducing the mesh size further beyond the fine resolution did not produce any significant variation in either the velocity or temperature. Therefore the fine mesh is chosen for the analysis. Figure 3.12 shows the generated mesh.

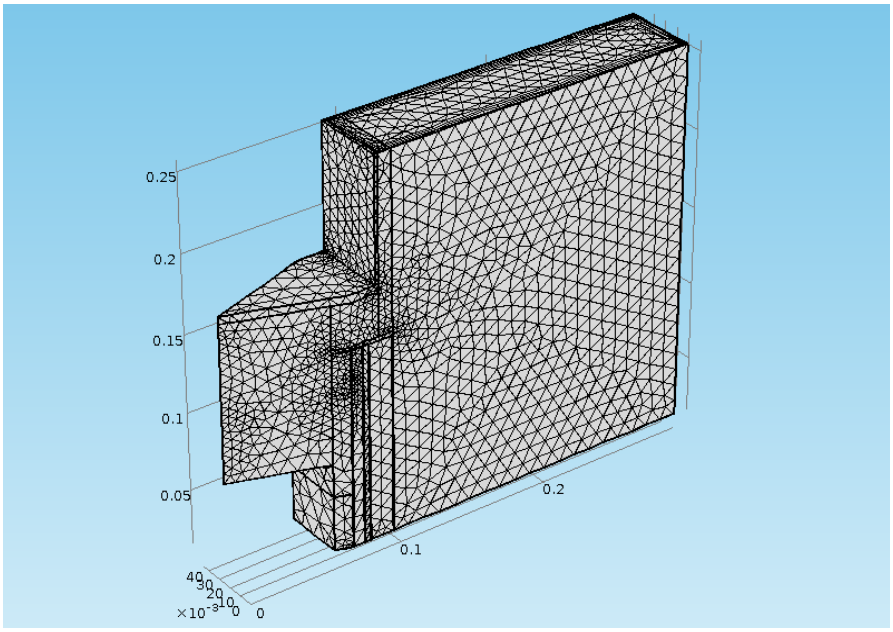

Figure 3.12. Generated mesh

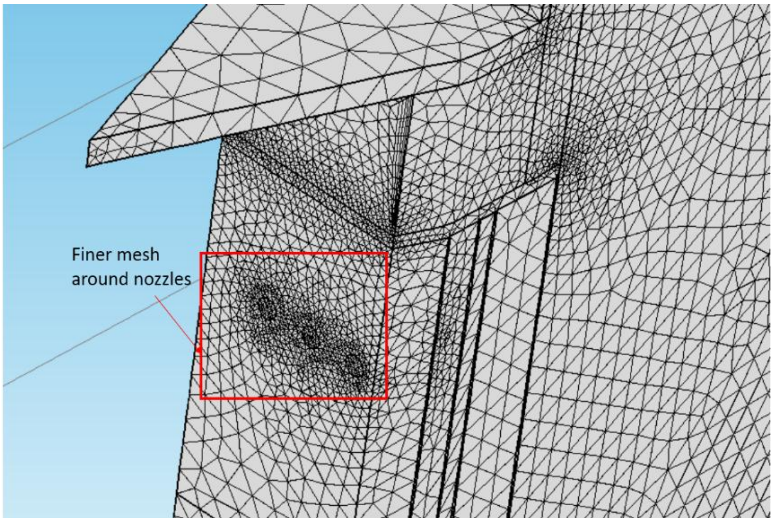

Figure 3.13. Finer mesh around nozzles

In regions where there are high gradients in flow properties, for example around the nozzles, the mesh is finer. This is highlighted in figure 3.13.
Table 3.6 shows some details of the mesh used.

Minimum element quality	1.376E-5
Average element quality	0.5179
Number of tetrahedral elements	362250
Total number of elements	536611

Table 3.6: Mesh statistics

3.8. DISCRETIZATION

COMSOL offers the choice of first and second order discretization in space. Simulations were run using both these discretization schemes. The results have been tabulated in table 3.7.

Discretization	First order in space **(P1 elements for both velocity and temperature)**	Second order in space **(Velocity-P2 elements Temperature –P1 elements)**
Number of degrees of freedom	181,892	970,275
Solution time	31 minutes	233 minutes

Table 3.7: Discretization order and solution time

The simulations were run for a normal mesh. As seen from table 3.7, the number of degrees of freedom and the solution time increase by a factor of 9 when second order discretization is implemented. The velocity contour plot for the two cases is shown in figure 3.14. The plot is along the center plane of the second nozzle for both the cases

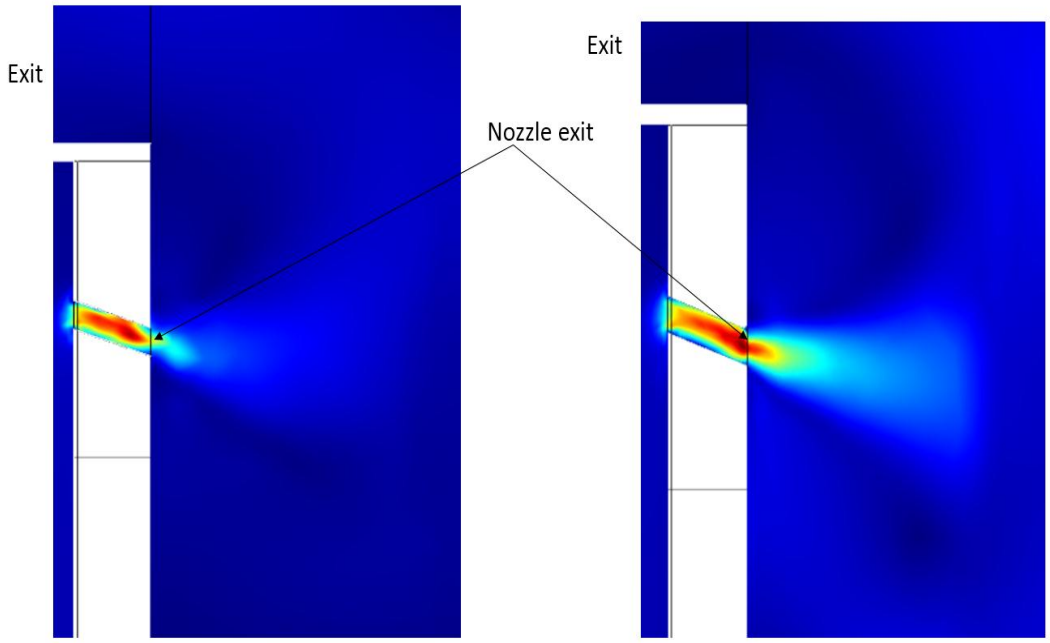

Figure 3.14: Velocity contours, Left) First order discretization Right) Second order discretization

The figure reveals that the flow field is better resolved in case of the second order discretization. A comparison of the velocity magnitude for both the cases is shown in figure 3.15. The measurements is along the centerline of the second nozzle starting from the nozzle inlet to the center of the combustion chamber.

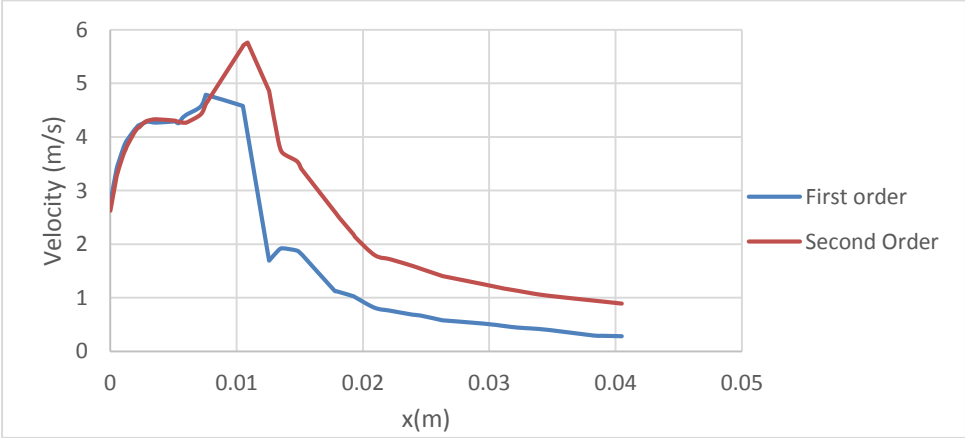

Figure 3.15: Velocity comparison – first and second order discretization

The figure reveals a substantial difference in the magnitude of velocity between the two cases. The order of discretization thus significantly influences the results. Since a second order discretization scheme returns a better resolved flow field, it is incorporated in the model.

3.9. SOLVER SETTINGS

A direct solver is used for the simulations. Convergence was faster with a direct solver compared to an iterative solver. The tolerance of the solver is 10^{-3}.
Additional details on some of the fundamental aspects involved in COMSOL Multiphysics software is explained in Appendix E.

The simulation is run with the geometry described incorporating a fine mesh with a second order discretization scheme. The results obtained are discussed in the next section.

Chapter 4. Results

In this chapter, the results obtained from the simulation model are discussed. The chapter is divided into two sections. The first sections analyzes the temperature and the flow patterns. In the second section, the mixing behavior of the air and the producer gases is discussed.

4.1. FLOW PATTERNS AND TEMPERATURE DISTRIBUTION

In this section, the fluid flow patterns and the temperature fields in the different regions of the stove are analyzed. The analysis is carried out in the following regions of the stove:

1) Annular chamber
2) Nozzles
3) Combustion chamber
4) Insulation sheets

The different regions are highlighted in figure 4.1.

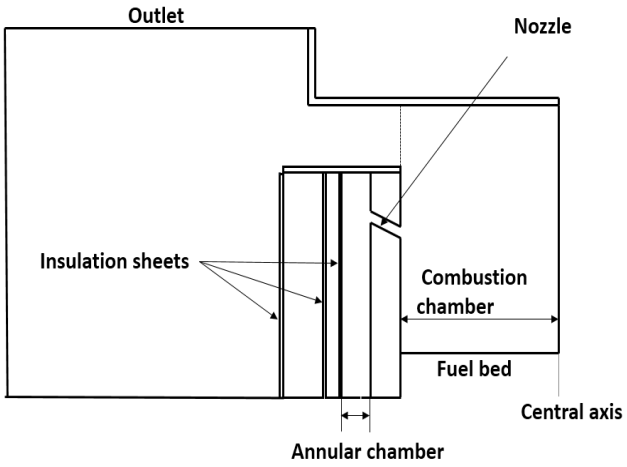

Figure 4.1: Gasifier stove -components

We begin with a discussion on the annular chamber.

4.1.1. ANNULAR CHAMBER

The annular chamber is a passage for the air from the fan to the nozzles. It is a circular chamber enclosed by the insulation tile support on one side and the innermost insulating sheet on the other (refer to figure

4.1). The annular chamber is provided to preheat the combustion air. The temperature variation of air and the walls of the annular chamber along the height of the annular chamber are shown in figure 4.2.

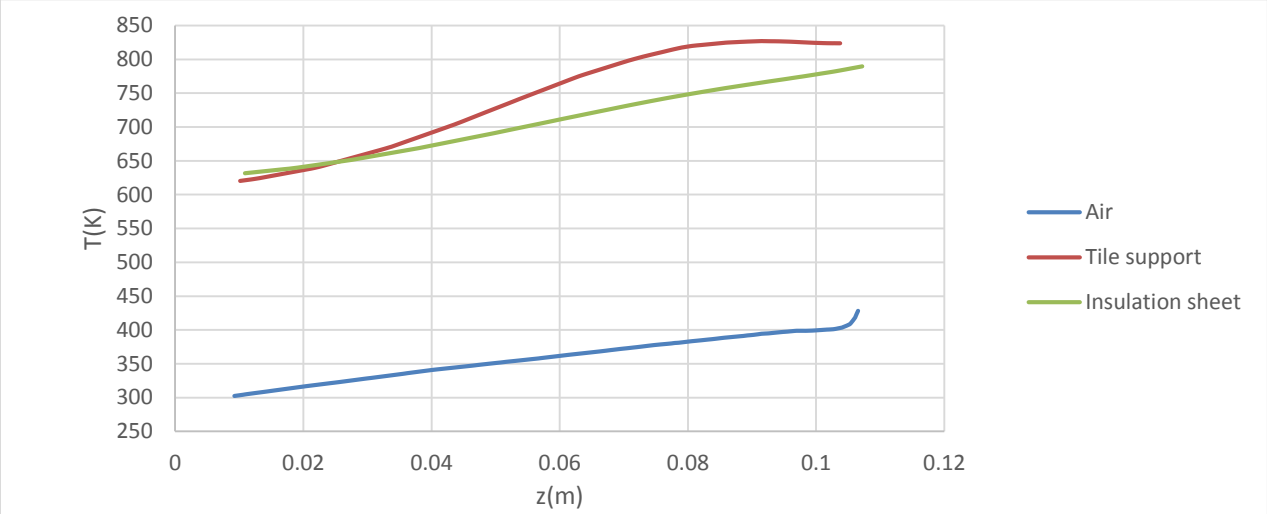

Figure 4.2: Temperature variation, annular chamber (along nozzle 2 center plane)

The measurement is along the center-plane of the second nozzle. The value of 'z' is from where the air enters the chamber to the nozzle center point.

The walls of the annular chamber are at high temperatures because of the proximity to the combustion chamber. The preheating in the annular chamber is of the order of 100K. The average temperature of air at the nozzle inlet is 440K. Similar behavior is seen for the case of the first and the third nozzles.

The heated air upon entering the nozzle, transforms into a jet. The flow behavior in the nozzles is explained in the following section.

4.1.2. NOZZLES

The air flow from the annular chamber gets divided among the three nozzles almost equally. The mass flow measured at the inlet of each nozzle is provided in table 4.1.

The mass flow is calculated as the surface integral of the momentum over the inlet surfaces of the nozzle

$$w_{noz} = \int (\rho * U)\, ds$$

Nozzle	Mass Flow (Kg/s)
1	$3.89*10^{-5}$
2	$3.86*10^{-5}$
3	$3.71*10^{-5}$

Table 4.1: Mass flow in the nozzles

Because of the small nozzle area (d=4mm), the fluid entering the nozzles is transformed into a jet with a high velocity core. The velocity contour of the flow in the nozzle 2 is shown in figure 4.3.

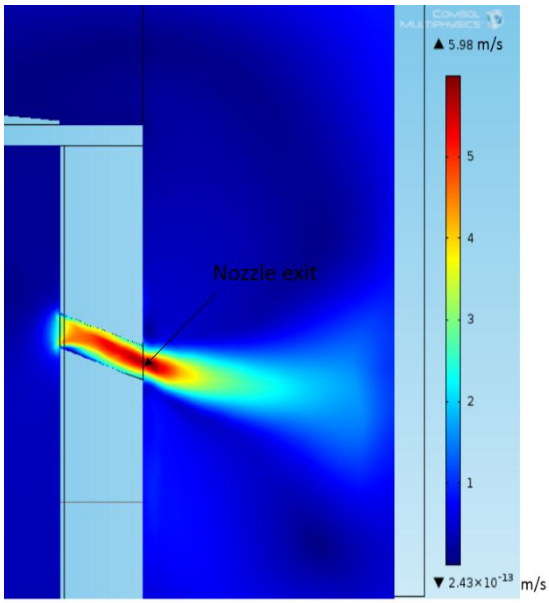

Figure 4.3: Velocity magnitude (along the center plane of 2nd nozzle)

From the velocity magnitude, the Reynolds number of the jet can be calculated as

$$Re = \frac{\mu d U_j}{\rho}$$

Where,
μ - Dynamic viscosity, Pa-s
d- diameter of the nozzle, m
U_j – velocity of the jet, m/s
ρ – Density, Kg/m^3
The Reynolds number calculated along the centerline of the three nozzles is shown in figure 4.4.

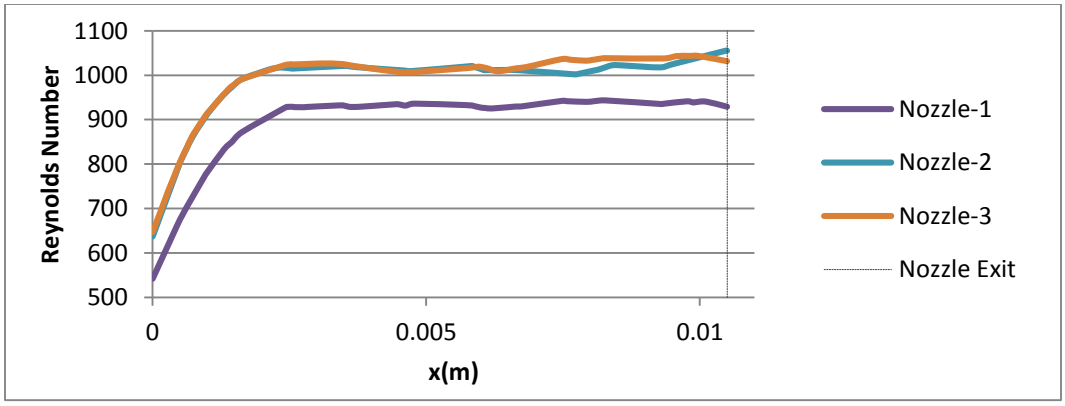

Figure 4.4: Reynold's number variation along nozzle center plane

The plot is along the centerline of the nozzles from the inlet to the exit into the combustion chamber. The Reynolds number along the entire nozzle is lower than the critical value of 2300 for flow in circular channels (Cengel and Cimbala, 2010). The flow in the nozzles remains laminar. However at the exit, the

Reynolds number ranges from 925-1025. A jet exiting at this Reynolds number make a transition to turbulence.

The walls of the nozzle are at very high temperatures due to their proximity to the combustion chamber. Consequently, the air stream heats up rapidly as it travels the length of the nozzle. The temperature variation of air measured along the nozzle centerline is shown in figure 4.5. The dotted line indicates the nozzle exit.

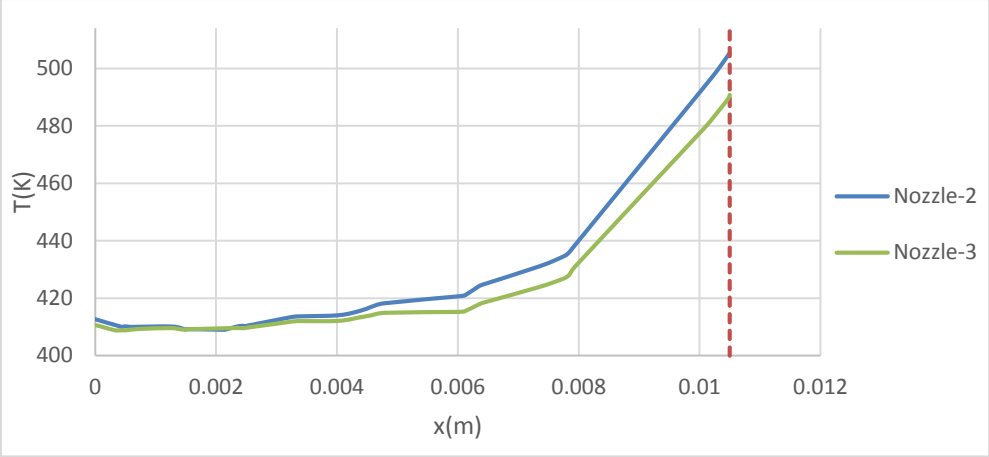

Figure 4.5: Air temperature along the nozzle centerline

As can be seen from figure 4.5, the preheating of air is significant, with a temperature increase of around 80-90 K over a distance of 10.5 mm (ceramic tile thickness-10mm, tile support- 5mm).

The temperature of the air flow closer to the walls is much higher than the temperature of air close to the centerline. The average air temperature exiting the nozzle (and entering the combustion chamber) is higher than the centerline values. The average temperature at the nozzle exit for the three nozzles is shown in table 4.2.

Nozzle	Temperature (K)
1	595
2	591
3	581

Table 4.2 : Average temperature at nozzle exit

Preheating of the secondary air is one of the basic principles of stove design. A higher air inlet temperature reduces emissions and accelerates the combustion reactions (Baldwin, 1987).Higher secondary air temperature is crucial in achieving tier 4 emission levels. De Foort (2015) has reported tier 4 emission levels in a forced draft gasifier stove with secondary air temperatures of 573 K.

Thus air at the nozzle exit has an average temperature of around 590K and a Reynolds number of approximately 1000. The behavior of the jet as it expands into the combustion chamber is explained in the following sections.

4.1.3. COMBUSTION CHAMBER

The heated air jets from the nozzle exit into the combustion chamber. 27 jets exit into the combustion chamber and collide at the center of the combustion chamber. The jet streams heat up rapidly because of the high temperatures in the combustion chamber. Interaction of the air jets with the fuel stream and the collision with other jets sets up a complex flow regime. This can be seen in the path lines of the fluid flow is seen in figure 4.6.

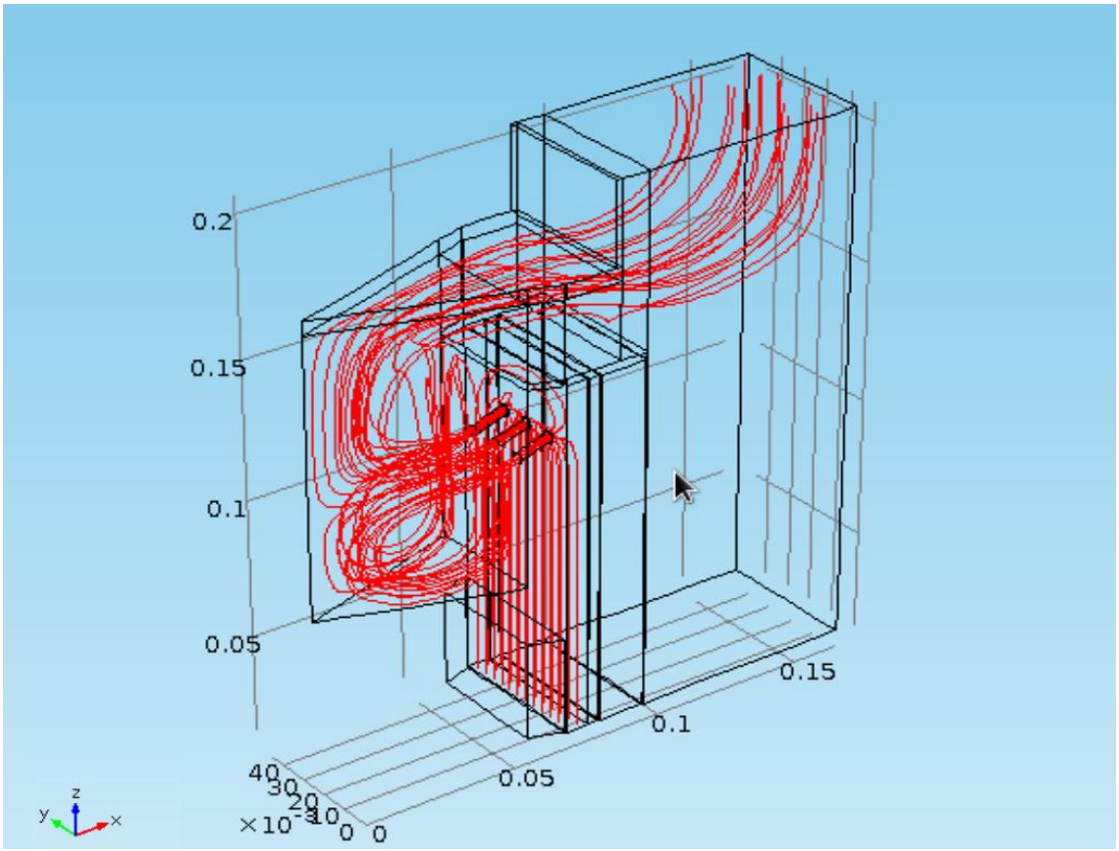

Figure 4.6: Flow path lines

The jet expands as it penetrates into the combustion chamber. Close to the center of the chamber it bifurcates into an upper and lower stream. The lower stream sets up a region of recirculation, while the upper stream escapes through the exit. The recirculation zone is due to the collision of jets from the neighboring domains. There is also a wake region just above the nozzles where there is ambient air entrainment.

The flow pattern along the center plane of the second nozzle is shown in Figure 4.7. It can be seen that the high momentum jet suppresses the rising fuel stream setting up a clockwise circulation in the lower regions close to the fuel bed. The flow pattern has a kidney like structure with a high velocity jet core surrounded by counter rotating circulation zones on both sides.

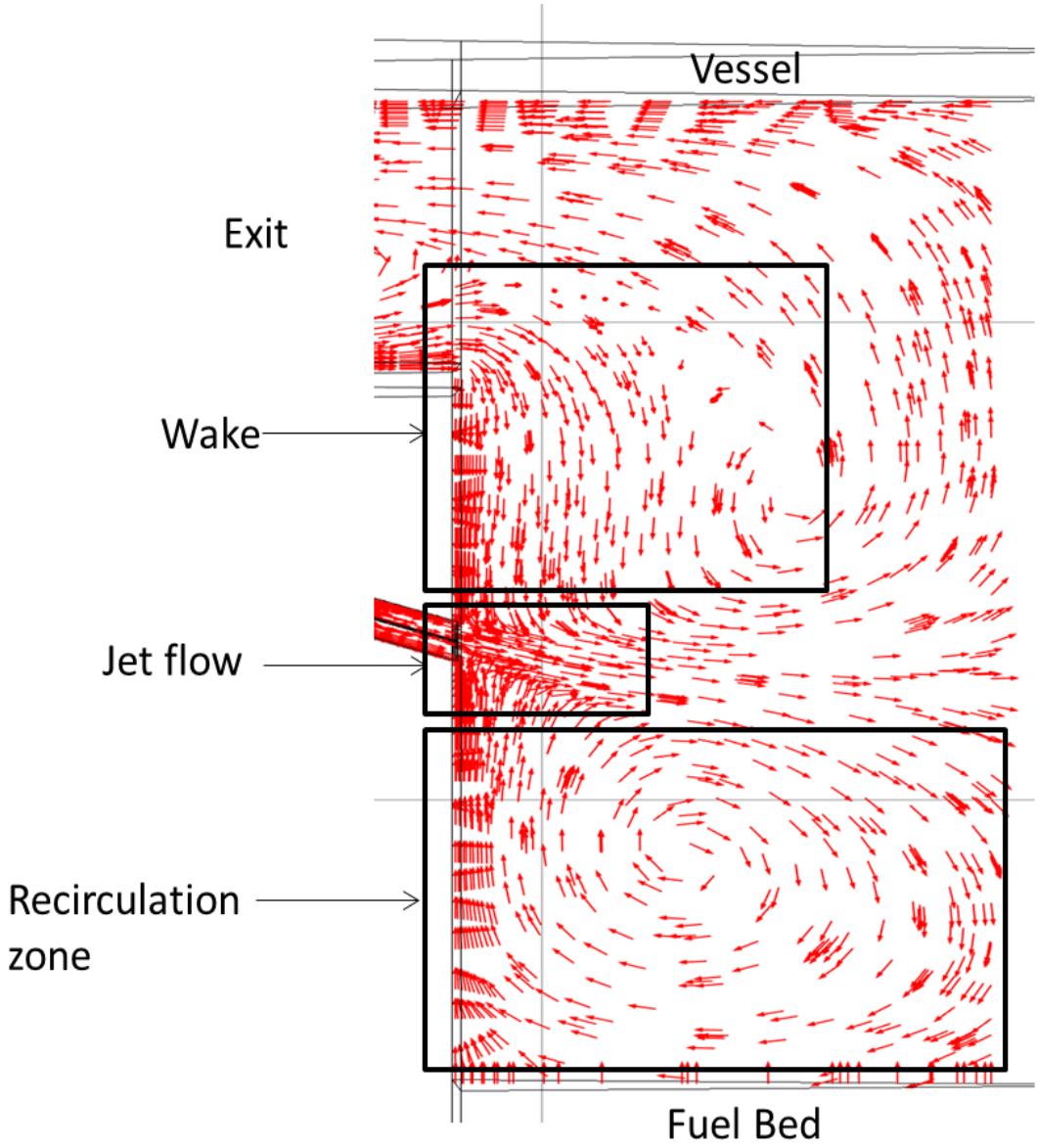

Figure 4.7: Different flow regions inside the combustion chamber

The nozzle arrangement in the insulation tile is not symmetric along the centerline of the tile. Consequently, in a region away from the nozzles the flow pattern is slightly different from what is observed along the nozzle center plane. The 'arrow plot' plotted along a plane away from the nozzles is shown in figure 4.8.In the region away from the nozzles, the kidney shaped pattern is less pronounced. In the absence of the air jet, the fuel rich stream rising up along the walls of the combustion chamber flow into the wake region above the nozzles. There is no ambient air entrainment along this plane.

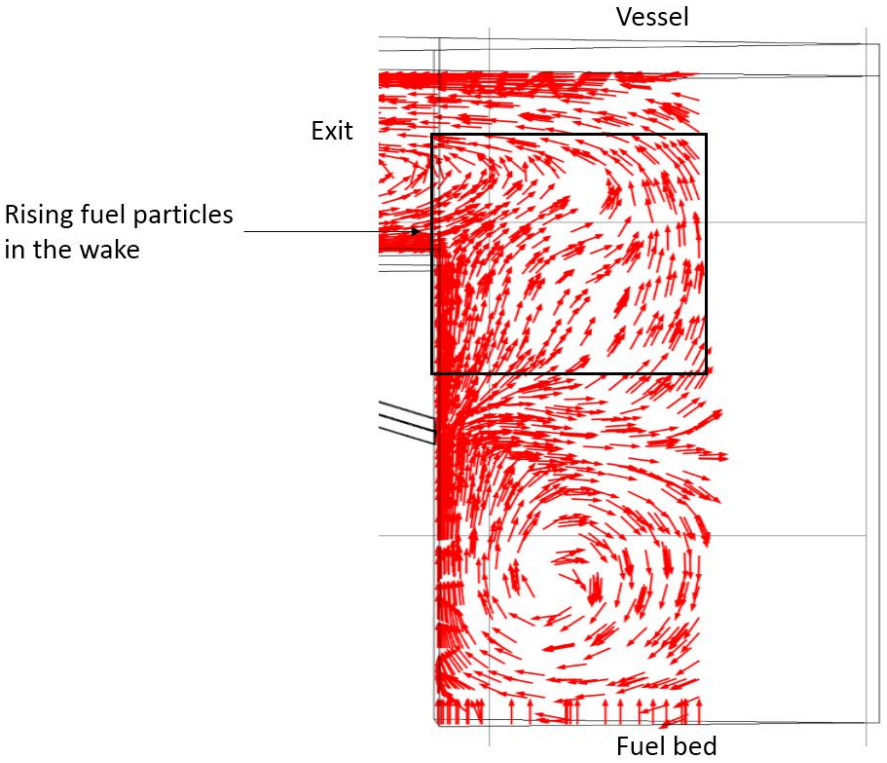

Figure 4.8 Arrow volume - in between nozzles, y=0.02315m

It is evident from figures 4.7 and 4.8 that there are three important regions of flow inside the combustion chamber. They are:
1) Jet flow region
2) Recirculation zone
3) Wake region

Each of this region is discussed in the following section.

4.1.3.1. JET FLOW REGION

This is the region very close to the nozzle exit where the flow exhibits jet behavior. This is evident from the contour plot shown in in figure 4.9.The contour plot reveals a high velocity core flow surrounded by relatively lower velocity layers on the edges. The outer edges of the flow come in contact with the surrounding fluid forming a shear layer. This is more pronounced in the lower edges of the jet because of the interaction with the fuel crossflow. The shear layer is crucial to mixing and its significance is explained in the later sections.

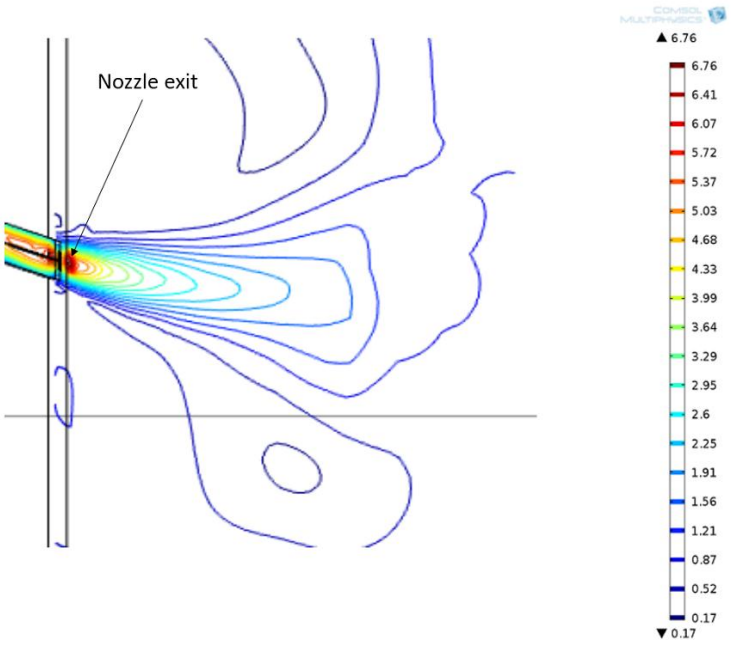

Figure 4.9: Velocity contour - Nozzle exit

The rapid deceleration of the jet can also be observed from figure 4.9.

The jet at the exit can be treated as a momentum source. Along the jet trajectory the jet decays as it loses momentum and spreads as it entrains the surrounding fluid. The spatial evolution or the spreading of the jet as it expands into the combustion chamber is shown in figure 4.10.

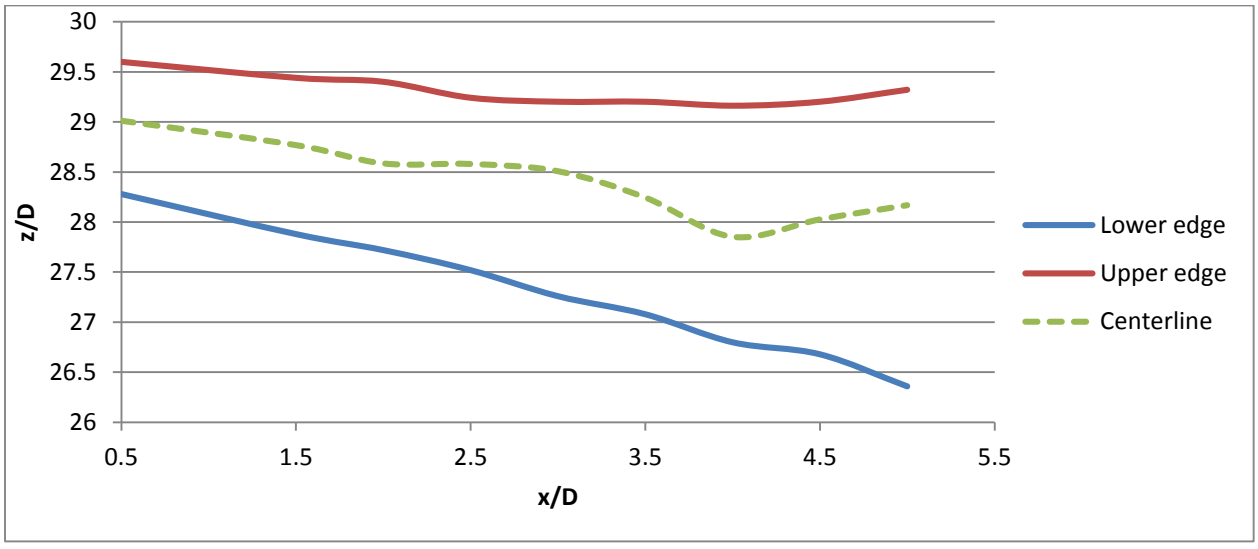

Figure 4.10: Evolution of the jet (z plane, along the nozzle 2 central axis)

The X axis is plotted along the radius of the combustion chamber. The distances measured are from the nozzle exit.

The centerline of the jet is formed by the locus of maximum momentum points while the width is chosen as the distance where the momentum is at least 10% of the momentum at the nozzle exit.
It is observed that the jet flow region is restricted to distances less than x=5D. Beyond this distance the jet bifurcates into a lower and an upper stream. The spreading angle of the jet is calculated from figure 4.10 is approximately 27° which is slightly larger than the spreading angle for a free jet.

As the jet spreads, it rapidly decelerates. This evident from figure 4.11 which shows the centerline velocity of the jet plotted along the jet trajectory. The jet velocity is normalized with the velocity at the nozzle exit while the axial distance is normalized with the diameter of the jet. The plot extends from the nozzle exit up till a distance of about 20mm into the combustion chamber, beyond which jet behavior ceases to exist.

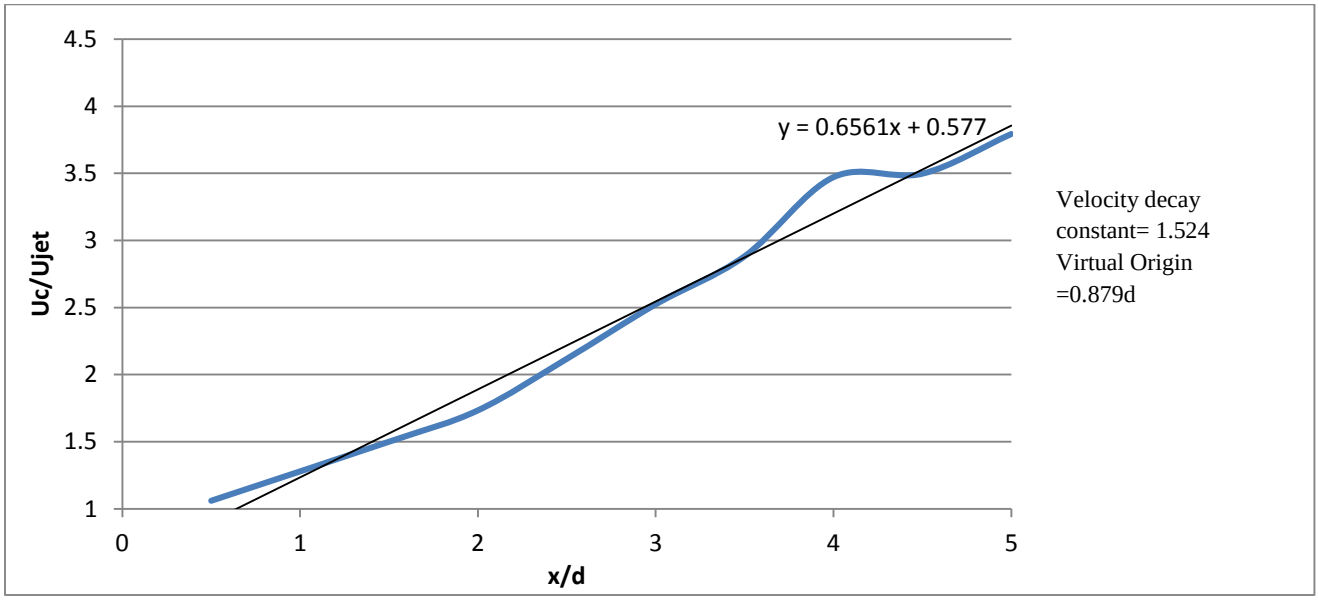

Figure 4.11: Centerline velocity decay

A decay constant calculated as the slope of the normalized velocity curve and a virtual origin calculated as the intercept made by the curve on the X- axis are good indicators of the velocity decay. (Pope, 2000)

From figure 4.11, the decay constant is calculated as 1.524 and the virtual origin is located at x_o=1.733. At x=5d, the velocity is only about quarter the velocity at the nozzle exit.

The rapid velocity decay translates into a rapid decline of Reynolds number of the jet. Figure 4.12 shows the Reynolds number variation for the jet, calculated on the basis of the jet width, plotted for different distances downstream of the nozzle.

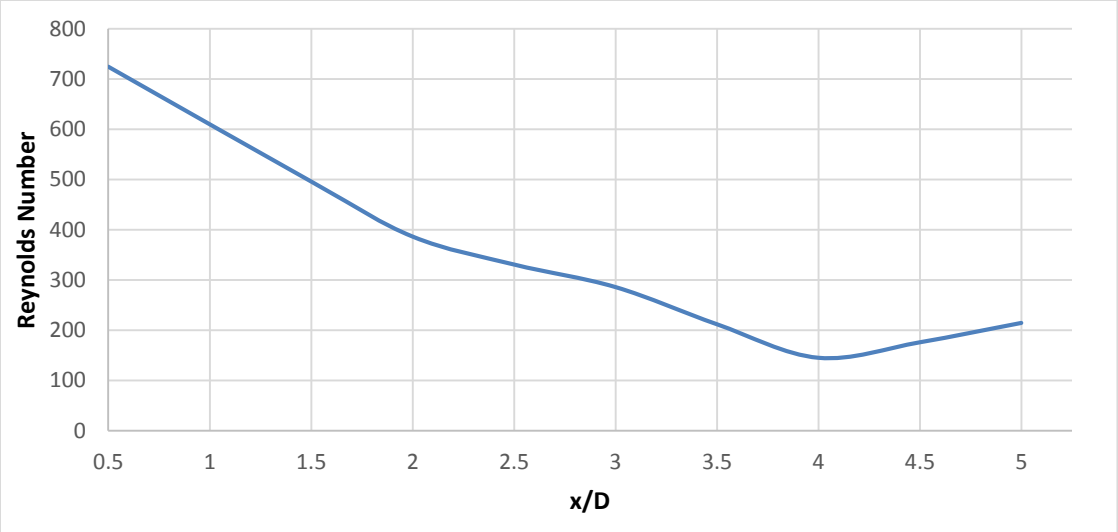

Figure 4.12: Reynolds Number variation

Appendix B contains a tabulation of the jet width and the corresponding Reynolds number at different downstream distances.

There are fewer forces deflecting acting on the jet in the lateral direction and the jet maintains a trajectory close to the nozzle centerline. The spreading angle is calculated to be around 28 °. The spreading is axisymmetric along the centerline. The jet flow along the lateral direction is restricted to a very small distance of x=2.5D and beyond this distance it collides with air streams from the neighboring nozzles.

Therefore the jet region in the combustion chamber is restricted to a very small region of x<5D from the nozzle exit. This is a region of rapid velocity decline and temperature rise. The lower edge of the jet sets up a region of recirculation in lower regions close to the fuel bed. This region is analyzed in the following section.

4.1.3.2. RECIRCULATION ZONE

The recirculation zone is set up because of the collision of the air jets from the neighboring domains at the center of the combustion chamber. The recirculation zone ensures good mixing between the air and the fuel streams. This forms the lower half of the kidney like structure explained in section 4.1.3. The vertical

velocity profiles plotted for different heights (z) along the length(x) of the combustion chamber is shown in figure 4.13. The co-ordinate system used is provided in figure 4.14.

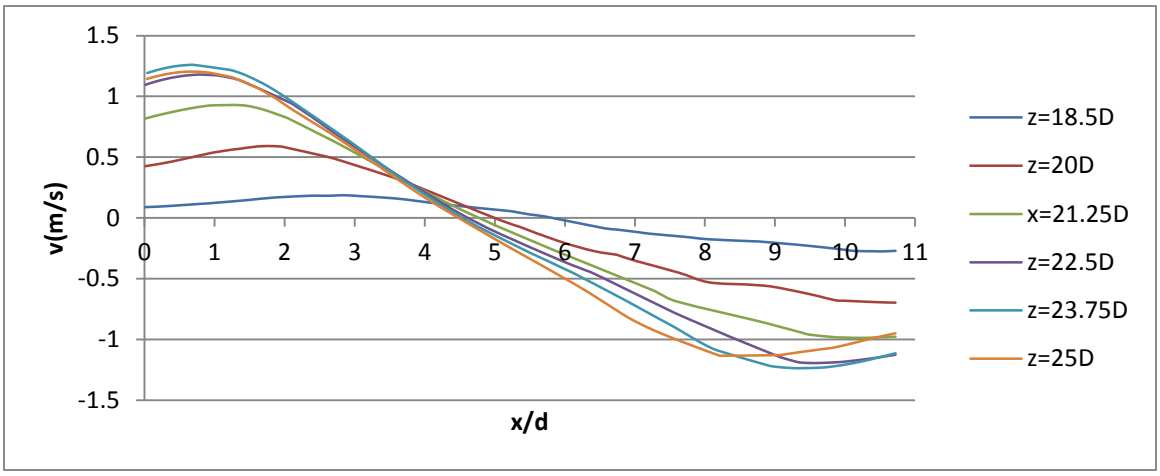

Figure 4.13: Velocity profiles-Recirculation zone

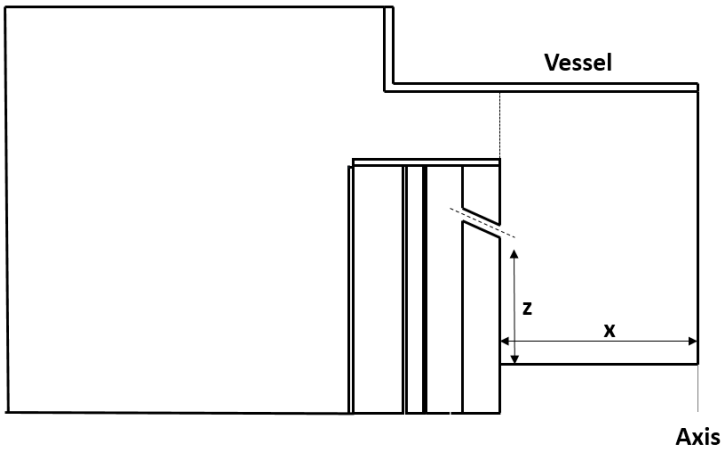

Figure 4.14: Coordinate system used

The vertical velocity component changes sign at the stagnation point around which the clockwise circulation is centered. The high velocity in the region close to the walls points to a presence of a strong wall jet along the walls of the combustion chamber.

4.1.3.3. WAKE

As explained earlier the wake is formed in the regions directly above the nozzle. A small portion of the fuel stream rising from the fuel bed escapes through the spaces between the nozzles and accumulates in this region. The upper edge of the jet drives a weak circulation in the anti-clockwise direction. The wake is a regions of ambient air entrainment as explained earlier.

4.1.4. TEMPERATURE PROFILE

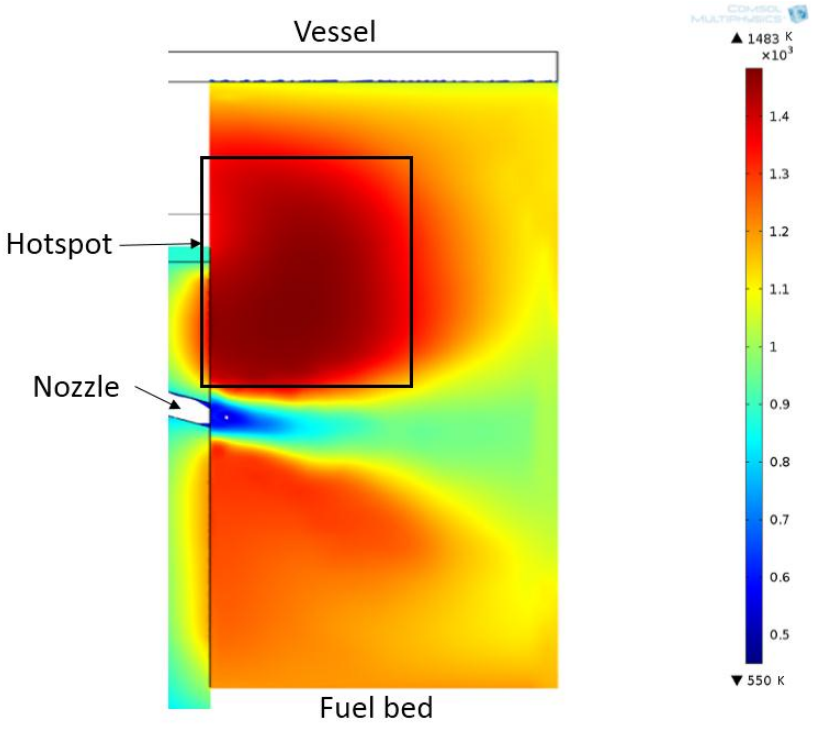

Figure 4.15: Temperature variation inside the combustion chamber (along the second nozzle plane)

The temperature field inside the combustion chamber is seen in figure 4.15.

There exists a hotspot in the combustion chamber where the temperature is the highest. This corresponds to the wake region where there is limited fluid flow. This is a consequence of the uniform heat generation assumption. The same phenomena is observed in the recirculation zone close to the stagnation point. This is in contrast to the actual operating conditions where the temperature is proportional to the flow rate of the air fuel mixture. Higher temperatures are expected towards the center of the flame and not in the proximity of the insulation tiles.
Therefore the temperature field is not a realistic approximation of the actual conditions.

VALIDATION

Experimental data on the flow field and the temperatures inside the combustion chamber is not available. However, visual observations of the stove operation indicate the presence of a recirculation zone in the lower regions of the combustion chamber. The flame observed during the actual stove operation is provided in figure 4.16.

Figure 4.16: Flame pattern in the stove

Since the flow field simulations inside the combustion chamber are in sync with the visual observations the model is qualitatively validated. It can thus be used as a tool for visualizing the flow patterns in the combustion chamber.

Next, we analyze the temperature distribution in the insulating structures of the stove.

4.1.5. INSULATION SHEETS

Figure 4.17 shows the insulation sheets provided at different regions of the stove:

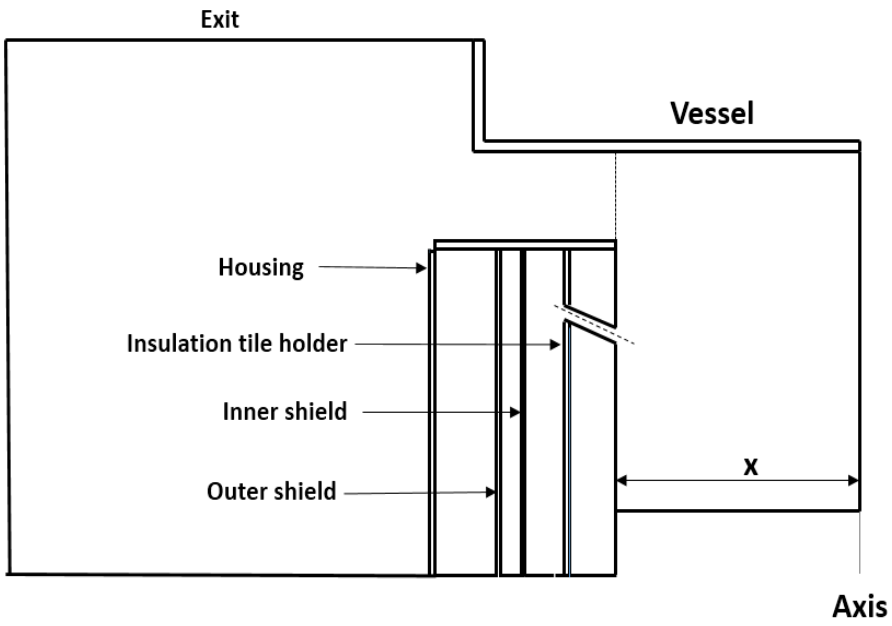

Figure 4.17: Insulation chamber – components

The temperature values in these parts are of interest. Experimental values for the temperature in these components for different fan speeds is available. Table 4.3 provides a comparison of the experimental and the simulation values.

	Experimental values		Simulation	
Region	**Top (K)**	**Bottom (K)**	**Top (K)**	**Bottom(K)**
Insulation tile holder	625-675	575-625	750	592
Inner shield	500-550	425	700	580
Outer shield	475-495	398	610	450
Housing	375-400	323	450	300

Table 4.3: Temperature values-insulation chamber

- There are significant differences between the simulation and experimental values. The values are comparable only at the bottom of the insulation tile holder and the housing.
- The values in the upper regions are substantially higher than experimental results. This due to the following reasons.
  1) Presence of a hot spot in the wake region very close to the insulation tiles.
  2) Non detailed design: Specific design details have not been included in the model partly to reduce the computation effort involved. For example consider the seal of the insulation chamber. In the actual stove the seal is inclined upwards towards the exit of the stove. This inclination forces the hot gases from the combustion chamber upwards away from the insulation sheets. This inclination has not been modelled. Consequently, the upper regions of the insulation chamber are exposed to the hot gases leading to higher temperatures.
- Non –inclusion of the design details is the cause for the large discrepancies seen in temperature values in the inner and the outer shield.
- Compared to the combustion chamber, the temperature values for the insulation chamber are slightly more realistic. A more detailed design will lead to more acceptable set of values.

To conclude, in this section the flow field and the temperature profile in the combustion region as predicted by the simulation was analyzed. While the flow field is in agreement with visual observations, the temperature distribution does not represent the actual stove operating conditions accurately. A better definition of the heat term is required to overcome this drawback. The temperature is the insulating structures are more reasonable, however they still show a large deviation from experimental values. Incorporating the detailed design is expected to return more agreeable results.

4.1.7. SIMULATIONS WITH HIGHER INLET PRESSURE

Refer to section 3.6.1 where it has been explained that the specified inlet pressure of 30 Pa at the annular chamber inlet results in a secondary air flow that is 45% of the experimental value. A few simulations with a higher inlet pressure of 50 Pa have been carried out and the results are presented in this section. A comprehensive analysis was not possible, only some important details are specified here.

- The mass flows in the three nozzles for both the cases has been reproduced in table 4.4. The mass flow with the higher pressure is roughly 72% of the experimental value.

Nozzle	Inlet pressure=50Pa	Inlet pressure =30 Pa
1	$4.9*10^{-5}$ kg/s	$3.89*10^{-5}$ kg/s
2	$5.1*10^{-5}$ kg/s	$3.86*10^{-5}$ kg/s
3	$5.08*10^{-5}$ kg/s	$3.71*10^{-5}$ kg/s
Total	$15.08*10^{-5}$ kg/s (56% of actual value)	$11.46*10^{-5}$ kg/s (43% of actual value)

Table 4.4: Temperature values-insulation chamber

- The increased secondary air flow leads to increased velocities in the nozzles. The air jet penetrates deeper into the combustion chamber. This is visible in 4.18a.

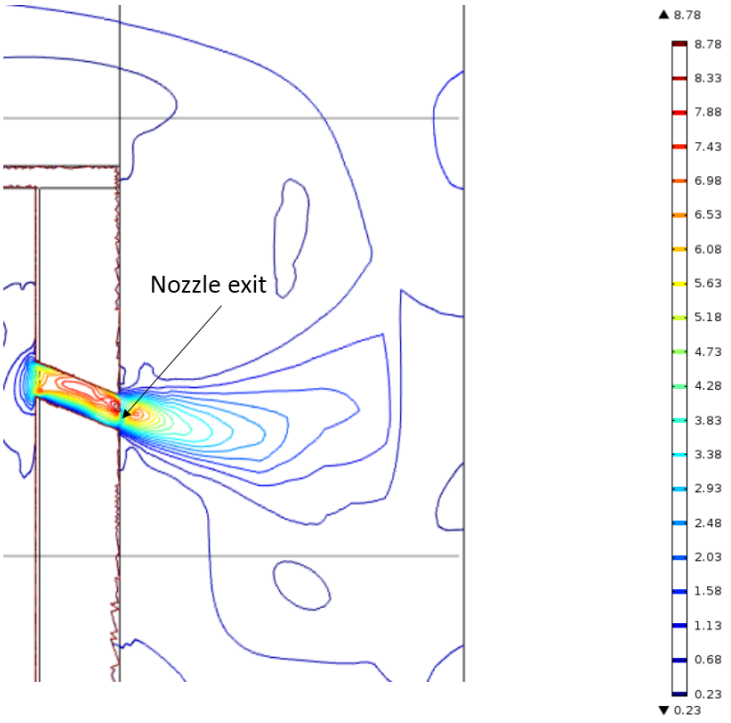

Figure 4.18a: Velocity contours (m/s), Inlet pressure=50Pa

- A comparison of the jet properties for both the cases is provided in table 4.5.

Nozzle	Inlet pressure=50Pa	Inlet pressure =30Pa
Virtual origin	0.685	0.879
Decay constant	1.04733	1.524

Table 4.5: Jet properties comparison

- The biggest influence of the increased mass flow is on the temperature field in the combustion chamber. Figure 4.18b shows the temperature distribution for the inlet pressure of 50 Pa. Compared to figure 4.15, the highest temperature is no longer in the wake region. Increased mass flow means, the wake formed is less pronounced eliminating the hotspot observed for the earlier case. Also the magnitude of maximum temperature is less by around 200K compared to the first case.

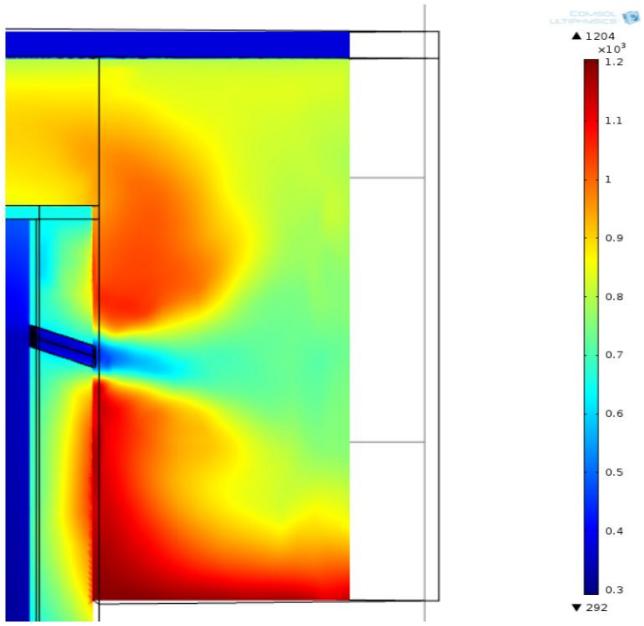

Figure 4.18b: Temperature field: Inlet pressure=50Pa

- The overall temperatures in the insulation structures are also lower by almost 200K in the insulation tile holder and the inner shield. A comparison is provided in table 4.6.

	Experimental values		Inlet =50Pa		Inlet =30Pa	
Region	**Top (K)**	**Bottom (K)**	**Top (K)**	**Bottom(K)**	**Top (K)**	**Bottom(K)**
Insulation tile holder	625-675	575-625	550	410	750	592
Inner shield	500-550	425	500	400	700	580

Table 4.6: Temperature values-insulation chamber

- The temperature values differ from the experimental values by around 75-100K. Therefore a source term with a higher power magnitude can be specified.

4.2: MIXING ANALYSIS

In this section the mixing of the air and the fuel stream in different regions of the stove is analyzed. Though the kinetics of combustion is not modelled, mixture fraction analysis will shed light on the probability of combustion at different regions. Passive scalars are implemented for this purpose.

The concentration of the reactants and the temperature are the two most important factors influencing the rate of a reaction. A prerequisite for analyzing the mixing behavior is to establish the desired concentration levels of the reactants and temperature values. This is done initially followed by the study of the scalar concentration profiles of the reactants.

The mixing analysis is done only for the case when the inlet air pressure is 30 Pa.

4.2.1. CONCENTRATION OF REACTANTS

The focus in this section is on establishing the desired range of reactant concentration for secondary combustion. The combustion equation needs to be formulated for this purpose. Knowledge of the producer gas composition is required for deriving the combustion equation.

The composition of the producer gas is a strong function of the 'superficial velocity' of a gasifier. Superficial velocity is a property that characterizes the operating range of a gasifier. It is defined as

$$U_s = \frac{Gas\ Production\ rate\left(\frac{m^3}{s}\right)}{Crosssectional\ area\ (m^2)}$$ (Reed et al, 97)

It is the most significant property influencing the fuel bed temperature and the exit gas composition for a fixed bed of biomass (Fatehi & Kaviany, 1994). For a domestic cooking stove, the value of superficial velocity is limited to 3.5 - 6 cm/s to restrict the particle carry over and reduce emissions (Reed et al, 97).

Experimental data for the producer gas composition is not available for the Philips wood stove. However, detailed experiments have been carried out on Oorja, a forced draft gasifier stove by Varunkumar, 2012. The Oorja stove operates in the same range of superficial velocities as the Philips stove. And because the composition is a strong function of the superficial velocity, the producer gas composition for the two stoves will be similar. Therefore, experimental data from Varunkumar, 2012 is used to formulate the combustion equation.

4.2.1.1. THE COMBUSTION EQUATION

The producer gas composition depends on the type of biomass used. Wooden chips are typically used in gasifier stoves. The ultimate analysis of such chips is given in table 4.7. The composition is calculated on a moisture and ash free basis.

Element	Weight (%)
C	44.4
H	6.3
O	48.8
N	0.6

Table 4.7: Ultimate analysis of wood chips used in stoves (Varunkumar, 2012)

In the flaming mode, biomass initially undergoes heating and devolatisation. The volatiles react with the primary air supplied at the bottom of the fuel bed, undergoing sub-stoichiometric combustion. The product gases formed has CO, CO_2, H_2, H_2O and CH_4 as its constituents. These gases pass through the hot char bed on the top of the fuel bed forming a producer gas rich in CO and H_2 (Varunkumar, 2012).

When wood with composition specified in table 4.7 is used, the composition of the producer gas formed is shown in table 4.8. 'Y' is the mass fraction and 'X' is the mole fraction.

Component	Y (%)	X (%)
CO	10.8	9.6
CO_2	23.5	13.3
CH_4	2.5	3.9
H	0.8	10.0
H_2O	15.6	21.6
O	0.8	0.6
N_2	46.0	41.0

Table 4.8: Producer gas composition (Varunkumar, 2012)

This producer gas formed is oxidized by the secondary air releasing heat in the process. Using the molar fractions given in table 4.8, this reaction can be expressed as:

$$9.6CO + 3.9CH_4 + 10H_2 + 0.6O_2 + a.O_2 \rightarrow b.CO_2 + c.H_2O \ldots\ldots E4.1$$

The number of moles of O_2 required and the number of moles of CO_2 and H_2O formed are not known. They can be determined by balancing the chemical equation. This calculation is shown below:

a) Carbon

$$C_{products} = C_{reactants}$$

$$b = 9.6 + 3.9 = 13.5$$

b) Hydrogen

$$H_{products} = H_{reactants}$$

$$2C = ((3.9 * 4) + (10 * 2)) = 35.6$$

$$c = 17.8$$

c) Oxygen

$$O_{products} = O_{reactants}$$

$$2b + c = 9.6 + (0.6 * 2) + 2a$$

Substituting the values of 'b' and 'c' in the above equation and calculating for 'a',

$$a = \frac{1}{2}\left((2 * 13.5) + (17.8) - 9.6 - (2 * 0.6)\right) = 17$$

Substituting thee values in E4.1, we obtain the combustion equation:

$$\mathbf{9.6CO + 3.9CH_4 + 10H_2 + 0.6O_2 + 17O_2 \rightarrow 13.5\ CO_2 + 17.8\ H_2O} \quad \text{....E4.2}$$

This is the equation for the stoichiometric combustion of the producer gases formed on the top of the fuel bed with air from the secondary nozzles. The air fuel ratios can be established using this equation. This is done in the next section.

4.2.1.2. AIR FUEL RATIO

From the combustion equation provided in E4.2, the stoichiometric molar air fuel ratio can be established. The equation is for 100 moles of the producer gas.100 moles of the fuel requires 17 moles of oxygen for complete combustion. Since air has 21% oxygen by volume, the number of moles of air required for stoichiometric combustion of 100 moles of the fuel is

$$N_{air} = \frac{A}{0.21} = \frac{17}{0.21} = 80.952$$

Therefore the molar air fuel ratio,

$$\left(\frac{A}{F}\right)_{stoichiometric} = \frac{N_{air}}{N_f} = \frac{80.952}{100} = 0.809$$

This is the molar stoichiometric air fuel ratio.

Now that the stoichiometric ratio is known, we calculate the actual air fuel ratio in the stove. The mass flow of the producer gas on the top of the fuel bed and the air entering the combustion chamber has already been calculated in sections 3.6.2 and 4.1.2 respectively. To establish the molar air fuel ratio, the molecular mass of the producer gas needs to be calculated. The molecular weight is calculated using the composition provided in table 4.8 as:

$$M_f = (X_{CO} * W_{CO}) + \left(X_{CO_2} * W_{CO_2}\right) + \left(X_{CH_4} * W_{CH_4}\right) + \left(X_{H_2} * W_{H_2}\right) + \left(X_{H_2O} * W_{H_2O}\right) + \left(X_{O_2} * W_{O_2}\right) + \left(X_{N_2} * W_{N_2}\right)$$

Here 'W' refers to the molecular weight of the individual components.

Substituting the molecular weights and using values from table 4.8, we obtain

$$M_f = 26.64g$$

This is the weight of one mole of the producer gas. Now the mass flow of producer gas on top of the fuel bed can be expressed in molar terms. From section 3.6.2, the producer gas mass flow at the top of the fuel bed is $W_f = 9.028*10^{-5}$ kg/s. Therefore the number of moles

$$N_f = W_f / M_f$$

$$N_f = 0.34 * 10^{-2}\ mol/s$$

Similar calculation is done for the case of air. The mass flow of air entering the combustion chamber has been calculated as W_s=26.65 *10^{-5} kg/s (per segment) in section 4.1.2. Considering the nitrogen volume fraction in air to be 79% and the oxygen fraction to be 21%, the molecular weight of air is

$$M_{air} = (X_{N_2} * M_{N_2} + X_{O_2} * M_{O_2})$$

$$M_{air} = 28.84\ g$$

Therefore the number of moles entering the combustion chamber through the secondary air nozzles is

$$N_{air} = \frac{W_s}{M_{air}} = 0.924 * 10^{-2}\ mol/s$$

Therefore the actual overall molar air fuel ratio for secondary combustion in the stove:

$$(\frac{A}{F})_{actual} = \frac{N_{air}}{N_f} = \frac{0.924 * 10^{-2}}{0.34 * 10^{-2}} = 2.72$$

The equivalence ratio defined as the ratio of the actual air fuel ratio to the stoichiometric air fuel ratio. It is expressed as

$$\varphi = (A/F)_{actual}/(A/F)_{stoichiometric}$$

Substituting the values calculated, we obtain the equivalence ratio of secondary combustion in the stove.

$$\varphi = 3.4$$

All the calculations are summarized in table 4.9.

Quantity	Value
Stoichiometric molar A/F ratio	0.809
Stoichiometric fuel mass fraction	0.553
Actual overall molar A/F ratio	2.72
Equivalence ratio	3.4

Table 4.9: Air fuel ratios

4.2.1.3. FLAMMBILITY LIMITS

The stoichiometric air fuel ratio only indicates the ratio required for the complete combustion of the fuel. A more useful property is the flammability limits. The flammability limits of air fuel mixture are the mixture fraction limits by volume that will burn indefinitely in the given conditions without further ignition. The wider the limits, easier the combustion.

For the producer gas the flammability lies in the range of 12-74% (Speight, 2010).

Now that the necessary reactant concentration levels have been established, we discuss the temperature requirement for the secondary combustion reaction.

4.2.2. TEMPERATURE DEPENDENCE

The rate of a reaction can be expressed as:

$$r_f = k_f \prod_{i=1}^{n} [M_i]^{p_i}$$

Where,
r_f = rate of the reaction, mol m^{-3} s^{-1}
k_f = Arrhenius rate constant
p_i= reaction order
$[M_i]$ – concentration of the reactants
(Fantini et al, 2014)

From the expression it is evident that the reaction rate is a strong function of the rate constant and the concentration of the reactants. The Arrhenius rate constant in turn is defined as:

$$k_f = k_0 e^{-\frac{E_a}{R_u T}}$$

Where,
k_f = Arrhenius rate constant
k_o = pre-exponential factor
E_a= Activation energy, J mol^{-1}
T= reaction temperature, K
R_u = universal gas constant, J mol^{-1} K^{-1}

The Arrhenius rate constant is varies exponentially with temperature. The activation energy term is also temperature dependent. Therefore temperature is the biggest influencing factor on the rate of the reaction. (Fantini et al, 2014)

The presence of the activation energy term in the rate constant equation means that there is a threshold temperature below which a reaction will not initiate. For the secondary combustion of the producer gases in a micro gasifier this value is around 700°C (Caregnato, 2011).

With the reactant concentration and the temperature range for secondary combustion now established, we proceed to the passive scalar implementation and mixing analysis.

4.3. PASSIVE SCALARS

A passive scalar is basically a diffusive contaminant that advects and diffuses with the flow without dynamically influencing it. Passive scalars are extensively used in combustion applications to analyze the mixing and transport of chemical species (Warhaft, 2000)

Figure 4.19 shows the passive scalar implementation in the current model. The wood gas and the air are the two species introduced. At the fuel bed the mass fraction of wood gas is specified as unity and at the nozzle inlet the mass fraction of air is unity.

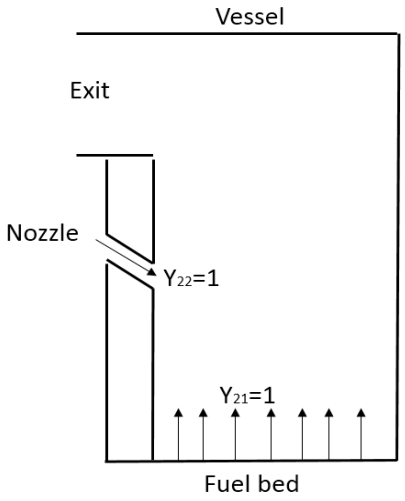

Figure 4.19: Passive scalar implementation

The scalar concentration profiles at different locations will shed light on the mixing behavior. The mixing behavior is studies for two different cases as shown in figure 4.20.

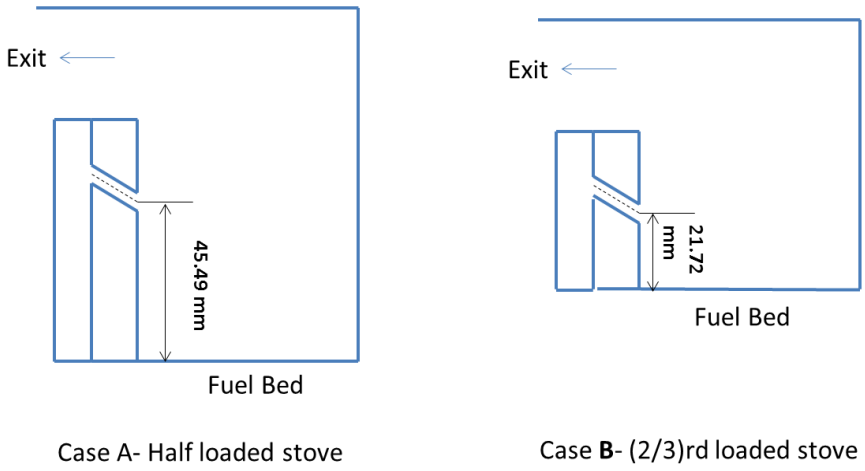

Figure 4.20: Different fuel loading

First is for a half loaded stove, hereby referred to as case A. The second case is when the stove is 2/3 loaded, hereby referred to as case B.

4.3.1. CASE A

The fuel mole fractions plotted for this case along two different planes is shown in figure 4.21.

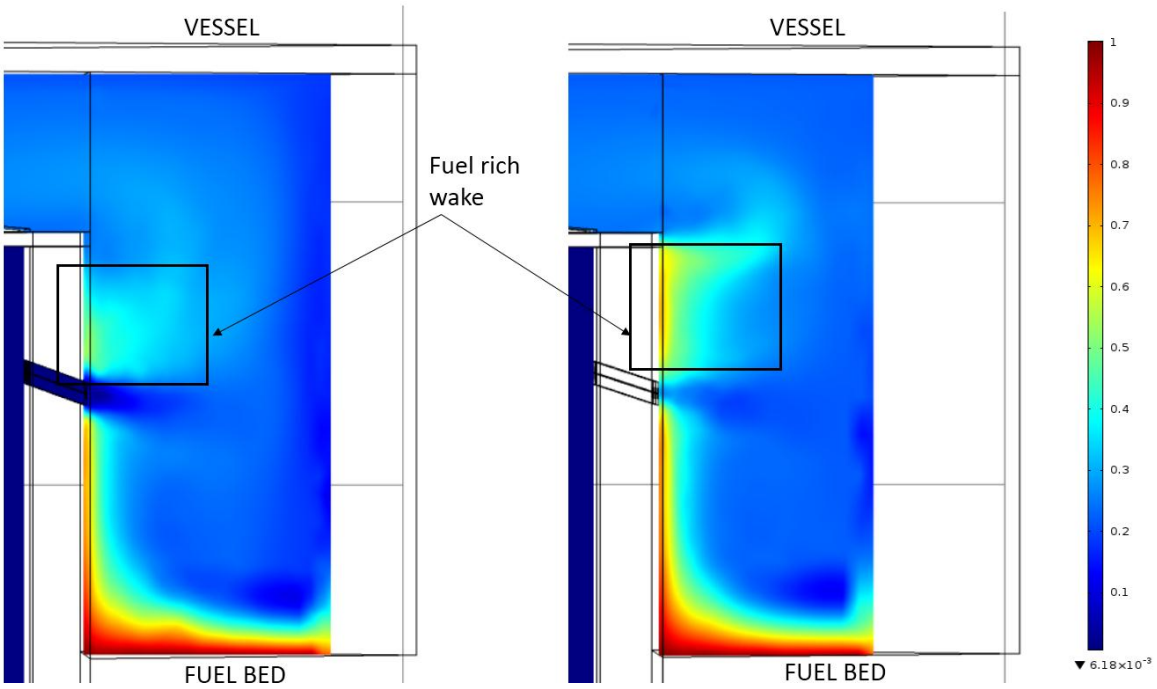

Figure 4.21: Fuel mole fractions, A) Along second nozzle center plane, y=0.01815m B) Away from nozzles, y=0.0315m

The stoichiometric molar fraction for the fuel (producer gas) is 0.553. It can be seen from figure 4.21 that the fraction is fuel rich in the following regions:
1) Along the walls of the combustion chamber,
2) Just above the fuel bed
3) Wake region above the nozzles

A rich mixture in the proximity of the fuel bed is expected. The rich mixture along the walls is because the fuel stream is suppressed by the air from the secondary nozzles. In the region between nozzles and away from the nozzles, a small fraction of this fuel rich stream escapes into the wake region. However, this fraction is very small as bulk of the particles are intercepted by the recirculation zone. The recirculation zone which extends to regions away from the nozzles too. This is ascertained by figure 4.21, where the air molar fraction profile for the two planes are almost identical.

Apart from the above mentioned regions, the mixture in the combustion chamber is overall on the leaner side. Also the bulk of the mixture, except at the top of the fuel bed and in regions close to the nozzle exit, lie within the flammability limit of 12% -74%.

The regions close to the nozzle exit is an area of intense mixing. This is because of the shear layer that is formed at the edges of the jet. Turbulent kinetic energy is a good measure of the velocity gradients, and hence of mixing. The normalized turbulent kinetic energy profile plotted for different downstream distances is provided in appendix C. The turbulent kinetic energy is highest along the edges of the jet because of the shear layer.

The air mole fraction along the height of the jet at different downstream distances is shown in figure 4.22. The co-ordinate system used is provided in figure 4.23.

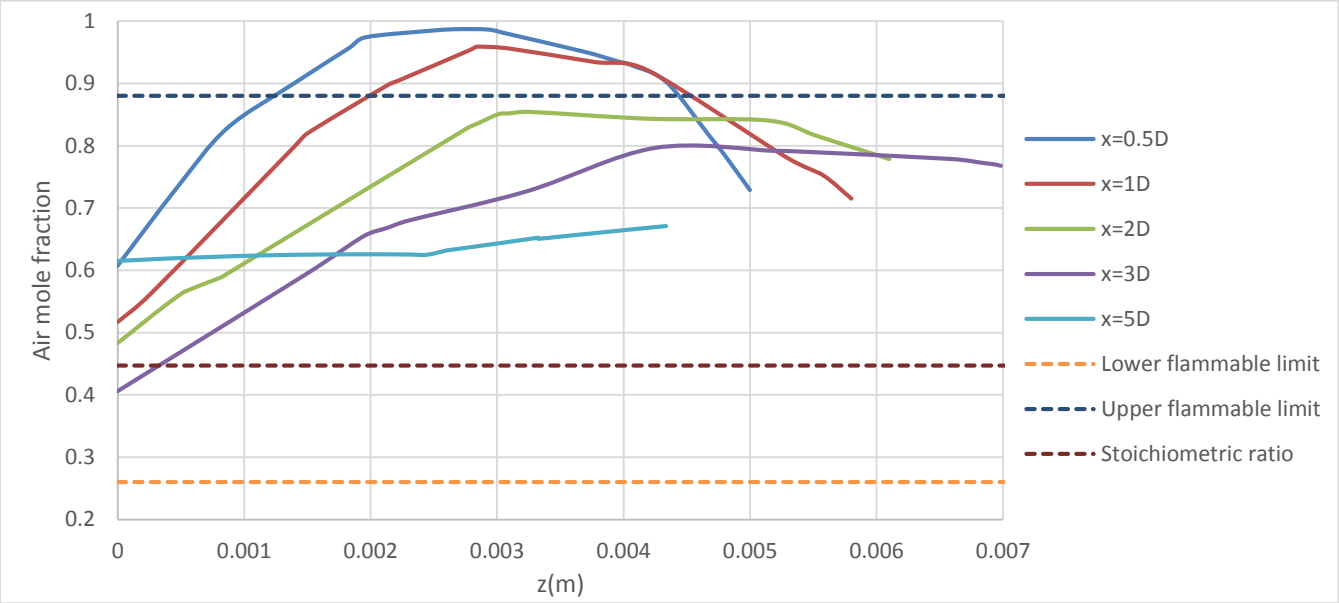

Figure 4.22: Mass fraction of air at different downstream distances along the jet trajectory

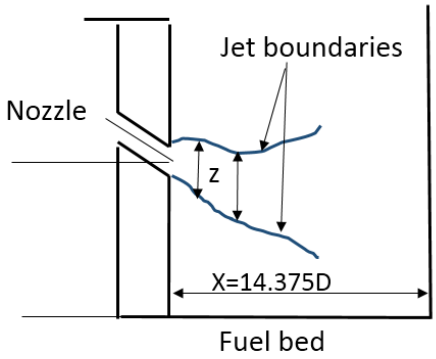

Figure 4.23: Co-ordinate system used for figure 4.21

The excellent mixing of the fuel and the air stream at the nozzle exit is evident from the fact that at downstream distances greater than x=1D, the bulk of the mixture is already within the flammability limits. The lower edges are closer to the stoichiometric ratio. Also noticeable is that mass fraction evens out for regions greater than x=3D indicating the bulk of mixing occurs very close to the nozzle exit.

The temperatures at the lower edges are above 700°C indicating this is a region where the probability of combustion is high. This analysis is validated by figure 4.24, which shows the actual flame pattern seen in the stove.

Figure 4.24: Flame pattern in the stove

The thin flame along the jet shear layer is clearly visible from figure 4.23. Also noticeable is the recirculation due to the collision of the jets at the center of the combustion chamber. Though, the flame pattern is for a different arrangement of nozzles, the observations are expected to be valid even for a single row of nozzles.

The mixture rising up vertically in the center of the combustion chamber and exiting the stove is very lean. This means that the bulk of the combustion occurs in the regions close to the fuel bed. The recirculation zone essentially traps the fuel particle rising from the fuel bed. The exiting upper stream can be seen to be composed of mainly of the products of combustion.

We now do a similar analysis for Case B.

4.3.2. CASE B

The flow pattern and the temperature profiles in the combustion chamber for this case are different when compared to case A. Figure 4.25 shows the fluid path lines plotted along two different planes. One along the center plane of the second nozzle and the second in a region away from the nozzles

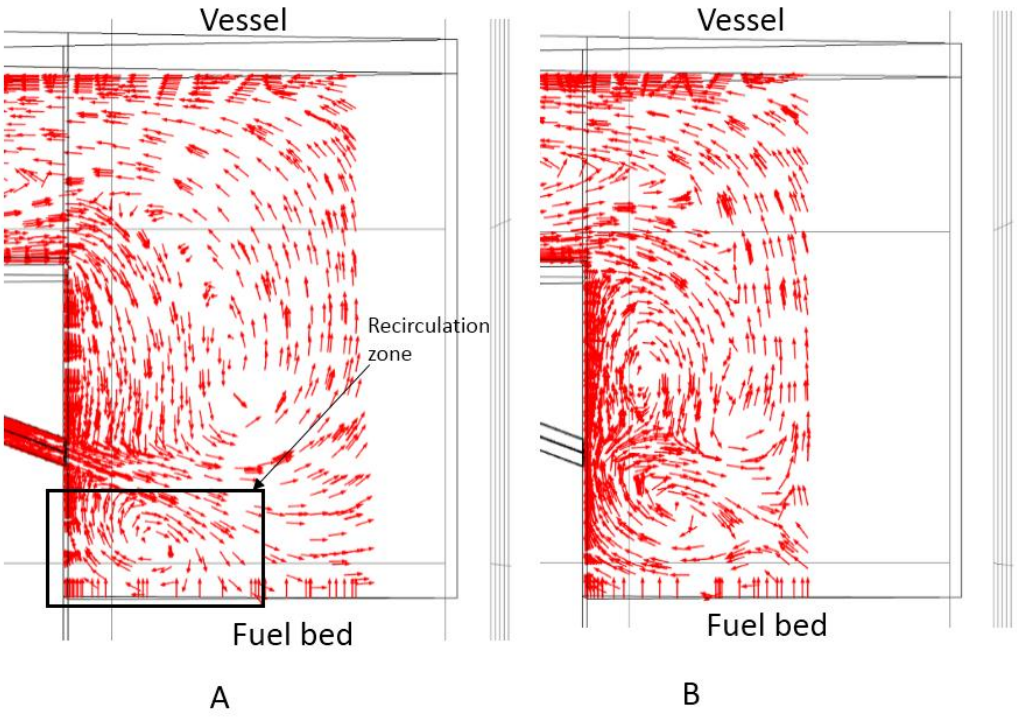

Figure 4.25: Fluid path lines: A) Along second nozzle center plane (y=0.01815m), B) Away from nozzles (y=0.03115m)

Unlike case A, the kidney shaped pattern is less pronounced for this case because of the smaller recirculation zone. A part of the fuel stream is driven towards the center of the combustion chamber by the lower edge of the jet. Compared to case A smaller proportion of fuel particles is forced towards the combustion chamber walls. Therefore circulation is weaker and the wall jet formed has a lower lateral velocity. Weaker crossflow effects result in a smaller jet spreading angle (lower edge) and deeper penetration of the jet into the combustion chamber. This can be seen from table 4.10 which provides a comparison of the jet properties for the two cases.

	Centerline velocity slope	Virtual origin	Spreading Angle(lower edge)
Case A	1.524	1.733	18.5°
Case B	2.716	2.2	15.93°

Table 4.10: Comparison of jet properties

In regions away from the nozzle, the weaker recirculation zone leads to a larger proportion (compared to case A) of fuel particles flowing into the wake formed above the nozzles.

Now that the flow field for this case has been analyzed, we proceed to the mixing analysis.

4.3.2.1. MIXING ANALYSIS

Figure 4.26 provides the fuel mole fraction plotted along two different planes. One along the second nozzle center plane, another away from the nozzles.

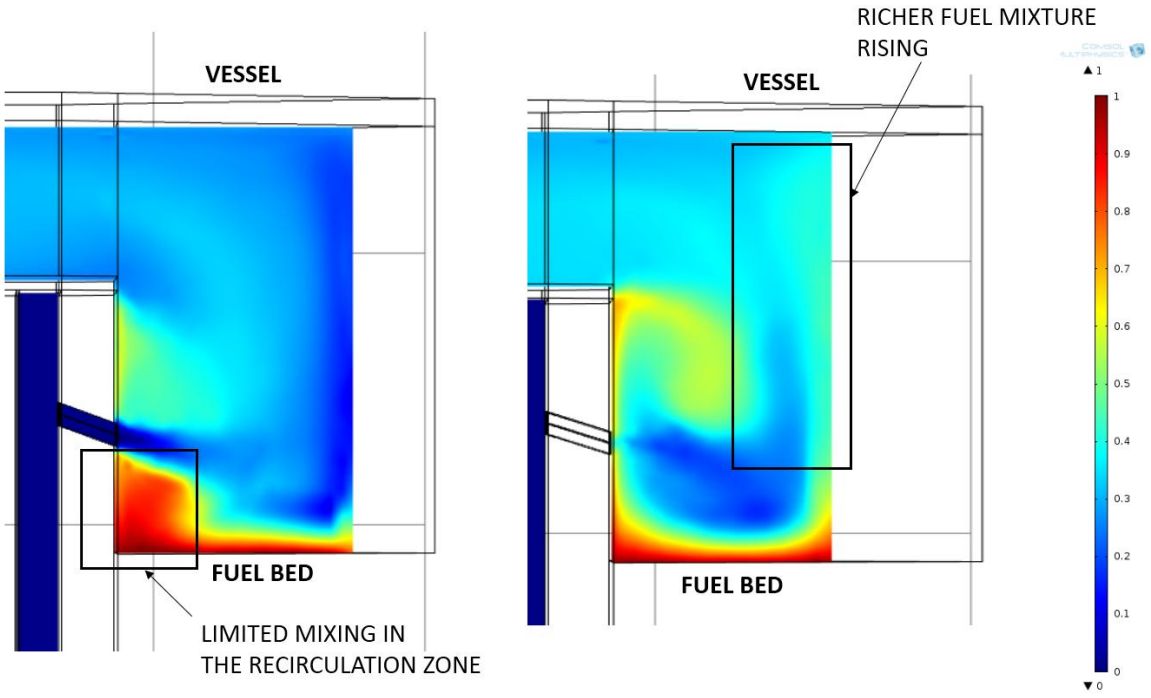

Figure 4.26: Fuel mole fraction- A) Along second nozzle center plane (y=0.01815m) B) Away from nozzles(y=0.03115)

Figure 4.26 reveals that the mixing behavior seen for this case is markedly different from case A. There is little or no mixing in the recirculation zone. For the plane along the nozzle center plane, the bulk of the mixing is closer to the center of the combustion chamber (apart from the nozzle edges). The mixing is non-uniform with pockets of fuel rich mixture above the upper flammability limit.

Like in case A, the wake is fuel rich, but the amount of fuel particles in this region is higher compared to case A. This is especially true along planes away from the nozzle center plane.

Another noticeable difference is that the mixture rising up along the center is close to the stoichiometric ratio. A comparison of the fuel average mass fraction of the vertical stream close to the center is provided in table 4.11.

	X_f	
y (m)	**CASE A**	**CASE B**
0.01815	0.22	0.28
0.03115	0.224	0.44

Table 4.11: Fuel mass fraction comparison

Compared to case A, the mixture fraction in the upper regions of the combustion chamber is closer to the stoichiometric limit for case B. This means that unlike in case A, combustion is not restricted to the lower regions of the combustion chamber. Operating close to the stoichiometric conditions raises the probability of incomplete combustion and may lead to higher emissions and is not desirable.

5. CONCLUSION

The Philips micro-gasifier stove has been developed based on experimental and empirical observations. Computational modelling is expected to bring down the design costs as well as accelerate the design process. Given the complexities involved in simulating combustion, identifying the right design space with the resources available is crucial. A comprehensive computational model of the stove require modelling the solid fuel bed, gas phase combustion (CFD and the chemistry model), flame and pollutant formation etc. In view of the time frame available, only the secondary combustion zone is modelled. A CFD model is developed to investigate the fluid flow and temperature profiles in the secondary combustion zone for the steady state operation of the gasifier stove in the flaming mode. The computational model is only expected to aid experimental design and not replace it.

A 3 dimensional model of the stove is built using COMSOL Multiphysics. Combustion is modelled as a volumetric heat source with uniform heat generation in the combustion chamber. The computational domain is restricted to one insulation tile, i.e. 1/9th of the entire stove. The effect of the neighboring domains is accounted for by using periodic boundary conditions. A 2^{nd} order discretization scheme is implemented and convergence is achieved with the domain described.

The flow field reveals that the producer gas rising from the fuel bed is suppressed by the high momentum jets. This interaction and the collision of jets at the center of the combustion chamber sets up a zone of intense recirculation. The absence of flow data inside the combustion chamber means that the results are only qualitative indicative of only the broader trends. However the simulation prediction are in sync with visual observations of the flame pattern in the stove.

The temperature field prediction inside the combustion chamber suffers from the uniform heat generation assumption. There exists ‘hotspots’ in the regions where the mass flow is restricted. In the wake region above the nozzles and around the stagnation region very high temperature ensues. This is not reflective of the actual operating conditions. For regions outside the combustion the values are comparable, still inaccurate. By including a more detailed design a close approximation of experimental values can be obtained.

However it has now been realized that the high temperatures inside the combustion chamber is largely due to the low secondary airflow rate specified in the simulation model. With a pressure of 30Pa specified at the annular chamber inlet, the secondary air flow rate is only 43% of the actual/experimental value. Initial results of simulations run with a higher secondary air flow report lower overall temperatures and a less pronounced hotspot in the wake region. It is expected that a close approximation of the operating conditions is possible if the right mass flow is specified at the annular chamber inlet.

Passive scalars are used to study the mixing of the air and the producer gas. The recirculation zone is found to have a significant influence on the mixing of the two streams. The analysis is done for two different heights of the fuel bed. At higher fuel bed heights it is found that the recirculation zone is limited in space limiting the mixing of the streams resulting in richer mixtures in regions away from the nozzles. The interpretation of the mixing analysis is again only qualitative.

The CFD model is only partially successful in meeting the objectives it was designed for. However it is still a good tool for visualizing the flow patterns. A better definition of the heat source term and modelling the reactive flow will make this a valuable design tool fit enough for integration into the design cycle.

6. FUTURE WORK

- Establishing the right secondary air flow rate will lead to a close approximation of the combustion chamber. However, the uniform heat generation assumption means there will be hotspots, even if less pronounced, that will influence the overall temperature field.
- To overcome this, the heat source term can be made proportional to the mixing of the air and the fuel stream. With this approximation a better approximation of temperatures in the combustion chamber is possible.
- Now that the significance of the recirculation zone is known, influence of nozzle diameter and nozzle angle on the recirculation zone should be studied.
- Reactive flow properties vary significantly from non-reactive flow. Therefore modelling the reactive flow is necessary for an accurate description of the flow behavior inside the combustion chamber. Starting with the basic combustion reactions, more species can be added on later if required.
- A detailed model of the flame will need switching to software packages with specialized combustion modules.

APPENDICES

APPENDIX A: Fan curve

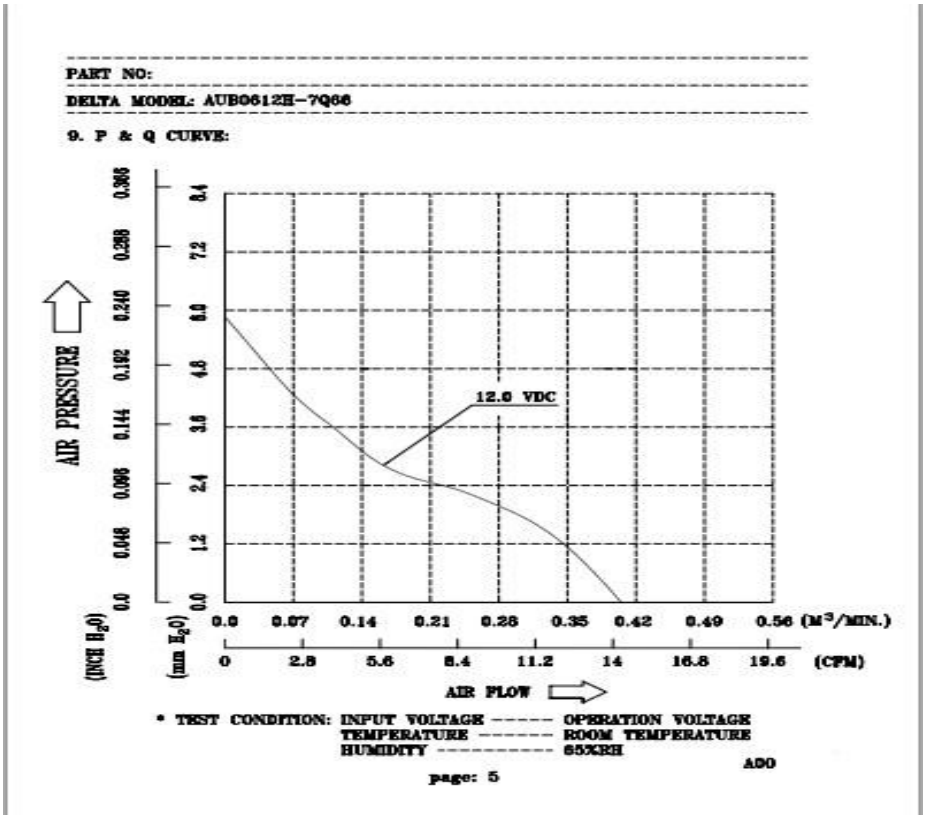

APPENDIX B: Reynolds number and Jet width

x	Case-A	Case -B
0.5	1.32	1.25
1.5	1.56	1.63
2	1.68	1.8
2.5	1.72	1.8
3	1.94	2
3.5	2.12	2.15
4	2.36	2.3
4.5	2.52	2.6
5	2.96	2.79

APPENDIX C: Normalized turbulent kinetic energy profiles

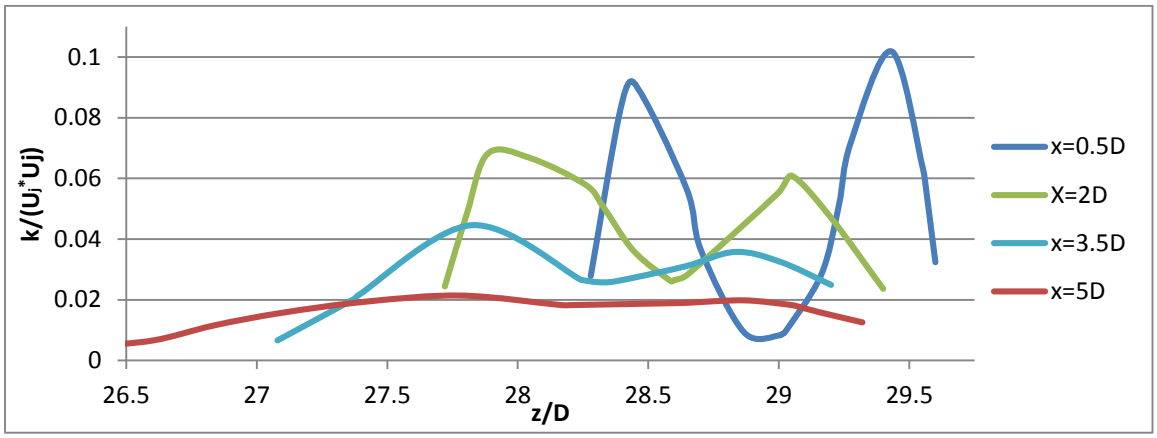

APPENDIX D

SIMULATION OF A HIGH REYNOLDS NUMBER TURBULENT ROUND JET (for validation of mesh)

D.1. OBJECTIVE

The objective of this exercise is to understand the accuracy of the mesh used in simulating turbulent flows. Only a comparison of the simulation and the experimental values is provided. A standard test case is simulated using COMSOL 4.4 and the results compared with experimental values to enable a better interpretation of the results.

A high Reynold's number turbulent round jet is chosen for study. Extensive analysis of the round jet is provided in Pope, 2000 using experimental data from Hussain et al, 1994. These references are used for this analysis.

Since the jet trajectory and spreading are the key areas of interest the study is focused on the following properties:

1) The centerline velocity decay
2) Radial velocity profile
3) Lateral velocity profile

D.2. FLOW DESCRIPTION

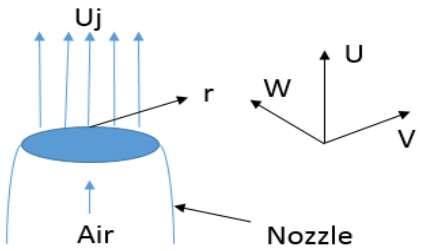

Figure D.1: Round jet and co-ordinate system used

The experimental set up consists of a jet of air exiting a nozzle into the stationary ambient fluid. The exit diameter of the nozzle is 2.54cms and the exit Reynold's number of the jet is 95500 (exit velocity - 56.2 m/s). The velocity profile is almost flat topped with constant velocity at all locations in the inlet. The flow is axisymmetric and the flow properties are time independent (Hussain et al, 1994).

D.3. COMPUTATIONAL DOMAIN

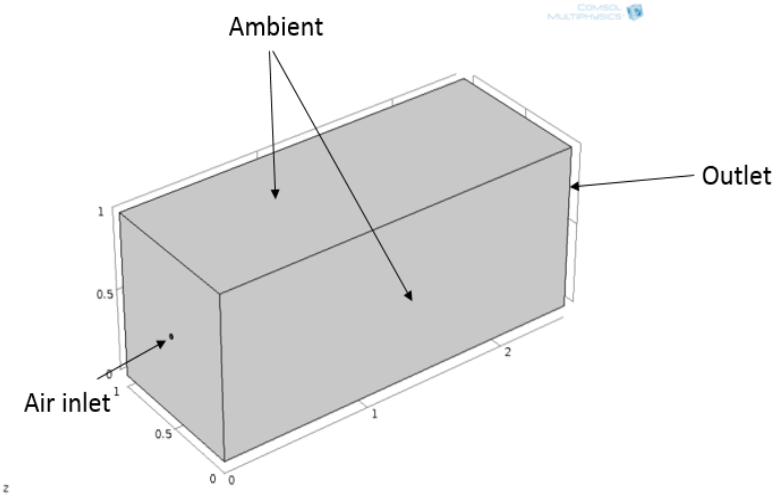

Figure D.2: Computational model

The computational domain is shown in figure D.2. Only the exit diameter of the nozzle is the relevant geometric parameter and the nozzle profile and the other details are not necessary. The computational domain extends to a distance of 100D along the X axis and approximately 40D along the Y and the Z axis.

D.4. BOUNDARY CONDITIONS

The inlet flow velocity of 56.2m/s forms the inlet boundary condition. A zero pressure condition marks the outlet and the ambient.

The inlet is slightly extended and as a consequence the inlet velocity profile is not a top hat/flat topped. There is a high velocity core and the velocity is lower along the nozzle walls. The velocity at the centerline at the nozzle exit increases by about 2%. Consequently the Reynold's number is slightly higher than 95500 at the exit as shown in Appendix D.A.
The turbulence intensity is set at 0.58% as specified in Hussain et al (1994). The turbulence length for a fully developed turbulent jet is 0.075L (COMSOL CFD user's guide, 2013). 'L' here is the jet diameter and hence the turbulence length scale calculated is 0.02032m.

D.4. MESH AND SOLVER

The default mesh settings used in the simulation of the stove is retained. A second order discretization in space and a direct solver is used.

D.5. RESULTS

D.5.1. CENTRELINE VELOCITY VARIATION

The centerline velocity of a self-preserving jet is represented by the equation:

$$U_c = BM^{0.5}\,(x - x_o)$$

In the non-dimensional form,

$$\frac{U_{jet}}{U_c} = \left(\frac{1}{B_u}\right)\left[\left(\frac{x}{D}\right) - \left(\frac{x_0}{D}\right)\right]$$

Where,
U_c - Centerline velocity, m/s
x - axial location, m
x_o - virtual origin, m
U_{jet} – Jet velocity at the nozzle exit, m/s
B_u- Decay constant (Hussain et al, 1994).

The normalized centerline velocity as predicted by the simulation is plotted along the length of the jet is given in figure D.3. The data is limited to region 0 and 40D.

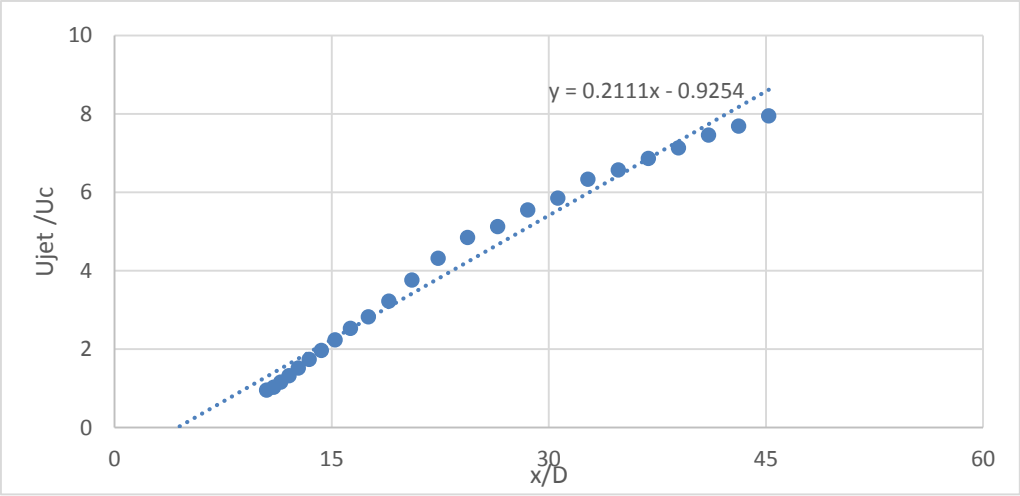

Figure D.3: Centerline velocity vs Axial distance, up to x=40D

The graph returns the equation, $y = 0.2111x - 0.9254$.
From this the calculated decay constant is $B_u = 4.74$ and the virtual origin is located at $x_0 = 4.38$.
The decay constant deviates from the experimental value by around -17%, while for the virtual origin the error involved is around 9.5%.
Similar calculation with the distance extended up to X=100D is done. The results for both the cases are tabulated in table D.1.

	B_u	x_0
Hussein et al,1994	5.7	4
Simulation (x/D,0-100)	8 (error = 40%)	6.355 (error =58.875%)
Simulation (x/D,0-40)	4.74(error = -17%)	4.38 (error =9.5%)

Table D.1 : Centerline velocity decay- Experimental and simulation values

It can be seen from table D.1 that the error involved for the data range of X=0 -100D is substantial. This indicates that the simulation is not very successful in predicting the centerline velocity decline for downstream distances greater than 40D. However, for smaller distances the values are more comparable.

One reason for the variation is the nature of velocity profile at the nozzle inlet. A closer approximation of a flat top velocity profile could reduce the error further for distances lower than 40D. At greater downstream distances, the domain might not be wide enough affecting the quality of the results.

D.5.2. RADIAL PROFILE OF AXIAL VELOCITY

The radial profile of axial velocity is of interest as it indicates the spreading of the jet. Figure D.4 shows the axial velocity plotted against radial distance. The velocity is normalized with the exit velocity of the jet while the radial distance is normalized with the jet diameter.

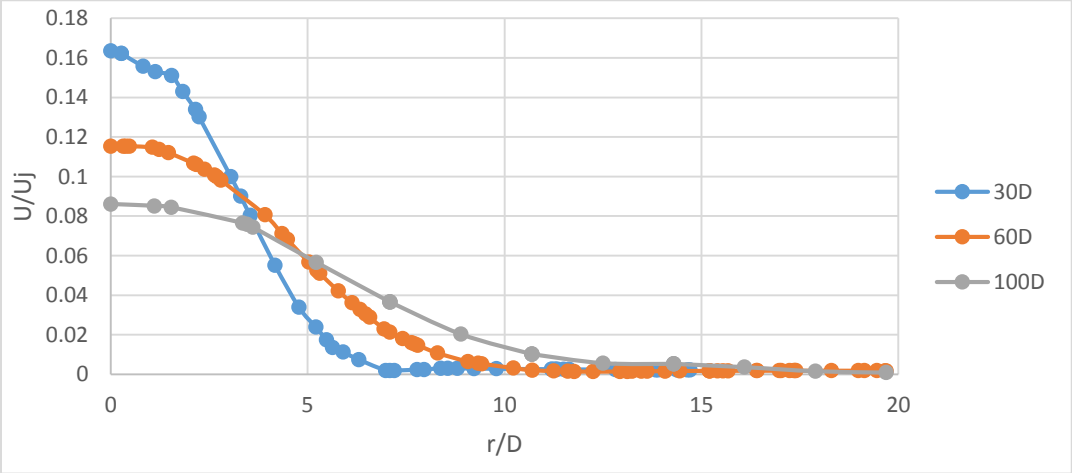

Figure D.4: Radial velocity profiles-Simulation values

The radial velocity profile seen in figure D.4 is similar to that reported in Pope, 2000. A comparison of the normalized velocity at the center of the jet is shown in table D.2.

	Simulation	Experimental (Hussein et al,1994)	Error
X=30D	0.161	0.22	-27.3 %
X=60D	0.19	0.105	81%
X=100D	0.082	0.06	37%

Table D.2: U/U_j -Simulation vs Experimental

The simulation predicts a lower velocity magnitude at the centerline at a distance of x=30D, but a higher magnitude for x=60D and x=100D. The error levels for downstream distances are greater as is the case for centerline velocity decay.

Another property of interest is the radius at which the velocity becomes zero. Table D.3 provides a comparison of the simulation results and the experimental values

	Simulation	Experimental	Error
X=30D	6.5D	7D	-7.1%
X=60D	12D	13D	-7.7%
X=100D	18D	22D	-18.2%

Table D.3: Zero velocity locations

The trend of lower error values at smaller downstream distances is repeated for this case also. Compared to the velocity magnitude, the error involved is smaller. At all downstream distances, the simulation returns values lower than the experimental predictions.

D.5.3. SELF SIMILARITY

To check for self-similarity the radial profile of velocity is plotted for different distances. The velocity is normalized with the centerline velocity of the jet at that particular distance while the axial distance is normalized with the exit diameter of the jet. The resulting plot is shown in figure D.5.

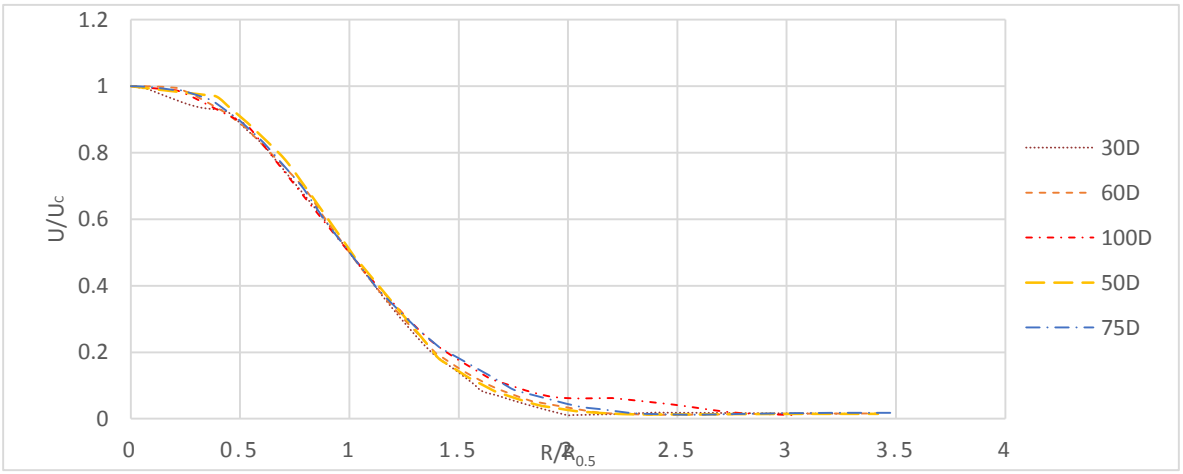

Figure D.5: Axial velocity - Self similarity

There is a great degree of overlapping of the curves drawn at different distances. While the profile plotted at a distance of x=100D seems to have a slightly different shape, overall, the shapes of the profiles at other downstream distances are similar. The curves are plotted for distances between x=30D and x=100D and it is safe to assume that the velocity profiles are self-similar in this range.

D.5.4. LATERAL VELCOITY

Figure D.6 shows the plot of mean lateral velocity as a function of the radial distance of the jet. The velocity is normalized by the jet exit velocity and the radial distance by $r_{0.5}$.

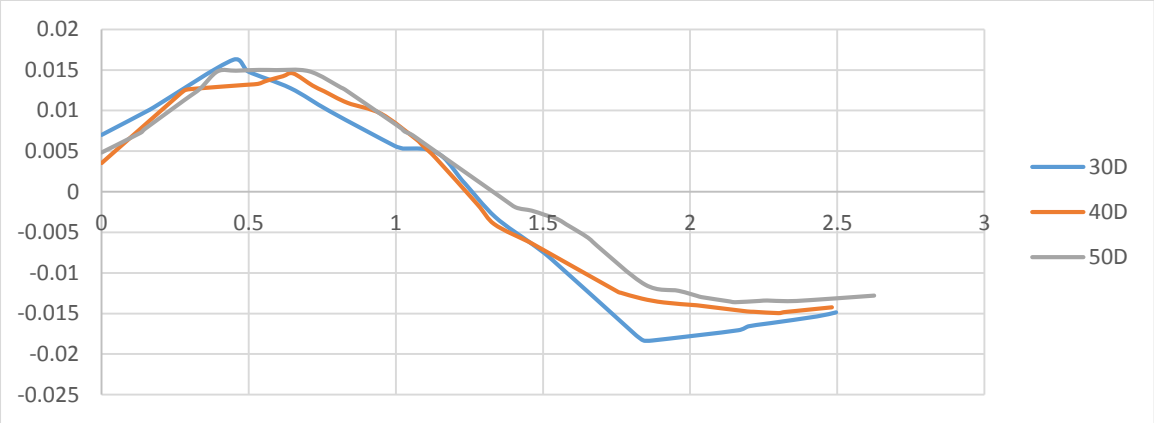

Figure D.6: Lateral velocity profiles-Simulation data

The point of entrainment of the surrounding fluid into the jet occurs at the edges of the jet where the lateral velocity is negative. The simulation predicts a lower value of the lateral velocity and predicts entrainment at a lower radius.

Table D.4 is a compilation of the experimental and the simulation values.

	Maximum value V/U_0	Point of entrainment
Experimental	0.019	1.5 *$r_{0.5}$
Simulation, X=30D	0.015	1.25*$r_{0.5}$
Simulation, X=50D	0.015	1.3*$r_{0.5}$
Simulation, X=60D	0.015	1.25*$r_{0.5}$

Table D.4: Lateral velocity - experimental and simulation values

Also the degree of the overlapping observed for this case is to a lesser degree compared to the axial velocity curves.

D.6. CONCLUSION

It is safe to conclude that the simulation is only partially successful in simulating the high Reynold's number turbulent round jet.

The centerline velocity predicted by the simulation shows significant errors in regions from x=40D to x=100D. When the data is limited to a distance if x=40D, the error in decay constant comes down from 40% to 9.5 %. The error can further be reduced if a closer approximation of a flat velocity profile can be achieved at the inlet.

The radial profile of velocity plotted for different distances was self-similar and there is a great degree of overlap for curves drawn at different distances. The velocity variation along the radius is similar to experimental observations. However the magnitude of velocity as predicted by the simulation deviates significantly from experimental observations. For distances less than 30D, this deviation is around 27%.

The lateral velocity predictions is in agreement with experimental values. The magnitude is about 20% lower than the experimental values. Also the radius of entrainment, predicted by the simulation is lower by about 18% than experimental data suggesting that the model under-predicts the spreading rate of the jet.

The simulation returns a more accurate solution at distances closer to the nozzle exit. Because the distances in the combustion chamber are within x=15D, the error values are within acceptable limits.

APPENDIX D.A: Reynold's number along the length of jet

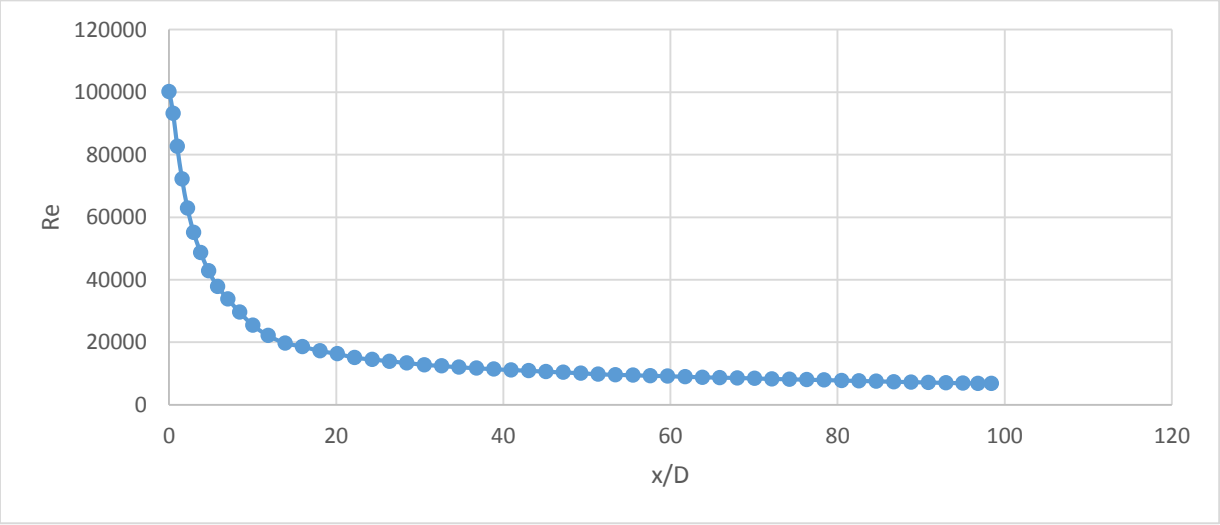

APPENDIX E

NUMERICAL DIFFICULTIES IN SOLVING NS EQUATIONS

In this section how finite element methods tackle the challenges that arise in modelling of flow is explained.

There are several difficulties that might arise when numerically solving for the Navier- Stokes equations. Numerical difficulties can arise for -

1) Convection dominated flows
2) Low Mach number flows

We briefly describe each of them below.

1) Convection dominated flows

Momentum equation is a non-linear partial differential equation with source terms. Special iterative techniques are required to accommodate the non-linearity at higher Reynold's number where the flow is convection dominated flow. Non-linear convective terms from the momentum equation pose numerical challenges at higher Reynold's numbers. In FEM methods this is dealt with by damping the convective term by adding artificial diffusion. (Fletcher, 1991)

The Galerkin based FEM enormously successful for a variety of applications has some severe limitations when applied to advection dominated problems (Urgen et al, 2000). The solution for the convection-diffusion equation is convective over most domains and the diffusive parts is restricted only to smaller sub-domains giving rise to sharp gradients and boundary value problems. FEM methods are best suited to elliptic problems and at higher Peclet numbers when parts of the equation becomes hyperbolic, numerical instabilities are observed. The instabilities manifest in the form of spurious oscillations and wiggles (Chaple, 2006).
This is also observed in other classical numerical approaches like the finite volume and the finite difference methods. One solution to this is to refine the mesh and reduce the Peclet number, ensuring convection does not dominate at the cells. This is unsuited for practical applications as it will increase the computational effort. In finite volume and finite difference methods, upwind discretization is used to tackle the issue of spurious oscillations.

Upwinding is a technique that is employed extensively in the central difference scheme to overcome the wiggles and the spurious oscillations arising. It is a discretization scheme which uses the flow of an influence from the neighboring grid points (Versteeg and Malasekera, 1995). In finite volume methods upwinding of hyperbolic system of equations is achieved through flux splitting.

As mentioned earlier in the finite element method, upwinding is achieved by adding artificial diffusion. For one dimensional problems exact solutions can be attained using this method.

There are two ways in which the artificial diffusion can be introduced
1) Modification of the terms in the original equation
2) Modification of the shape function

The modification may be introduced a priori leading to schemes depending on a free parameter or may be obtained naturally as a consequence of other considerations. Figure E.1 shows a modified weigh function where the upwind node is weighed more heavily than the downstream one.

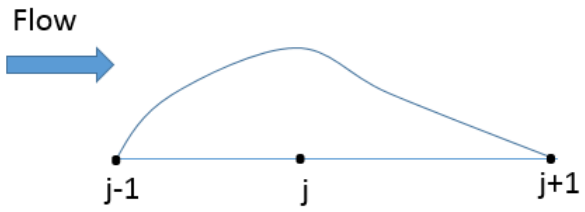

Figure E.1 : Upwinded weight function (Donea, 2003)

The two most prominent upwind finite element methods based on the modification of the weight functions are:
1) Streamline Upwind Petrov Galerkin methods (SUPG)
2) Galerkin least squares method (GLS)

1) SUPG method: This method is based on the principle of modifying the weighing function. A diffusion term is added to the original equations which might override the viscosity term in the advection diffusion equation.

The classical Galerkin formulation of the standard advection diffusion equation can be stated as

$$B^g(w_h, a_h) = \int_\Omega w_h\left(\frac{\partial a_h}{\partial t} + \frac{\partial v a_h}{\partial x}\right) dx$$

In the SUPG method, the weighing functions are modified to include upwinding as described in figure E.1. The piece-wise approximation described in the earlier sections is modified as

$$\overline{w_h} = w_h + \tau v \frac{\partial w_h}{\partial x}$$

The weighing function depends on the free parameter τ. It is chosen so as to compensate for the negative diffusion. It is also referred to as the 'stabilization' parameter. (Pegon et al, 1993)

The modified weighing functions are applied to all the terms of the equation and not just convection term. If restricted to the convection term alone it results in a non-residual formulation which results in an inaccurate solution in source dominated flows (Polner, 2005).

The term streamline upwind is used because the standard weighing functions are modified by adding streamline upwind perturbation acting only in the flow direction. This is necessary to avoid the problem of crosswind diffusion which is caused by the addition of unnecessary diffusion perpendicular to the direction of the flow. This is avoided in streamline upwind methods as diffusivity introduced acts only in the direction of the flow. (Donea, 2003)

The method even though accurate is hindered by its free parameter dependence which limits it scope of application. Also the method is computationally more expensive than the finite volume upwind formulations. A detailed analysis of the accuracy and convergence behavior of this method can be found in Donea, 2003.

2) Galerkin least squares method: In the GLS method the stabilization parameter is obtained by minimizing the square of the equation residual. This method offers an implicit way of solving the advection diffusion equation by eliminating the dependence on any external parameter. Also when applied to hyperbolic system of equations this methods resulted in symmetric formulations.

In the least squares method the advection model equation is solved as

$$I\left(n + \left(\frac{1}{2}\right)\right) = \int_\Omega \left(\left(\frac{\partial a}{\partial t} + v\,\frac{\partial a}{\partial x}\right)\right)^2 dx = 0 \quad \text{(Carey and Jiang, 1988)}$$

The following approximations are introduced

$$\frac{\partial a}{\partial t}\Big|^{n+\frac{1}{2}} = \frac{a^{n+1} - a^n}{\Delta t}$$

$$\frac{\partial a}{\partial x}\Big|^{n+\frac{1}{2}} = \left(\frac{1}{2}\right)\left(\frac{\partial a}{\partial x}\Big|^{n+1} + \frac{\partial a}{\partial x}\Big|^{n}\right)$$

The first variation of $I\left(n+\left(\frac{1}{2}\right)\right)$ with respect to a^{n+1}, the weak Galerkin approximation can be expressed as

$$B^{LS}_{w_h,a_h} = \int_{\Omega} (w_h + (\left(\frac{v\Delta t}{2}\right)\frac{\partial w_h}{\partial x})\left(\left(a_h^{n+1} - a_h^n\right) + \left(\frac{v\Delta t}{2}\right)\left(\frac{\partial a_h^n}{\partial x} + \frac{\partial a_x^{n+1}}{\partial x}\right)\right)dx$$

Where the modified weight equation is expressed as:

$$\overline{w_h} = w_h + (\left(\frac{v\Delta t}{2}\right)\frac{\partial w_h}{\partial x})$$

The modified weight function no longer depends on any external parameter. Like in SPUG, the perturbation term is mesh dependent. The GLS method is very similar to the SPUG method and for the advection diffusion equation both the methods are the same. The GLS method is a more general stabilization approach and can be applied to a range of fluid flow problems (Pegon et al, 1993).

A limitation of both the GLS and the SUPG method is the possibility of oscillations where discontinuities are present. A discontinuity capturing term is added to the standard formulation to overcome this. The discontinuity capturing term acts in a direction of the solution gradient rather than streamline direction.

Both SPUG and the GLS formulations can be extended to the NS equations. Extension of these methods to incompressible NS equations is available in Polner (2005).

The CFD module in COMSOL Multiphysics employs the GLS method to solve for fluid flows. While the basic principles of the GLS method has been explained in the earlier sections, the application to NS equations is done similar to the way shown in Hauke and Hughes, 1994.

2. LOW MACH NUMBER FLOW

The compressible form of Navier- Stokes Stokes equation allows for two kinds of propagation of speeds. The fluid velocity and the velocity of the sound. The two are related by a dimensionless number called the Mach number which is defined as the ratio of the fluid velocity to the velocity of sound at that particular temperature. Therefore

$$Ma = \frac{|u|}{c_s}$$

For compressible flow, the momentum equation is parabolic for non-stationary flow and elliptic for stationary flow. The continuity equation is hyperbolic for both stationary and non-stationary flow. Therefore the equation system is hybrid parabolic-hyperbolic for non-stationary flow and hybrid elliptic-parabolic for stationary flow.

In many practical applications, the fluid velocity is small in comparison to the speed of sound i.e. the Mach number is very low. At such lower Mach numbers, due to rapid equalization of pressure the fluid cannot sustain the large pressure gradients. If the temperature variations are small enough. The Boussenisq approximation is used or the incompressible Navier- Stokes Stokes equation can be applied. However when the temperature variations are substantial, the density of the fluid becomes temperature dependent rather than pressure dependent. Such a scenario occurs in combustors, reactors where the fluid

undergoes large temperature changes. In such a regime the pressure waves propagate at an infinite speed resulting in a parabolic system of equations.
When fully compressible Navier- Stokes –Stokes equation is applied to such flows, numerical difficulties arise. Since there is density variation the incompressible Navier- Stokes-Stokes equation cannot be used either. Therefore low Mach number flows need to be treated separately.
Considering a simple case of a low Mach number isentropic flow.
Expressing pressure as a function of density and using the continuity equation results in:

$$\frac{\partial P}{\partial t} + \rho c_s^2 \nabla . v + v . \nabla p = 0$$

The linearization of the conservation equations can be written as :

$$\frac{\partial u}{\partial t} + A(u)\frac{\partial u}{\partial x} = 0$$

Where$u = (\rho, v, p)^T$, the matrix A (u) is given by

$$A = \begin{bmatrix} v & \rho & 0 \\ 0 & v & \rho^{-1} \\ 0 & \rho c_s^2 & v \end{bmatrix}$$

The eigen values of A are - λ_1=v, $\lambda_{2,3}$ =v±c_s which correspond to the convective waves and sound waves. At lower Mach numbers, because the two velocities differ significantly, the poorly distributed eigen values leads to a stiff formulation. For accurate calculation the time step involved in the numerical method has to be low, which may not be practical.

For finite volume methods there are several methods employed to overcome this challenge.
Classical stabilized finite element formulations like SPUG and GLS methods are not equipped to deal with these discrepancies. At lower Mach numbers, the stabilization matrix is inadequate. There is a loss of accuracy as the Mach number of the flow reduces. The degradation of accuracy is due to the mismatch between the fluxes in the original equation and the amount of artificial viscosity added. (Donea, 2003) Suitable pre-conditioning is required to compensate for the loss of accuracy can be compensated. Wong et al, 2001 reports the use of specific pre-conditioners which have proven to be very successful. The stabilization matrix too needs modifications. Yu et al, 1995 developed a least square based finite element method which when applied to low Mach number flows lead to a symmetric positive definite matrix.

COMSOL has a separate interface for High Mach number flows. The Mach number effects are assumed to begin at around Ma= 0.3, so for flows higher than Ma=0.3. COMSOL has a dedicated numerical scheme which is able to capture the sharp gradients observed in high Mach number flows. Also special boundary conditions to incorporate for the shock waves and expansion waves is incorporated. For flows< Ma=0.3, the compressible formulation of the Navier- Stokes equation is used, however, the density is assumed to be a function of the temperature alone and not pressure. (COMSOL CFD User's guide, 2013).

BIBLIOGRAPHY

Arnold, J. E. M., Kohlin, G., Persson, R., & Shepherd, G. (2003). *Fuelwood Revisited: What has changed in the last decade?* (No. CIFOR Occasional Paper no. 39, pp. viii-35p). CIFOR, Bogor, Indonesia.

Bergman, T. L., Incropera, F. P., & Lavine, A. S. (2011). *Fundamentals of heat and mass transfer*. New Jersey: John Wiley & Sons.

Bhattacharya S.C, Leon MA, (2005), '*Prospects for Biomass Gasifiers for Cooking Applications in Asia*'. World Renewable Energy Regional Conference, pp. 18-21.

Chaple, B.R. P. (2006). *Numerical stabilization of convection-diffusion-reaction problems*. Delft University of Technology, Faculty of Electrical Engineering, Mathematics and Computer Science, Delft Institute of Applied Mathematics.

Bruce, N., Rehfuess, E., Mehta, S., Hutton, G., Smith, K. (2006). *Indoor air pollution, Disease Control Priorities in Developing Countries 2nd ed.* Oxford University Press, New York.doi:10.1596/978-0-821-36179-5/Ch-42, pp. 793–816.

Bussmann, P. J. T., Prasad, K. K., (1982). *Model predictions of temperature and velocity profiles in turbulent diffusion buoyant flames*. Proceedings of the 7th International Heat Transfer Conference EN4.

Bussmann, P.J.T., Visser, P., Prasad, K. (1983). *Open Fires: Experiments and Theory*. Proceedings of the Indian Academy of Sciences, Engineering Sciences, 6(1):1-34.

Caregnato, D. (2011). *Micro-gasification – Cooking applications for developing countries*. Retrieved from http://stovecamp.altervista.org/wp-content/uploads/2011/09/Caregnato.pdf

Carey, G. F., & Jianng, B. N. (1988). Least-squares finite elements for first-order hyperbolic systems. *International journal for numerical methods in engineering*, *26*(1), 81-93.

COMSOL CFD module User's guide. (2013). Retrieved from www.nf.nci.org.au/facilities/software/COMSOL/4.3/doc/pdf/mph/COMSOLMultiphysicsUsersGuide.pdf.

Cook, R.D. (2007). *Concepts and applications of finite element analysis*. New Jersey: John Wiley & Sons.

Çengel, Y. A., Cimbala, J. M. (2006). *Fluid mechanics: Fundamentals and applications*. Boston: McGraw-Hill Higher Education.

Global Alliance for Clean Cook stoves. (2012). *Clean Cooking Catalog*. Retrieved from http://catalog.cleancookstoves.org/#/stoves/47.

DeFoort, M. (2015). *Achieving Tier 4 Emissions and Efficiency in Biomass Cookstoves.* Presentation, Colorado. Retrieved from http://energy.gov/sites/prod/files/2015/04/f21/cookstoves_defoort_5211.pdf.

Donea, J., Huerta, A. (2003).*Finite Element Methods for Flow Problems*. New Jersey: John Wiley and Sons.

Engineering Toolbox, *Emissivity coefficients of some common Materials.* Retrieved from http://www.engineeringtoolbox.com/emissivity-coefficients-d_447.html

Fantini, M., De Jong, W. and Van Ommen, J. R. (2014). *Reactions, in Biomass as a Sustainable Energy Source for the Future: Fundamentals of Conversion Processes* (eds W. De Jong and J. R. Van Ommen), John Wiley & Sons, Inc, Hoboken.

Fatehi, M., & Kaviany, M. (1994). Adiabatic reverse combustion in a packed bed. *Combustion and Flame*, *99*(1), 1-17.

Fletcher, C. A. J. (1990).*Computational Techniques for Fluid Dynamics*, Sydney: Springer-Verlag.

Global Alliance for Clean Cookstoves. (2015). *Phase 1 Report*, Retrieved from http://cleancookstoves.org/binary-data/RESOURCE/file/000/000/283-1.pdf

Goldemberg, J., Johansson, T. B., Reddy, A. K., & Williams, R. H. (2004*). A global clean cooking fuel initiative*. Energy for Sustainable Development, 8(3), 5-12.

Gupta, R., & Mittal, N. D. (2010). Fluid flow and heat transfer in a single-pan wood stove. *Int J Eng Sci Technol*, *2*(9), 4312-4324.

Hauke, G., & Hughes, T. J. R. (1994). *A unified approach to compressible and incompressible flows*. Computer Methods in Applied Mechanics and Engineering, *113*(3), 389-395.

Hussein, H. J., Capp, S. P., & George, W. K. (1994). Velocity measurements in a high-Reynolds-number, momentum-conserving, axisymmetric, turbulent jet. *Journal of Fluid Mechanics*, *258*, 31-75.

International Energy Agency. (2006). *World Energy Outlook*, pp 419:445 retrieved from http://www.worldenergyoutlook.org/media/weowebsite/2008-1994/WEO2006.pdf

International Energy Agency (IEA). (2015). *Energy and Climate Change*, World Energy Outlook, Paris. pp 16:19

Jetter, J., Zhao, Y., Smith, K. R., Khan, B., Yelverton, T., DeCarlo, P., & Hays, M. D. (2012). *Pollutant emissions and energy efficiency under controlled conditions for household biomass cookstoves and implications for metrics useful in setting international test standards*. Environmental science & technology, 46(19), 10827-10834.

Jetter, J. (2012), *Proposed Emissions Tiers for Rating of Cookstoves*, Presentation, The Hague. Retrieved from http://www.pciaonline.org/files/10-Performance-Measures-web.pdf

Wong, J. S., D. L. Darmofal, and J. Peraire. (2001).*The solution of the compressible Euler equations at low Mach numbers using a stabilized finite element algorithm.* Computer Methods in Applied Mechanics and Engineering, 190:5719–5737.

Khan, A. A., W. De Jong, et al. (2009). *Biomass combustion in fluidized bed boilers: Potential problems and remedies*. Fuel Processing Technology 90: 21-50

Keyes, D. E., McInnes, L. C., Woodward, C., Gropp, W., Myra, E., Pernice, M., & Wohlmuth, B. (2013). Multiphysics simulations Challenges and opportunities. *International Journal of High Performance Computing Applications*, *27*(1), 4-83.

Kurkela, E., & Staåhlberg, P. (1992). Air gasification of peat, wood and brown coal in a pressurized fluidized-bed reactor. II. Formation of nitrogen compounds. Fuel processing technology, 31(1), 23-32.

Lacrosse L. (1990).*Contribution à l'étude du comportement des combustibles ligno-cellulosiques en gazogènes à lit fixe et à tirage inversé*. Thèse de doctorat. Faculté des Sciences Agronomiques de Gembloux.

MacCarty, N., Ogle, D., Still, D., Bond, T., Roden, C., & Willson, B. (2007). Laboratory comparison of the global-warming potential of six categories of biomass cooking stoves. *Creswell, OR: Aprovecho Research Center*.

MacCarty, N., Still, D., & Ogle, D. (2010*). Fuel use and emissions performance of fifty cooking stoves in the laboratory and related benchmarks of performance*. Energy for Sustainable Development, 14(3), 161-171.

MacCarty, N. A. (2013). *A zonal model to aid in the design of household biomass cookstoves*. (Master's Thesis, Iowa State University). Retrieved from http://lib.dr.iastate.edu/cgi/viewcontent.cgi?article=4596&context=etd.

Mando, M. (2013).*Direct Combustion of Biomass*. Biomass Combustion, Science, Technology and Engineering, 61-83.

Mathieu, P., Dubuisson, R. (2002). *Performance analysis of biomass gasifier*, Energy Conservation Manage, 43, pp. 1291–1299.

McKendry, P. (2002). Energy production from biomass (part 1): overview of biomass. *Bioresource technology*, *83*(1), 37-46.

McKendry, P. (2002). Energy production from biomass (part 2): conversion technologies. *Bioresource technology*, *83*(1), 47-54.

Menon, S., Koch, D., Beig, G., Sahu, S., Fasullo, J., & Orlikowski, D. (2010). Black carbon aerosols and the third polar ice cap. *Atmospheric Chemistry and Physics*, *10*(10), 4559-4571.

Morgan Thermal Ceramics, *Firelite LWHS* [Fact sheet]. Retrieved from http://www.morganthermalceramics.com/sites/default/files/datasheets/firelite_lwhs_-_metric.pdf

Morini, G. L. (2014). Viscous Heating. In *Encyclopedia of Microfluidics and Nanofluidics* (pp. 1-11). Springer US.

Nilsson, S., A. Gómez-Barea, et al. (2012). *Gasification reactivity of char from dried sewage sludge in a fluidized bed.* Fuel 92: 346-353.

Pegon.P, Soria.A. & Laval.H. (1993), *A Review of Finite Element Solvers for the Compressible Navier-Stokes Stokes Equations.* Notes by Commission of European Communities, Joint Research Centre. ESCSC-EEC-EAEC Brussels.

Polner, M. (2005). *Galerkin Least-Squares Stabilization Operators for the Navier- Stokes-Stokes Equations: A Unified Approach*. University of Twente.

Pope, S. (2000). *Turbulent flows*, Cambridge: Cambridge University Press.

Ramanathan, V., & Carmichael, G. (2008). Global and regional climate changes due to black carbon. *Nature geoscience*, *1*(4), 221-227.

Reed, T. B., Walt, R., Ellis, S., Das, A., & Deutch, S. (1999). Superficial velocity-the key to downdraft gasification. *Proceedings of the 4th biomass conference of the Americas. Oakland, CA* (pp. 1-8).

Roth, C. (2011). Micro-gasification: cooking with gas from biomass. Berlin: GIZ.

Rudel, T. K. (2013). The national determinants of deforestation in sub-Saharan Africa. *Philosophical Transactions of the Royal Society of London B: Biological Sciences*, *368*(1625), 20120405.

Speight, J. G. (2010). *The biofuels handbook* (No. 5). Royal Society of Chemistry.

Urgen Bathe, K. J., Hendriana, D., Brezzi, F., & Sangalli, G. (2000). Inf–sup testing of upwind methods. *Int. J. Numer. Meth. Engng*, *48*, 745-760.

Van der Sluis, P. (2015). Energy from Biomass: Cooking without Fossil Fuels, in Van Swaaij,W.P.M.,Sascha, R.,Kersten, R.A.,Palz, W.(Eds), *Biomass power for the World* (pp 227:245), Pan Stanford.

Varunkumar, S. (2012). *Packed bed gasification-combustion in biomass based domestic stoves and combustion systems* (Doctoral dissertation, Indian Institute of Science Bangalore).

Versteeg, H.K. and Malasekera, W. (1995). *An introduction to Computational Fluid Dynamics*, New Jersey: John Wiley & Sons.

Warhaft, Z. (2000). Passive scalars in turbulent flows. *Annual Review of Fluid Mechanics*, *32*(1), 203-240.

Weerasinghe, W. M. S. R., & Kumara, U. D. L. (2003). CFD approach for modelling of combustion of a semi enclosed cooking stove. In *The international conference on mechanical engineering*.

Wilcox, David C. (1998). *Turbulence modeling for CFD*. Vol. 2. La Canada, CA: DCW industries,

World Health Organization. (2013).*Global Health Observatory (GHO), HIV AIDS* [Fact sheet]. Retrieved from: http://www.who.int/gho/hiv/en/

World Health Organization. (2013).*Tuberculosis* [Fact sheet]. Retrieved from: http://www.who.int/gho/hiv/en/http://www.who.int/mediacentre/factsheets/fs104/en/

World Health Organization. (2013).*Malaria* [Fact sheet]. Retrieved from http://www.who.int/mediacentre/factsheets/fs094/en/

World Health Organization. (2013). *Household air pollution and health* [Fact sheet]. Retrieved from: http://www.who.int/mediacentre/factsheets/fs292/en/

Yu, S. T., Jiang, B. N., Liu, N. S., & Wu, J. (1995). *The least-squares finite element method for low-mach-number compressible viscous flows*. International journal for numerical methods in engineering, 38(21), 3591-3610.

Zienkiewicz, O. C., & Taylor, R. L. (2000). *The finite element method: Solid mechanics* (Vol. 2). Butterworth-heinemann.

Zienkiewicz, O.C., Taylor, R.L. Nithiarasu, P. (2005). Finite Element Method for Fluid Dynamics (6th Edition). Elsevier. Online version available at http://app.knovel.com/hotlink/toc/id:kpFEMFDE04/finite-element-method-3/finite-element-method-3

Zube, D. J. (2010). *Heat transfer efficiency of biomass cookstoves* (Doctoral dissertation, Colorado State University).

GLOSSARY

List of Symbols

Symbol	Meaning
A	Area
B_u	Decay constant
C_p	Specific heat at constant pressure
c_s	Velocity of sound
D	Diameter
E	Energy
E_r	Surface Emissive Power
E_a	Activation energy
e	Internal energy
F	Force
F_{ij}	View factor
G	Irradiation
h	Convective heat transfer coefficient
H	Enthalpy
J	Radiosity
k	Turbulent Kinetic Energy
k_f	Arrhenius Rate constant
M	Molecular weight
N	Number of moles
p, P	Thermodynamic pressure
p_i	Order of a reaction
P_k	Production term
q''	Heat flux
r_f	Rate of a reaction
Q	Heat Flux
R, r	radius
T	Temperature
t	Time
U	Velocity
U_s	Superficial velocity
V	Flow rate
v	Vertical / lateral velocity
w	Mass flow rate
w_h	Weighing function
W	weight
X	Mole fraction
x_o	Virtual origin
Y	Mass fraction

List of Greek symbols

Symbol	Meaning
α	Absorptivity
ρ	Density
φ	Equivalence ratio
ε	Emissivity
τ_r	Reflectivity
ρ_r	Transmissivity
θ	Angle
μ_T	Turbulent eddy viscosity
τ	Stabilization parameter
ω	Turbulent dissipation rate
μ	Dynamic viscosity

Subscripts used

Subscript	Meaning
∞,amb	Ambient
c	Centerline
conv	Convection
f	Fuel
j	Jet
min	Minute
noz	Nozzle
p	Primary
s	Secondary
surr	Surroundings
sur	Surface
vol	Volume
vh	Viscous heating

List of constants

Symbol	Meaning
g	Gravitational acceleration
R_u	Universal Gas constant
σ	Stefan Boltzmann's constant

List of dimensionless numbers

Re	Reynolds number
Ma	Mach number

List of Acronyms

Acronym	Meaning
CFD	Computational Fluid Dynamics
FEM	Finite Element Method
FC	Fixed Carbon
GLS	Galerkin Least Square
GWP	Global Warming Potential
IEA	International Energy Agency
ISO	International Standards Organization
IWA	International Workshop Agreement
PIC	Products of incomplete combustion
PM	Particulate Matter
SUPG	Streamline Upwind Petrov Galerkin
VM	Volatile Matter
WHO	World Health Organization

List of Tensors

Symbol	Meaning
τ_{ij}	Deviatoric stress tensor
e_{ij}	Rate of deformation tensor
δ_{ij}	Kronecker delta